POLITECNICO

MILANO 1863

SCUOLA DI INGEGNERIA INDUSTRIALE
E DELL'INFORMAZIONE

ANALYSIS OF THE PORKCHOP PLOT CONSIDERING ECCENTRIC AND INCLINED PLANETARY ORBITS

TESI DI LAUREA MAGISTRALE IN
SPACE ENGINEERING - INGEGNERIA SPAZIALE

Author: **Jacopo Fossen**

Student ID: 944853
Advisor: Prof. Camilla Colombo
Co-advisors: Dr. Davide Menzio, Prof. Holger Voos
Academic Year: 2020-21

Abstract

Porkchop plots are quick and immediate tools used by mission designers to properly select the most convenient dates in which scheduling an interplanetary transfer between two bodies. These are contour plots which can represent a wide variety of parameters as a function of the departure and arrival date. One of the most important parameters, which embeds the feasibility of a space transfer, is the total ΔV needed to perform the manoeuvres. The aim of this dissertation is to analyse the peculiarities of ΔV porkchop plots among eccentric and inclined planet orbits with respect to the standard graph obtained with the assumption of circular and coplanar orbits. To this purpose, a separate analysis on the different parameters influencing the development of the ΔV contours is needed. The work is developed upon the choice of decoupling the effect of eccentricity, inclination, argument of periapsis and right ascension of the ascending node, considering them once at a time or sometimes in couple. Therefore, it is possible to distinguish the precise motivations beyond the evolution in shape, size and location of the minimum ΔV island in the epoch space. This work is meant to aid future researchers and mission developers to know in advance the characteristic features of a porkchop plot just by knowing the keplerian elements of the orbits. Since generally the Lambert solvers used to produce the porkchop plots are computationally expensive when applied recursively on a large scale of time, an understanding of the role of each parameter can be useful to limit the analysis to specific time windows. The work provides the characteristics of the evolution of the contours, thus defining regions of the domain in which the transfer is feasible and some other regions in which, given a threshold value for the cost, the mission is not affordable in any case. This allows to reduce the width of the time vectors case by case, searching for the solutions only in the proper regions. This thesis is part of the COMPASS project: "Control for orbit manoeuvring by surfing through orbit perturbations" (Grant agreement No 679086). This project is European Research Council (ERC) funded project under the European Union's Horizon 2020 research (www.compass.polimi.it).

Keywords: Porkchop plot, Orbital transfer, Cost reduction, Eccentricity, Inclination, Phasing

Sommario

I Porkchop plot sono strumenti grafici chiari e immediati che aiutano i mission designer a pianificare accuratamente le date più convenienti in cui programmare un trasferimento tra due corpi celesti. Questi grafici sono costituiti da curve di livello che possono rappresentare il valore di diversi parametri in funzione della data di partenza e della data di arrivo. Uno dei parametri principe per stabilire la praticabilità di una missione è il costo totale del trasferimento ΔV, in termini di differenza di velocità da fornire per realizzare le manovre necessarie. Lo scopo di questa tesi è quello di fare luce sulle peculiarità di un porkchop plot generato da un trasferimento orbitale considerando orbite eccentriche e inclinate rispetto a quello ottenuto attraverso l'approssimazione di orbite coplanari e circolari. A questo scopo, è necessaria un'analisi separata dei vari parametri che influiscono sullo sviluppo delle curve di livello già menzionate. La produzione si sviluppa a partire dalla scelta strategica di disaccoppiare l'effetto dell'eccentricità, dell'inclinazione, dell'anomalia del pericentro e della ascensione retta del nodo ascendente, considerandone l'effetto singolo e, talvolta, l'effetto simultaneo a coppie. Pertanto, è così possibile distinguere le precise motivazioni dietro una specifica evoluzione della forma, della dimensione e della posizione di una determinata isola nel piano. Questo lavoro è pensato per servire d'ausilio a futuri ricercatori e ingegneri progettisti, per conoscere le caratteristiche di un determinato porkchop plot a priori, semplicemente dal valore dei parametri orbitali. Siccome gli algoritmi che risolvono il problema di Lambert, necessari per produrre i porkchop plot, sono computazionalmente onerosi quando applicati su larga scala, una conoscenza più profonda del ruolo di ciascun parametro nello sviluppo dei risultati si può rivelare molto utile per limitare l'analisi a specifiche finestre temporali e, pertanto, per ottimizzarne l'efficienza. La tesi descrive le caratteristiche dell'evoluzione delle curve di livello, definendo così regioni del piano in cui il trasferimento è possibile ed altre in cui supera una determinata soglia di accettabilità. Ciò permette di ridurre la dimensione del problema caso per caso, cercando le migliori soluzioni soltanto all'interno di opportune regioni. Questa tesi è parte del progetto COMPASS: "Control for orbit manoeuvring by surfing through orbit perturbations"(Grant agreement No 679086). Questo progetto è finanziato dall'European Research Council (ERC) nell'ambito della ricerca European

Unions Horizon 2020.

Contents

List of Symbols

Variable	Description	SI unit
a	Semi-major axis	m
A	Area enclosed by a contour line	s^2
A_m	Multiplier factor	$[-]$
C_3	Characteristic energy	m/s
e	Eccentricity	$[-]$
E	Eccentric anomaly	rad/s
f	Generic function	$[-]$
f_{syn}	Synodic frequency	$1/s$
G	Universal gravitational constant	$\frac{m^3}{kg\ s^2}$
i	Inclination	rad
k	Generic constant	$[-]$
M	Mean anomaly	rad/s
r	Position vector	m
r_a	Apoapsis radius	m
r_p	Periapsis radius	m
S_θ	Angular distance	rad
t	Time	s
T	Period	s
v_∞	Excess velocity	m/s
V	Velocity	m/s
x, X	Abscissa coordinate	m
y, Y	Ordinate coordinate	m
y^*	Graphical distance	s
y_D	Distortion distance	s
z, Z	Quota coordinate	m

Greek Letters

Variable	Description	SI unit
Δ	Differential operator	$[-]$
η	Angle with respect to ecliptic plane	rad
ψ	Inclination ratio	$[-]$
θ	True anomaly	rad
μ	Standard gravitational parameter	m^3/s^2
π	Euclidean mathematical constant	$[-]$
ϕ	Transfer angle	rad
ω	Argument of periapsis	rad
Ω	Right ascension of ascending node	rad

List of Acronyms

Acronym	Description
2D	Bi-Dimensional
3D	Three-Dimensional
JD	Julian Day
MGA	Multi Gravity Assist
MJD2000	Modified Julian Day 2000
RAAN	Right Ascension of Ascending Node
RF	Reference Frame
TOF	Time of Flight

List of Tables

List of Figures

1 | Introduction

Mankind has always sought to get beyond the limits of the unknown and, since the ancient times, the sky and the space has always been object of romantic interest for artists and educated people. Even before modern times, driven by the desire for knowledge, many scientists theorised and proved the laws of motion of the celestial bodies just by observing the movement of planets, natural satellites, asteroids and comets through telescopes. However, if at those times the interest in this subject might have appeared as not essential, then, thanks to the technological development of XX century the focus on this researches became crucial. With the widespread of space exploration, in fact, the study of the motion in orbit and its application to the design and control of the artificial objects launched in space became a very high-value target. Moreover, the planning of space missions needs taking place years in advance in order to properly consider the requirements and allow affordable costs. Therefore, a new light was given to a class of mathematical problems which up to that time were considered only as matter for theoreticists, but whose applications have been essential in many engineering challenges. Most of these have been evolved throughout the years becoming significant in any mission design.

One of the principal objectives of any mission analysis process is a proper trajectory design. This consists in characterising the orbit to be followed by a spacecraft in order to accomplish the mission [28]. The correct definition of the mission expectations generates some requirements. Then, the research of the best paths compatible with the requirements is performed generally identifying a baseline and some back-up solutions. Afterwards, a recursive and iterative process allows to select the best trajectory for the mission. Generally, the essential requirements involved are the mission requirements which dictate the critical conditions needed, imposed by physical laws. Furthermore, another class of requirements foresee the optimisation of certain parameters. In the space engineering these may be related to the cost of the mission, in terms of fuel consumption, rather than to time constraints to be respected. The process of trajectory design can extend for several years during the development of a space mission and during this process the performance requirements can become more flexible in order to reach a compromise between differently oriented constraints. Clearly the same reasoning cannot be done for the requirements

imposed by the fundamental laws of orbital mechanics.

1.1.   Literature review

A classical tool employed in trajectory design to the aim of planning a space transfer is the use of Lambert's algorithm [13] [34]. Lambert's theorem states that the transfer time is dependant only on geometric parameters such as the sum of the magnitudes of the position vectors, the chord linking them and the semi-major axis [18]. Over the last two centuries, many researchers worked on the topic, providing advancements in the field. The first proof of Lambert's theorem was provided by Lagrange as reported in Battin's book [4]. The main idea of the solution was to perform a particular parametrisation of the transfer orbit in order to express the elapsed time as function of the semi-major axis. The majority of the literature on the Lambert's problem deals with the problem formulation and its numerical resolution. A great advancement in the development of algorithms tackling Lambert's problem came from the work of Lancaster et al. and constitutes the starting point for the majority of the algorithms developed successively [20] [19]. Bate et al. formulated the problem in universal variable approach [2]. Nowadays, Bate's algorithm is considered the fastest one among the different families of algorithms [9]. A key figure was Battin, whose "elegant" method improved significantly the convergence performances and extended the applicable cases of the problem [3] [32]. Important contribution was the one made by Gooding whose algorithm achieved high precision with low computational cost [15].

In modern years many researchers proposed alternative algorithms. Avanzini proposed a new algorithm based on the eccentricity vector. Avanzini's algorithm is not smoother with respect to Battin's method (from a computational point of view) but has the qualities of providing interesting insights on the dynamics and presenting a simpler derivation. Arora and Russell [1] derived a new version of the algorithm exploiting the method of universal variable used by Bate. Izzo, instead, revisited Lambert's problem following again the approach of Lancaster and Blanchard and comparing the results with Gooding's algorithm [16]. His algorithm iterates on the Lancaster-Blanchard variable through a Householder iteration scheme whose initial guess was derived analytically. Among the different classes of Lambert's solvers, Izzo's one offers the best compromise between speed, robustness and accuracy [9].

De la Torre Sangrà and Fantino compared and tested existing algorithms in terms of iteration method, choice of the free parameter and initial guess, while the performances are evaluated in terms of the speed of convergence and the robustness of the method [9]. According to this review, the two best state-of-the-art algorithms are actually Bate's

algorithm via universal variables with Newton-Raphson and Izzo's algorithm.

Lambert's algorithms are an essential tool in mission analysis. They are one of the building blocks for the generation of important engineering charts, called *porkchop plots*. This consists in contour plots tracing the variation of a performance index with respect to time. The information obtained from this visualisation tools can help analysts in performing the preliminary design of any space mission. This plot has been developed to properly schedule an interplanetary transfer and used for the last 60 years. It has been used since the Voyager problem in order to schedule the flybys avoiding specific festivity dates [35]. The plot shows the trend of a particular key parameter as function of the combination of the departure and arrival dates and allows a visual and immediate identification of the suitable dates for the operation. The variation of such a parameter is depicted through colour-coded contour lines.

Usually, the most used parameters are the characteristic energy at departure C_3 or the arrival excess velocity v_∞ because of their role in planning a determined mission and optimizing the interplanetary transfer [33]. Most of the times the mission designers seek for the epoch in which one of these parameter can be minimised in order to reduce the cost of the mission. A problem might arise when the regions in which these two parameters are minimised are not compatible with each other. This is why are often used porkchop plots representing a combined parameter that is the total transfer ΔV, which embeds the cost of the entire transfer [36] [12].

Many papers turned the attention to the different launch opportunities for feasible transfers, especially between Earth and Mars, both considering manned and unmanned missions [21] [31] [7] [14]. Woolley and Whetsel took inspiration from these works and described the morphology of this launch opportunities on the porkchop plot.

Woolley and Whetsel analysed in detail the morphological features of the porkchop plot for the particular case study of an Earth-to-Mars transfer, investigating how the different orbital elements of the two orbits do play a role in varying the ΔV budget [36]. The shape of the porkchop plot is, in fact, mainly influenced by the relative geometry and dynamics of the heliocentric orbits of the two planets.

Menzio's work [22] [23] [24] deals with the analytical determination of the minimum ΔV locations and assesses the shape of different contour lines. Menzio proposed to use ΔV solutions associated to tangential manoeuvres at departure or arrival to determine the shape of contour lines at constant ΔV. Moreover, [22] analysed the regularity on the repetition of contour lines.

On one side a good formulation and iteration scheme increase the convergence speed, on

the other side it is important to reduce the search space. This is achieved through the pruning which is principally applied to Multi Gravity Assist (MGA) trajectories. This method consists in monitoring some key parameters like ΔV or the time of flight Δt maintaining only the solutions for which these parameters are acceptable in the problem under study. The problem of an appropriate pruning technique is not trivial. In literature it is possible to find examples of interesting pruning techniques, especially concerning MGA problems. It is worth to mention especially the work of Blum et al. [5], Izzo et al. [17], Ceriotti [6] and Menzio [22]. Menzio showed that bounding regions can be used to reduce the search space and limit the exponential increase of computational need when more trajectory arcs are considered. Bounding regions allow a finer discretisation mesh and, consequently, a more detailed characterisation of the region around the minimum without spending time to search in unnecessary regions.

Finally, the reasoning is extended to the case of more than one revolution on the transfer orbit. When the time of flight is higher than a certain threshold, it is useful to consider the multi-revolution case. When the possibility of exploiting such time expensive solutions is legitimized, they provide trajectories with lower semi-major axis and lower eccentricity and, in turn, lower ΔV.

1.2. Original contribution and thesis outline

The aim of this thesis is to provide an in-depth analysis of the features of the porkchop plots arising from eccentric and inclined orbits.

Starting from the considerations, among the others, taken by Menzio and Woolley, this work aims to extend their work focusing on the evolution of the contour lines whenever the hypothesis of circular and coplanar orbit is abandoned [22] [36]. The evolution of the ΔV contours due to the variation of eccentricity or inclination of the departure and arrival orbit is meant to be analysed. With the employed strategy each effect will be considered separately. The combined effect is reconstructed starting from the circular coplanar approximation and adding complexities one at a time. Afterwards, all the effects will be summed in order to simulate a real scenario. The study is motivated because it has been revealed how the effective dynamics of the planets generates porkchop plots having minima well approximated by the ones derived by conveniently simplified dynamics.

Moreover, the porkchop plot is generally built after the use of a Lambert's algorithm, therefore the procedure can become computationally expensive when performed recursively on many data points [37]. However, as presented in the work of Menzio [22], a proper analysis on the different configuration between the position of two planets and the characteristics of their own orbit can be useful to predict the position of the minima

without running any code. Consequently, a challenging task consists in analysing the orbital dynamics in order to predict in advance the best time windows to perform the interplanetary travel.

Moreover, another objective of this thesis consists in proposing new versions of the graphs to improve the understanding of the dynamics.

Chapter 2 illustrates the most relevant formulas and theory used in this study. Mathematical modelling and methodology are presented here and constitute the starting point for the derivation of all the results present throughout this composition. The chapter contains a summary of the state-of-the-art results focusing on the relevant advancements present in literature. Successively, the original contribution of the thesis is presented. In Chapter 3 coplanar but eccentric orbits are considered. It analyses the effect of orbit eccentricities on the ΔV, focusing also on the role of the argument of periapsis and phasing. In Chapter 4 the scenario is taken back to the circular orbit case, exploiting this time the effect of inclination in modifying the morphology of contour lines. In this case the effect of the Right Ascension of the Ascending Node (RAAN) is addressed together with the phasing. In Chapter 5 eccentric and inclined orbit will be considered. Here all the complexities are treated simultaneously, resembling as much as possible the real dynamics. Finally, the last chapter is dedicated to the conclusion and to improvements on this field of research, future developments and different strategies to study this problems.

2 | Theoretical modelling and background

2.1. Approximations

The analysis contained in this thesis refers to single interplanetary transfers starting from the more internal planet and arriving to the more external one, without considering any flyby during the trajectory. The spacecraft is considered to be a massless point and the manoeuvres are istantaneous changes of velocity. This means that there are two successive instants of time in which the point mass has the same position but a different orientation or magnitude of the velocity vector. Moreover, the enormous distances of the heliocentric system, allow to neglect the presence of the sphere of influence (SOI) of the two planets [30] [29]. In this way, the position vector of the spacecraft which performs the transfer can be confused at the initial and final time with the one of the respective planet, as they were coincident points. This is the Zero SOI approximation.

The ΔV calculation is derived straight forward, since the heliocentric velocity of the planets in each point is calculated easily once the orbit is defined, and the velocity on the terminal points of the transfer orbit is an output of the Lambert solver.

$$|\Delta V| = |v_{T1} - v_{dep}| + |v_{arr} - v_{T2}| \tag{2.1}$$

where v_{T1} and v_{T2} are the velocities on the transfer orbit at the starting and ending point respectively, while v_{dep} and v_{arr} are the heliocentric velocities of the departure and arrival planet respectively. Consequently, ΔV represents the cost of the transfer in terms of impulse needed. More in general, once the departure and arrival position vectors are chosen, the geometry is fixed and according to Lambert's theory for a specific time of flight (TOF) there is one only parameter defining the orbit piercing the two points. From the evaluation of this parameter the transfer orbit will be defined. Actually two solutions are present: one for prograde and one for retrograde orbits. The former is the interesting one because embeds lower ΔV. Finally, the total cost of the transfer is evaluated summing the

cost of the two impulsive manoeuvres. All these approximations are generally accepted and widely used in this kind of problems because they allow to simplify the problem without spoiling the validity of the analysis.

For the sake of simplicity, the analysis has been carried on using the conditions of an Earth-to-Mars transfer. All the differences are evaluated with respect to the most simple case in which the two planets are supposed to lay on an orbit which has their own real semi-major axis but eccentricity and inclination equal to zero.

2.1.1.   Two-Body problem

In this thesis the motion of spacecraft and planets is described by the Two-Body (2B) problem. This constitutes the classical model describing the mutual gravitational attraction of two bodies in the heliocentric system. Given an inertial reference frame, the two masses m_1 and m_2 are in orbit around their centre of gravity and their position can be defined as follows [8] (Sec. 2, pp. 60):

$$\vec{r_1} = X_1\ \vec{i} + Y_1\ \vec{j} + Z_1\ \vec{k}$$
$$\vec{r_2} = X_2\ \vec{i} + Y_2\ \vec{j} + Z_2\ \vec{k} \tag{2.2}$$

where $\vec{r_1}$, $\vec{r_2}$ indicate the position vectors, $\vec{i}$, $\vec{j}$, $\vec{k}$ are the unit vectors forming the right-handed triad defining the reference frame and X_1, Y_1, Z_1, X_2, Y_2, Z_2 are the components of the position vectors on the three axes. The gravitational force acts along the line linking the two masses. For this reason it is useful to define the relative position of m_1 with respect to m_2.

$$\vec{r} = \vec{r_2} - \vec{r_1} \tag{2.3}$$

Now the gravitational force exterted on m_1 by m_2 can be expressed as a function of the value of the masses themselves, their relative distance and the universal gravity constant G [25] [8] (Sec. 2, pp. 61).

$$\vec{F_G} = \vec{F_{12}} = \frac{G\ m_1\ m_2}{r^2}\vec{u_r} \tag{2.4}$$

where $\vec{u_r}$ is the versor defining the direction of the attraction force, so it is simply

$$\vec{u_r} = \frac{\vec{r}}{|\vec{r}|} \tag{2.5}$$

The equation of motion of m_1 can be derived from Newton's second law [8] (Sec. 2, pp. 61):

$$m_1 \, \ddot{\vec{r_1}} = \frac{G \, m_1 \, m_2}{r^2} \vec{u_r} \tag{2.6}$$

where r is the magnitude of the vector $\vec{r}$ and $\ddot{\vec{r_1}}$ is the absolute acceleration of m_1. In the same way, equation of motion of m_2 can be derived from Newton's third law, the so-called action-reaction principle [8] (Sec. 2, pp. 61):

$$m_2 \, \ddot{\vec{r_2}} = -\frac{G \, m_1 \, m_2}{r^2} \vec{u_r} \tag{2.7}$$

Finally the equations of relative motion can be retrieved [8] (Sec. 2, pp. 62).

$$\ddot{\vec{r}} = -\frac{G \, (m_1 + m_2)}{r^2} \vec{u_r} = -\frac{G \, (m_1 + m_2)}{r^3} \vec{r} \tag{2.8}$$

Considering the great mass ratio between any natural body and any spacecraft ($m_2 \ll m_1$) and considering the mass of bodies concentrated in their barycentre, the dynamics can be simplified with the restricted 2B problem. Therefore the dynamics is described by equation (2.9)

$$\ddot{\vec{r}} = -\frac{\mu}{r^3} \vec{r} \tag{2.9}$$

where $\mu = G \, m_1$.

2.1.2. Ephemerides

Artificial ephemerides are necessary to evaluate the effect on the ΔV considering the individual contribution of each parameter one at a time. Given the semi-major axis a, the eccentricity e, the inclination i, the RAAN Ω and the pericenter anomaly ω, the orbit is defined in the space. Modelling the variation of the true anomaly θ with respect to time it is possible to correct the position of the planet given the modified orbital elements relating the position of the planet as function of the initial time t_0 from which the simulations are started.

As reported in Chapter 3 of Curtis [8], for an elliptical orbit the variation of θ is influenced by the eccentricity of the orbit and by the eccentric anomaly E through Equation (2.10):

$$tan\left(\frac{\theta}{2}\right) = \sqrt{\left(\frac{1 + e}{1 - e}\right)} tan\left(\frac{E}{2}\right) \tag{2.10}$$

where θ is the true anomaly and e is the eccentricity of the orbit. For instance, whenever

the orbit is considered circular, it is easy to retrieve the simplified model imposing the eccentricity to be null. As a consequence, the true anomaly θ equals the eccentric anomaly E and vice versa. The orbital motion of planets is expressed by Kepler equation [8] (Sec. 3, pp. 151):

$$\sqrt{\frac{\mu}{a^3}} \, (t - t_0) = M \tag{2.11}$$

where the right side represents the mean anomaly, which is linked to the eccentric anomaly [8] (Sec. 3, pp. 151).

$$M = E - e \, sinE \tag{2.12}$$

The linking between θ and time is now obtained through Kepler Equation (2.13) which relates E with respect to time, given a determined time vector starting at a time t_0.

$$\sqrt{\frac{\mu}{a^3}} \, (t - t_0) = E - e \, sinE \tag{2.13}$$

The solution of Equation (2.13) has to be found in a numerical way, using an iterative root solver. A Newton's method was used to fulfil equality given by Equation (2.14):

$$E - e \, sinE - M = 0 \tag{2.14}$$

It is useful to apply the Newton's method to the function $f(E)$, whose zeros represents the solution of the problem, since Newton's methods require the knowledge of the function describing the problem under study and its first derivative [10] [11].

$$\begin{cases} f(E) = E - e \, sinE - M \\ \qquad f'(E) = 1 - e \, cosE \end{cases} \tag{2.15}$$

At the end of this iterative process, for a specific value of the time vector, θ is known. The full orbit is retrieved applying the same process for every other value of time assigning an initial value of the eccentric anomaly to the first instant of time. Once the orbit is defined, the artificial ephemerides are created. The majority of the results are obtained using a time vector in days, the dynamics is modeled starting from the choice of a certain initial time which is independent from the real time which can be measured in JD, MJD2000 or other time representations. For this reason, many results are produced as porkchop

plots whose axis present dates of departure and arrival, and both vectors starts from an arbitrary time which is placed to zero. This simplifies the notation. Indeed the artificial ephemerides can be built freely without considering the real position of planets in a specific date. This is not a problem since the real dynamics of planets is preserved.

2.1.3. Lambert solver

The Lambert solver used throughout all the results is a version implemented by Izzo [16]. The solver takes as input the position vectors at departure and arrival, the transfer time and the gravitational parameter of the Sun and gives in output the velocities at departure and arrival on the transfer orbit. This algorithm solves the Lambert's problem following a procedure which differs from other historical version.

The radii and the TOF are normalised, then relevant geometrical parameters such as the chord, the transfer angle and the semi-perimeter are computed. The algorithm refers to the λ variable defined in Battin's book [4]. Afterwards, the algorithm evaluates the solution in terms of $\log(x+1)$ for the zero-revolution case or in terms of $\tan(x\frac{\pi}{2})$ in case of multi-revolution, where x represents the eccentricity. Successively the conic is retrieved in two similar ways depending on the sign of the variable x which discriminates among elliptical and hyperbolic solution.

Two features distinguish this algorithm among the others. First, the description of the orbit solution of the boundary value problem through an original logarithmic variable. Secondarily, after the transfer orbit has been defined the algorithm is able to retrieve the velocity vectors at departure and arrival in a way that removes the singularities for transfer angles approaching to 180 *deg*. This allows equivalent performance capabilities for any geometry of the problem.

2.2. State-of-the-art

In this brief paragraph the most relevant results present in literature regarding the topic are summarised in order to put the following contributions inside a clearer context.

In Menzio's work, circular and coplanar orbits can be used to study in first approximation the dynamics induced by real ephemerides [22] [23] [24]. Figure 2.1 shows the porkchop plot of a transfer between Earth and Mars in which both initial and final orbit are modelled as circular and coplanar. As described in [22], the porkchop plot has a characteristic three-lobed shape which is well described by the trend of solutions which present tangential injection at departure or at arrival. Two lobes out of three stretch in direction of the tangential manoeuvres, while the last one is enclosed by the other extremes of the

aforementioned curves. As it is easy to assume, in the circular and coplanar case, the intersection point between the two curves identifies the ΔV minimum. This is by construction the solution obtained for a Hohmann transfer. Indeed, Figure 2.2 shows that the ΔV minimum is located exactly where the solution shares a TOF equal to the Hohmann's semi-period and a transfer angle ϕ equal to 180 deg, as it is found at the intersection of the two relevant curves.
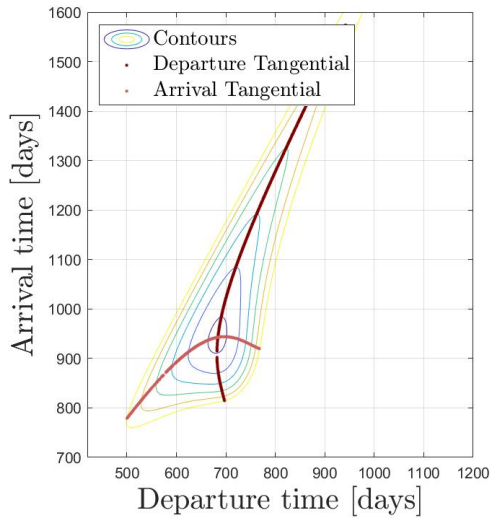
Figure 2.1: Tangential manoeuvres
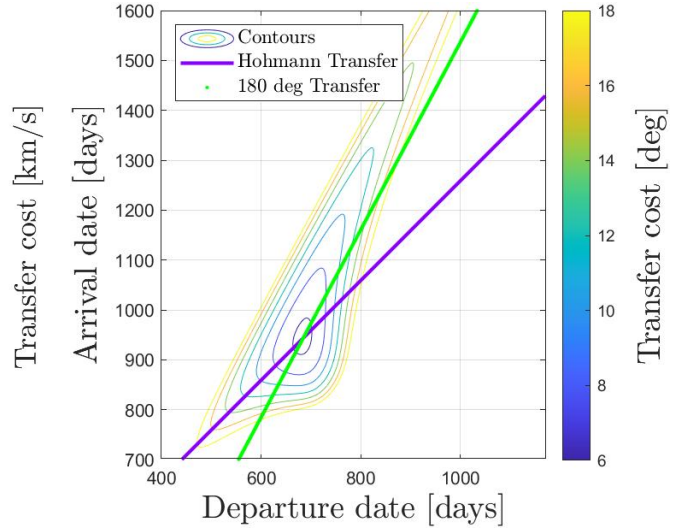
Figure 2.2: Relevant curves

For coplanar and circular ephemerides, the porkchop plot repeats every synodic period. The frequency of these repetitions is the frequency of conjunction f_{syn} which is given by Equation (2.16) and it expresses that the period of the orbit is directly influenced by the semi-major axis. If the synodic period is the definition from the dynamics point of view, the equivalent in space engineering is called *launch opportunity*.

$$f_{syn} = \frac{1}{2\pi}\left(\sqrt{\frac{\mu}{a_1^3}} - \sqrt{\frac{\mu}{a_2^3}}\right) \tag{2.16}$$

For an Earth-Mars transfer the two planets are found in a very similar configuration every 26 months. The ΔV minimum can be found at the intersection between the curves having TOF equal to the Hohmann Transfer and the curve having the transfer angle equal to 180 deg.

The importance of this result is the possibility to identify the position of the minimum in advance without running any Lambert algorithm and just analysing the ephemerides. Actually, the simplified model embeds at global level the information about the position of the minima and their magnitude. This is possible because the repetitiveness is not

influenced by the simplifications of the orbits. Every synodic period, a so-called launch opportunity exists and so a peak in the 3D curve of total ΔV is found as well. This result obtained by the circular and coplanar dynamics is fundamental because is still valid in the real case.

When the circular and coplanar assumption is removed, eccentricity and inclination modify position and velocity of the two planets along the orbit. Consequently, features like the minima locations, their magnitude, the shapes of the contour levels do not repeat exactly the same from one opportunity to the following one. Woolley and Whetsel [36] defined a cycle of variation of the ΔV contour shape. According to him, every 7 opportunities, almost 15 years, a "super-cycle" is defined [36]. In Figure 2.3 for the actual eccentricities and inclinations of Earth and Mars, the results are reported and show that at each launch opportunity a minimum is found at the inner contours, but the entire shape of the porkchop plot varies from one launch opportunity to the following one. Nevertheless every super-cycle the shape and the cost of the porkchop plot are very similar.
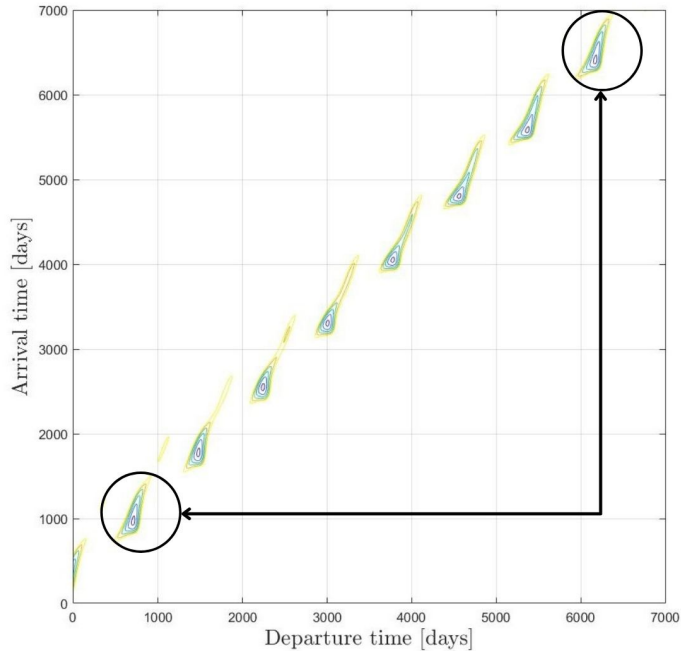
Figure 2.3: Repetition of the porkchop plot over a super-cycle.

Both the works of Woolley and Whetsel [36] and Menzio [22] [23] deal with the similarities and differences between the porkchop plot obtained with simplified ephemerides and the one drawn from the real data. Figure 2.4 shows the ΔV contour lines obtained considering

the real eccentricities and inclinations to the Earth and Mars orbits. It is possible to distinguish two lobes. The lower one refers to short transfers which span less than 180, while the upper one includes long trajectories which span more than 180. In literature they are referred respectively as Type 1 and Type 2 trajectories. The two lobes are separated by a ridge induced by the fact that the two planets lay on differently inclined orbits. The manoeuvre changing the plane of the orbit is more expensive and the ΔV grows out of proportion generating the ridge. Similarly to Figure 2.3 the ridge varies consistently from one cycle to another and can be more or less accentuated. In correspondence of specific dates, when Earth and Marsh are phased properly, even considering the real inclinations of the orbits, there exists trajectories linking the two planets still staying on the same plane of the starting orbit. This happens for a limited combination of dates, a narrow window inside the arrays of dates relative to each opportunity. In correspondence of these dates, a *bridge* forms accross the ridge and links the two lobes of Type 1 and Type 2 trajectories.
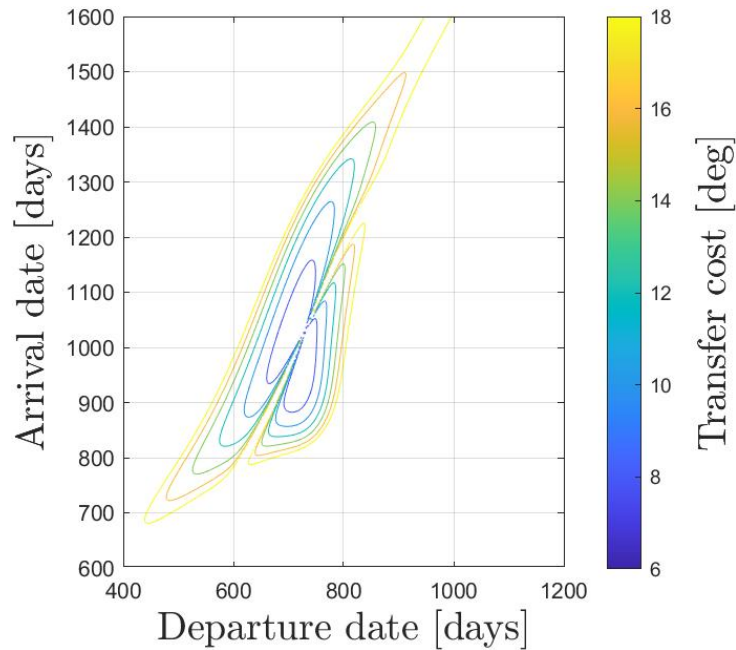
Figure 2.4: Porkchop plot for an Earth-to-Mars transfer obtained considering real eccentricities and inclinations.

3 | Transfer among eccentric orbits

In this chapter, the role of the eccentricity of the orbits of the two planets is examined in order to outline its effect in the morphology of porkchop plots. First of all, it is important to define clearly the Reference Frame (RF) in which the results of this chapter are derived. To analyse the effect of eccentricity alone, separated from the effect of other keplerian elements, the examined orbits are treated as they were coplanar. At this stage both the eccentricity vectors are aligned. The artificial ephemerides are built accordingly and generated.

For simplicity, the three-dimensional RF used is defined as follows:

1. *X axis* aligned with both eccentricity vectors and the vernal equinox;

2. *Z axis* aligned with angular momentum vector;

3. *Y axis* consequently directed according to right-hand rule;

This way, the RF is oriented as the Ecliptic one and it is depicted in Figure 3.1.
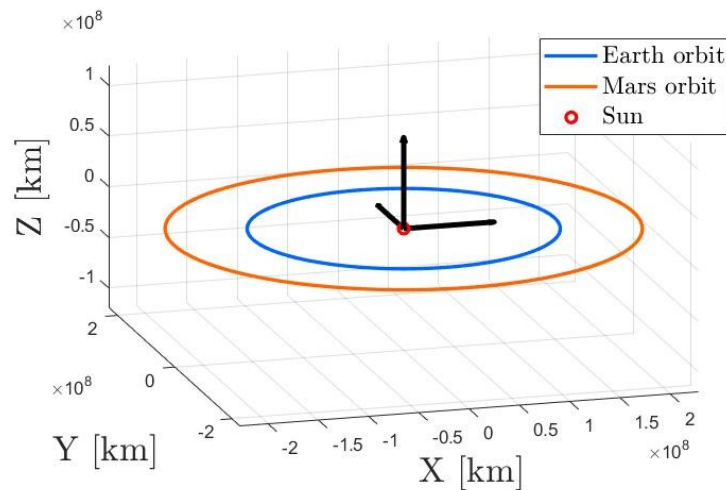
Figure 3.1: Reference Frame for eccentric and coplanar orbits.

At this stage, the argument of periapsis is set as null for both planets, and no phasing is considered. Consequently, both of them are found at the initial position t_0 laying on the

x axis.

The study upon the eccentricity starts defining an acceptable range in which this parameter is supposed to vary. This range has to take into account at least the eccentricities of the existing planets of the Solar System, which are summarised in Table 4.1.

Planet	Mercury	Venus	Earth	Mars	Jupiter	Saturn	Uranus	Neptune
Eccentricity	0.2056	0.0068	0.0167	0.0934	0.0484	0.0542	0.0472	0.0086

Table 3.1: Eccentricities of planet orbits in Solar System approximated at the fourth decimal.

Actually, this range is not so wide, and for a better understanding of the role of eccentricity in the morphology of porkchop plots, this range was extended also to orbits more eccentric than the real ones. From a practical point of view this may seem as a waste of time considering transfer between planets. However, from a theoretical perspective, this extension allows to better understand the transition of the graph and, in turn, the dynamics.

Furthermore, this analysis can be applied not only to heliocentric transfers in the Solar System but also to space transfers inside the sphere of influence of a planet, in its system of moons. Considering all the main moons of the giant gaseous, it is revealed how the highest eccentricity of a moon belongs to neptunian moon *Nereid* and it is equal to $e_{LIM} = 0.7417$ enabling the analysis to reach this magnitudes [26].

A further extension of this limit may be considered when dealing with asteroids and comets, whose eccentricity may get very close to the parabolic limit of $e = 1$. However, this aspect is not considered throughout this thesis.

The analysis of the effect of eccentricity on the ΔV is carried on using the nominal size of Earth and Mars orbits, varying first one and then the other eccentricity. Only successively both orbits will be considered as eccentric at the same time.

These three cases will be referred at with the following notation:

- Case 1: Circular-to-Eccentric transfer (CE) in which only Mars eccentricity varies;

- Case 2: Eccentric-to-Circular transfer (EC) in which only Earth eccentricity varies;

- Case 3: Eccentric-to-Eccentric transfer (EE) in which both eccentricities are considered.

Therefore, keeping fixed one of the two and varying the other one from zero to the upper

boundary discussed above, three different situations may happen.

A subdivision in classes can intuitively distinguish among these three situations:

- CLASS I: The two orbits have no intersection points;

- CLASS II: The two orbits have one intersection point (tangent case);

- CLASS III: The two orbits have two intersection points (secant case).

The switching condition between classes is identified by CLASS II. Depending on the planets considered the value of eccentricity belonging CLASS II is different. In the CE scenario, such a condition is imposed by the following statement:

$$r_{p_2} = r_{p_1} = a_1 \tag{3.1}$$

where r_{p_1} and r_{p_2} are the periapsis radii. Successively, the value of eccentricity such that the tangent condition is matched can be retrieved analytically from simple definitions.

$$r_{a_2} = 2\,a_2 - r_{p_2} \tag{3.2}$$

$$e_2 = \frac{r_{a_2} - r_{p_2}}{r_{a_2} + r_{p_2}} = 0.343691796556438 = e_{2tang} \tag{3.3}$$

In an analogous way, for the EC scenario the condition expressing tangential orbits is given by:

$$r_{a_1} = r_{a_2} = a_2 \tag{3.4}$$

where r_{a_1} and r_{a_2} are the apoapsis radii. Thus, the threshold value of eccentricity for discriminating among classes is retrieved as follows:

$$r_{p_1} = 2\,a_1 - r_{a_1} \tag{3.5}$$

$$e_1 = \frac{r_{a_1} - r_{p_1}}{r_{a_1} + r_{p_1}} = 0.523674387662889 = e_{1tang} \tag{3.6}$$

The three different scenarios for an eccentric orbit of the arrival or departure planet are presented below in Figure 3.2 and 3.3, respectively.
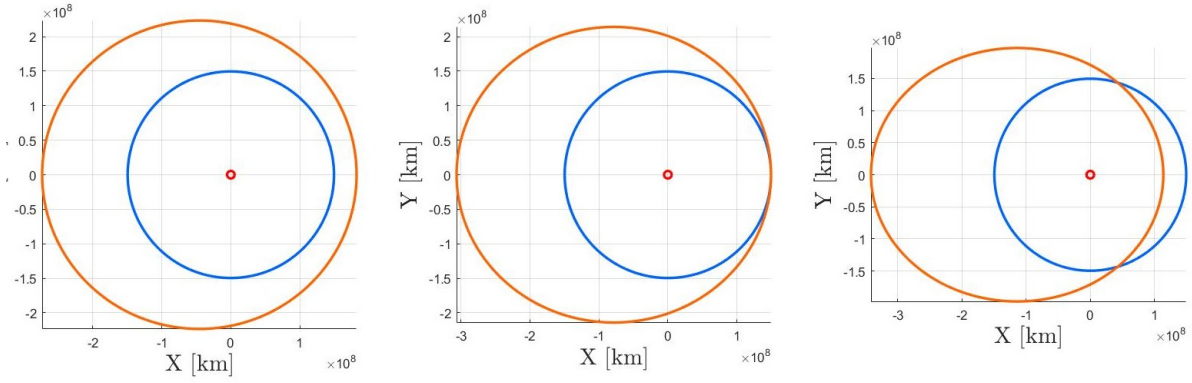
Figure 3.2: CLASS I, II, III for a Circular-to-Eccentric transfers.
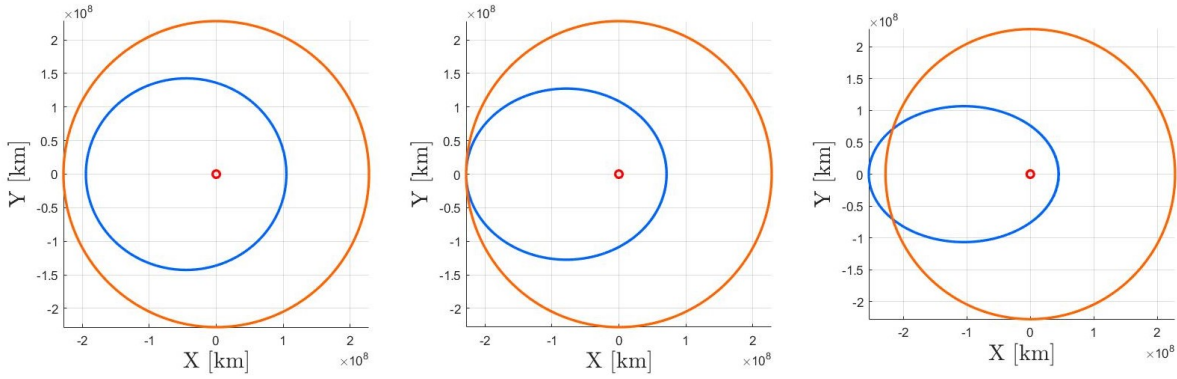
Figure 3.3: CLASS I, II, III for an Eccentric-to-Circular transfers.

Obviously, the orbits obtained modifying the true eccentricity of planets are no more similar to the original orbits, they just share the same semi-major axis. To be precise they should be addressed as *Earth-like* or *Mars-like* orbits. However, for a matter of simplicity all the unreal orbits are identified simply as Earth and Mars orbits or departure and arrival orbits.

3.1.   Eccentric arrival orbit

Firstly, it is considered the effect induced by the eccentricity of the arrival orbit. In Table 3.2 a diagram of the eccentricity ranges for the different classes of the CE transfers is presented.

	CLASS I	CLASS II	CLASS III
range	$0 < \text{e} < \text{e}_{2tang}$	$\text{e} = \text{e}_{2tang} \approx 0.3437$	$\text{e}_{2tang} < \text{e} < \text{e}_{LIM}$

Table 3.2: Definition of classes for CE scenario.

Considering the ranges described in Table 3.2, all the different orbits taken into account are shown in the following graph where the color scales from orange to yellow for increasing eccentricities as expressed in the colorbar, while the red dashed line indicates the trajectory of CLASS II.
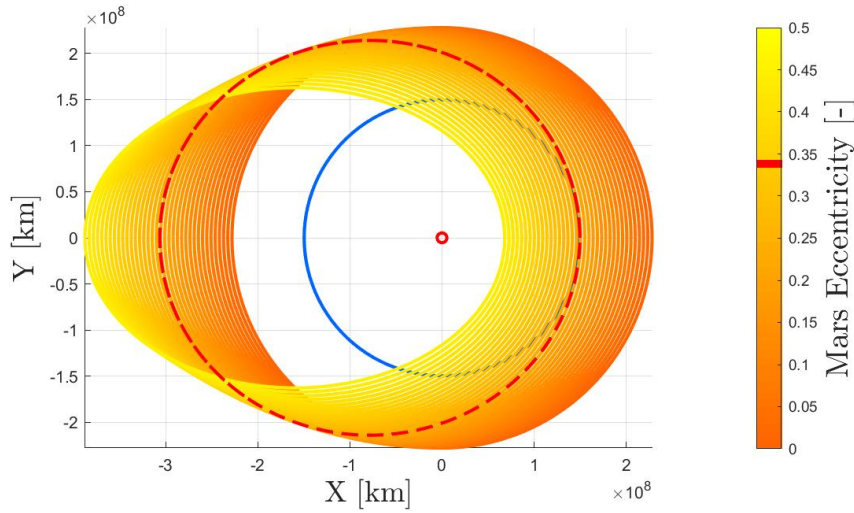
Figure 3.4: Orbit variation with eccentricity (Case 1).

The first aspect considered is the observation of how the eccentricity can vary qualitatively the shape of the porkchop plot. The effect of increasing eccentricity on the porkchop plot is visible from Figure 3.5. A threshold value for the maximum contour allowed was chosen to be equal to 20 km/s. Indeed, despite $10 - 12$ km/s is the target value, this limit is used to better understand the dynamics. This condition can be obtained intersecting the 3D curve itself and a horizontal plane passing for $z = 20$ km/s. The contours emerging from this plane are referred as ΔV *islands*.

Increasing the eccentricity the classic three-lobed shape obtained for the circular case is significantly modified. Two of the three lobes associated to tangential manoeuvres are stretched towards the diagonal, enlarging the figure.

At eccentricities approaching e_{2tang} the main island, which is an intact series of contours at low e_2, separates into more than one island. As a result, more islands populate the porkchop plot at higher eccentricities, offering more combination of dates in which the overall cost of the transfer is affordable.

As can be deduced by Figure 3.5, the more the island are separated the more the initial absolute minimum inside a particular launch opportunity (linked to the synodic period) turns into two or more local minima. When eccentricity becomes higher than e_{2tang}, the new local minimum born in the South-West region of the single launch opportunity contour reveals to be even more convenient than the original minimum in terms of ΔV.
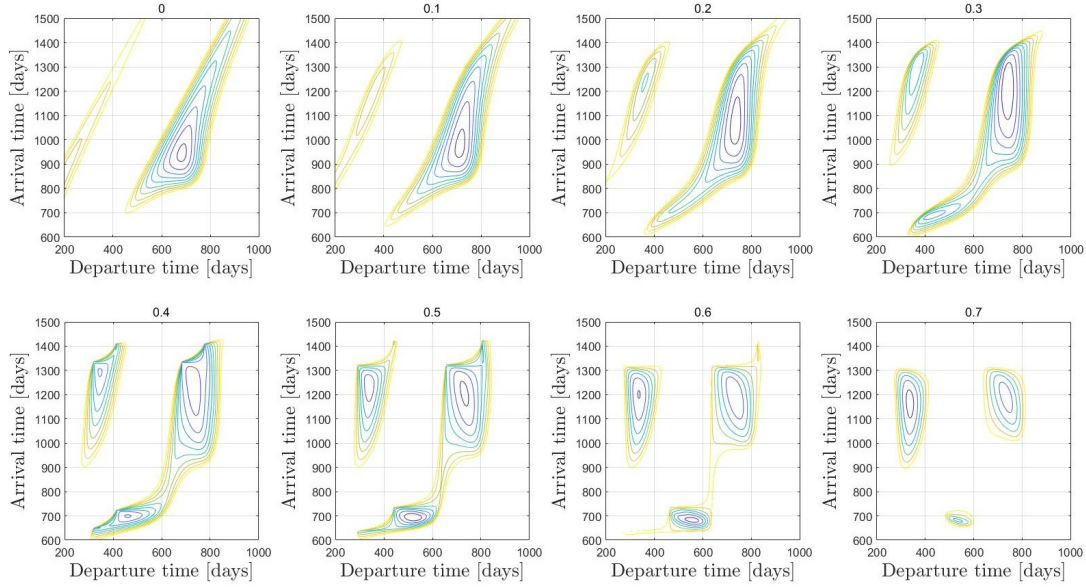
Figure 3.5: Modification of the porkchop plot for increasing eccentricity (Case 1).

In Figure 3.6 the evolution of a generic ΔV island is analysed in detail. From the upper and bottom-left lobe two new minima arise as a consequence of the increased eccentricity.
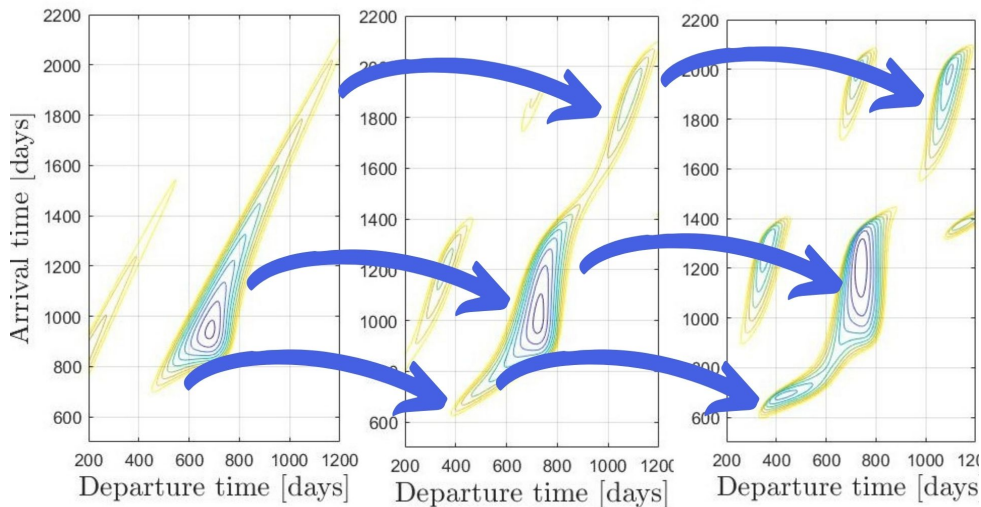
Figure 3.6: Evolution of porkchop plot with arising relative minima

The interesting point is to know how to locate a priori these islands generated at higher eccentricity, because they identify regions in which it is advantageous to organise a transfer. The positions of the minimum ΔV solution for varying eccentricity can be explained with a trend of the favorable conditions for the transfer, which strictly depend on the relative motion between the planets. In Figure 3.7 an evolution of the minima positions can be observed. Scaling the eccentricity of the martian orbit with variation of color from orange to yellow, the position of the minima tends to align with a certain vertical straight line. The highest position in the graph is depicted with a red dot which indicates e_{2tang}, confirming that the solution belonging to CLASS II acts as a divide. After a certain eccentricity, however, the trend of locations is subject to a sharp change so that the minima line up horizontally following once again a straight line in the bottom part of Figure 3.7. This of course involves particular dates of departure or arrival which on the porkchop plot are represented with vertical or horizontal lines respectively. These lines at which the solution asimptotically tends turn out to be related to the dates in which the respective planet transits at its perihelium. A correlation with Figure 3.5 comes from the realisation that the different trend of minima after a certain eccentricity is linked to the presence of the newborn island in that region of the plot.
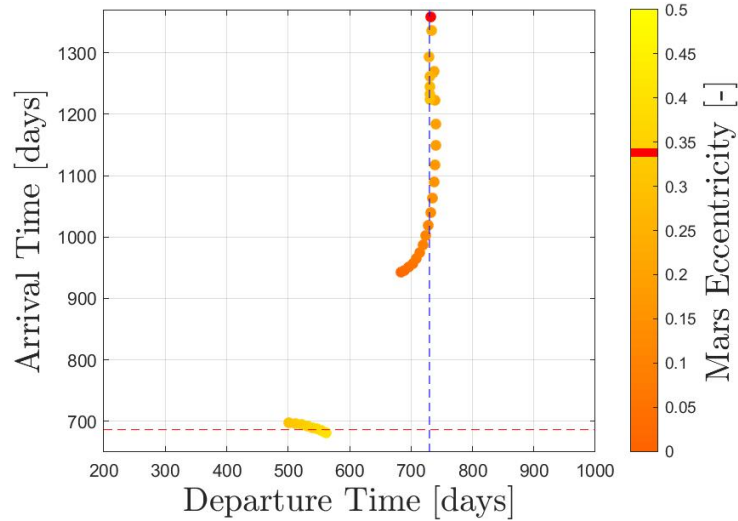
Figure 3.7: Evolution of minima location on porkchop plot for varying eccentricity (Case 1)

Once the semi-major axis is fixed the period of the orbit is independent from the eccentricity. For this reason, a regularity in the repetition of the perihelium transit dates can be observed, that is why even enhancing the eccentricity these lines remain fixed and the minima position aligns accordingly.

Moreover, these trends are explained by the fact that solutions at low ΔV resemble a

Hohmann transfer. Indeed, Figure 3.8 shows that at low eccentricities (CLASS I) the low ΔV solutions depart near $\theta = 0$ and arrive near the aphelium of Mars. However, when eccentricity gets considerably higher (CLASS III) low ΔV solution switch and arrive at the perihelium of Mars. This happens because in correspondence of the periapsis the distance of Mars from the Sun becomes smaller than the terrestrial radius.
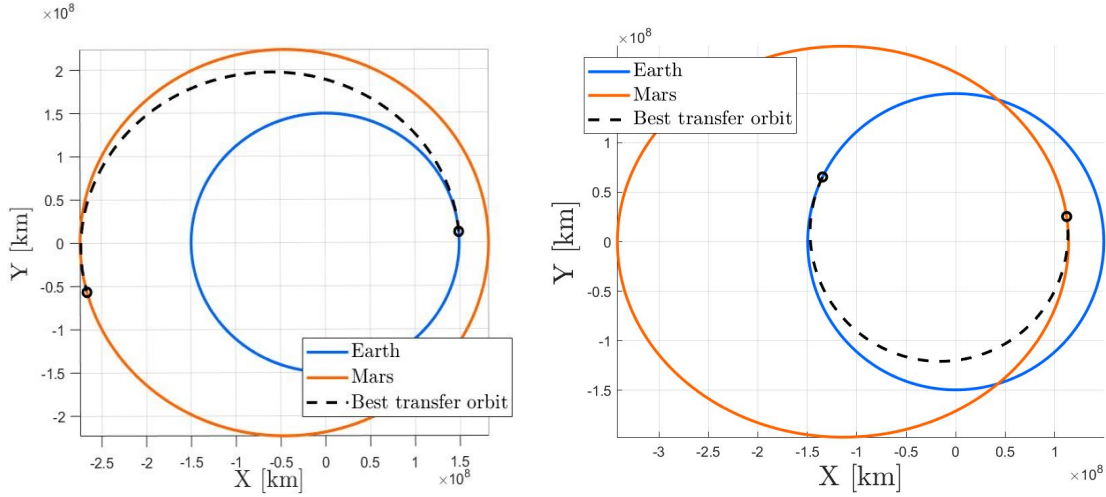
Figure 3.8: Minimum ΔV trajectory associated to $e_2 = 0.2$ (left) and $e_2 = 0.5$ (right).

For any eccentricity belonging to CLASS I, the trend of the ΔV solution is displayed against the TOF. Fixing the departure position at perigee and the arrival position at the apoapsis of Mars, the minimum ΔV is linked to the TOF of an analogous Hohmann transfer. This TOF is the Hohmann TOF of a transfer orbit linking the initial circular orbit and another circular orbit having the radius equal to the apoapsis radius of the arrival orbit at that eccentricity.

$$
\begin{cases}
r_{p_H} = r_{p_1} \\
r_{a_H} = r_{a_2} \\
a_H = \dfrac{r_{p_H} + r_{a_H}}{2} \\
TOF_{Hohmann} = \pi \sqrt{\dfrac{a_H^3}{\mu}}
\end{cases}
\tag{3.7}
$$

It is important to notice that the ΔV is different with respect to the fictitious circular orbit which has a different semi-major axis with respect to the eccentric orbit considered. The difference is expected as the velocities of the arrival orbits are not the same. The only parameter which is equal is the TOF.

In any case the result present in Figure 3.9 can justify the trend of minima location to align with the transit lines. Moreover, even if the magnitude of the minimum and the $TOF_{Hohmann}$ will be different, an analogous curve is reproducible for any value of e_2.
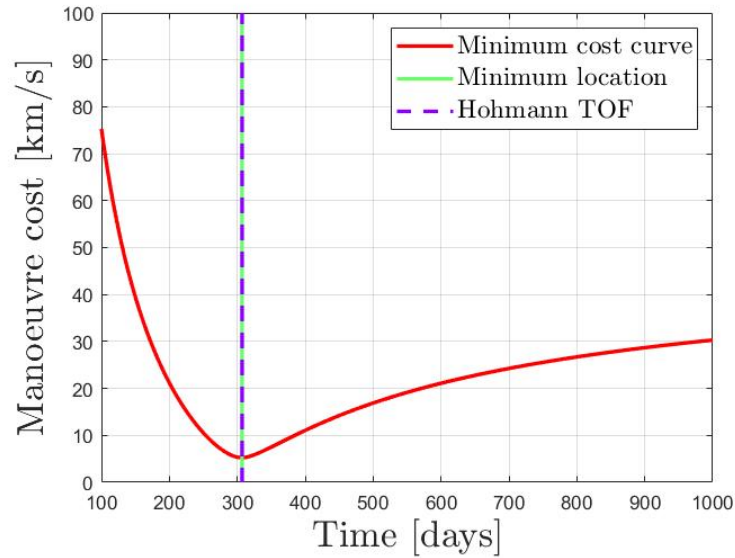
Figure 3.9: Evaluation of minimum ΔV and match with Hohmann-like TOF

An further insight can be noticed from Figure 3.10 where it is shown the porkchop plot for the ΔV contours lines of CLASS II eccentricity together with the straight lines identifying the transit of planets at their perihelium. Earth perihelium passages are reported in blue, while Mars ones in red. CLASS II is clearly an ideal scenario, but from this situation many reasonings can be done.
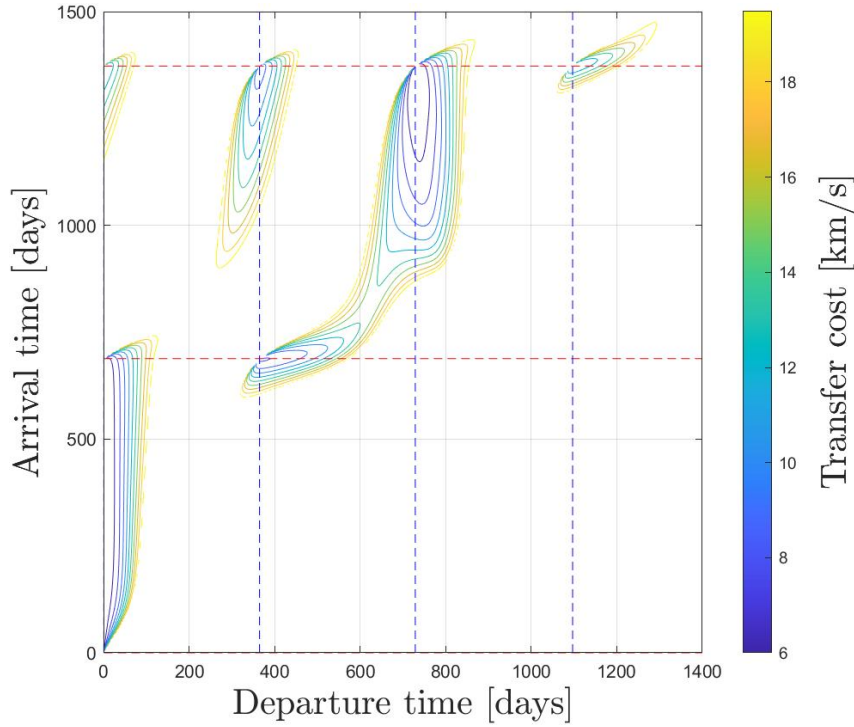
Figure 3.10: Porkchop plot for a CLASS II transfer

First of all, in correspondence of e_{2tang} also the ΔV contour lines produced on the porkchop plot are tangent with respect to each other and the tangent point is also the intersection point between the transit lines of the two planets.

Furthermore, a reasoning about the meaning of the different islands located in the plane can be done. In Figure 3.10, a main peak is produced almost any 2 years (since the synodic period is 2.14) and is identified by the second vertical transit line.

Instead the islands containing the local minima (i.e. in correspondence of the first vertical transfer line) correspond to particular opportunities in which the planets are phased in a worse way but still enabling a feasible transfer. The particular solution defined by the departure after 365 days since the beginning of the time window has not a main peak but still 2 solutions at low ΔV which can be exploited if the mission needs arriving in proximity of Mars perihelium passage.

Moreover, it is important to notice that up to now no phasing between the two planets is considered, that is the reason why the transfer in the point (0,0) happens in the very ideal case in which the two planets are in the same point, for this reason the transfer can be realised with a single impulse. More interesting contours in the plot are the following ones, when the alignment occurs for true anomalies different from zero, thus expressing a more real situation.

So, the reason why the main island is divided into different islands for increasing eccentricities has been shown in order to describe the morphological behavior of the porkchop plot. From a more practical point of view, the following diagram presents a drawback. If it is true that for scenarios belonging to CLASS III ($e > e_{tang}$) the local peaks are more relevant (lower ΔV), it is also true that the minimum ΔV calculated in this condition increases as well, as indicated in Figure 3.11. This reveals that theoretically high values of eccentricity are useful to understand the dynamics but practically this convey complications. In other words it would not be convenient to perform a direct Earth-to-Mars transfer when e_2 is too high.
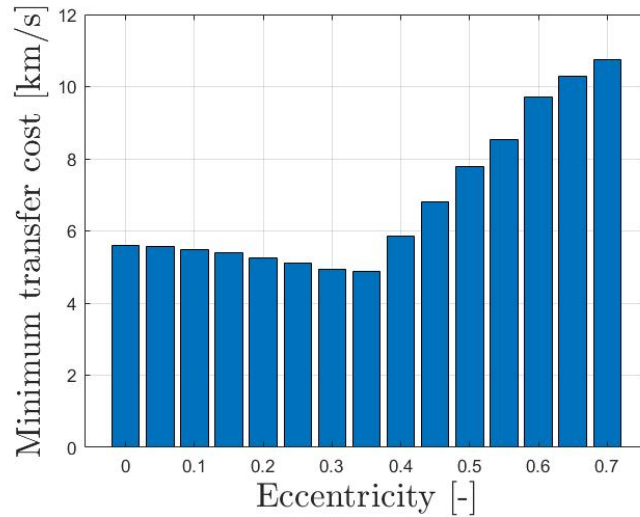
Figure 3.11: Magnitude of minimum ΔV for varying eccentricities

Furthermore, CLASS II and III scenario appears less interesting from a practical point of view. Indeed, at this stage the inclination is not considered, thus a similar situation is not reflected in a real world scenario. Moreover, whenever an orbit crossing occurs in the time scale of the Universe a collision would be unavoidable. In addition, when the two planets get really close to each other, the frame of reference of the two-body problem reveals to be inappropriate in describing the gravitational interactions and this is out of the scope of this work. For these reasons, from now on only the results of CLASS I will be investigated while CLASS II will be used as a limiting case.

Concentrating on CLASS I eccentricity range, the results shown that increasing values of e_2 modify significantly the shape of the ΔV island. Furthermore, a focused analysis can be performed in order to describe and quantify this modification. The aim is to understand what happens approaching the CLASS II limit and describe the evolution. The following graph shows how the eccentricity modifies in size and position the contour $\Delta V = 6\ km/s$,

which represents a good threshold to describe the region around the minimum. For
any eccentricity, the departure and arrival dates associated to a determined contour are
converted into the respective true anomaly intervals. The limits of each interval are
displayed in the graph through quadrilateral regions which modify their width. The blue
and red dashed lines shows the angular distance of a full revolution and have the role of
the transit lines in this frame of reference. When the eccentricity is different from zero,
the quadrilateral boxes describing the intervals are affected by the characteristic dashed
lines. The true anomaly ranges are modified accordingly and Figure 3.12 shows that the
boxes are attracted more and more as the eccentricity is close to the CLASS II limit.
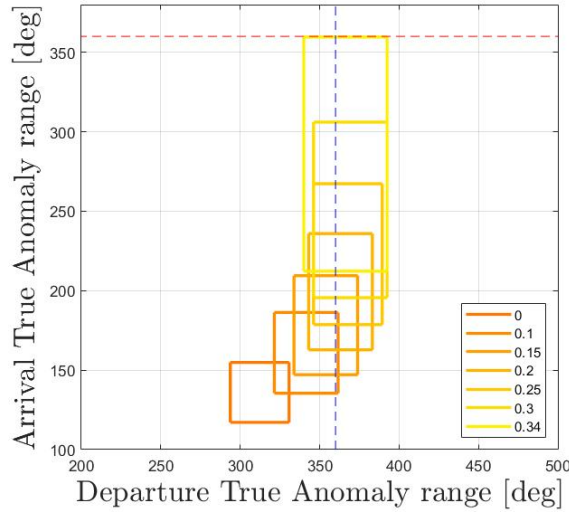
Figure 3.12: Variation of θ ranges associated to contour $\Delta V = 6 \ km/s$

The true anomaly is on purpose left unbounded to prevent the quadrilateral boxes to
collapse. Therefore the axes indicate the value $\overline{\theta} = \theta + k \ 2\pi$ where k is the number of
revolutions of the planet.

The choice to make reference to transit lines rather than to the Hohmann transfer line and
180 deg transfer line lays on the fact that, for eccentricities different from zero, the location
of the minimum does not match the intersection point of the two lines. Increasing the
eccentricity of the arrival planet, indeed, the Hohmann equivalent trajectory, as defined
in Equation 3.7 has a slightly higher semi-major axis, resulting in a higher period. In
the porkchop plot it is visualised as a straight line moving upwards with an increasing
eccentricity. The 180 deg transfer line, instead, varies its shape due to the different time
evolution of the planet true anomaly along an eccentric orbit, as expressed in Equation
(2.13).

The intersection between the Hohmann transfer line and the 180 *deg* transfer line is computed analytically for each eccentricity and the distance with respect to the position on the porkchop plot of the respective minimum is displayed in Figure 3.13.
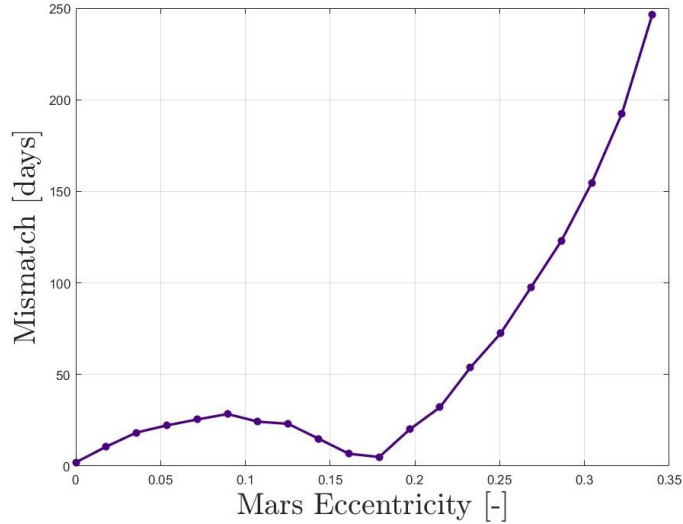
Figure 3.13: Error between minimum position and characteristic lines intersection when circular assumption is abandoned.

The result shows that only for null eccentricity it is easy to locate the minimum with the intersection of the two characteristic curves, as was reported by Menzio [22], while for higher eccentricities this is not valid anymore. In Figure 3.14 it is shown that the 180 *deg* transfer line is a good estimator until a certain threshold but then it becomes imprecise.

It is possible to relate the modification in shape of the ΔV contours with the distortion of the contour plot expressing the transfer angle ϕ. The transfer angle is an output of the Lambert solver, so its evolution is easily recovered and an analogous contour plot is presented. In order to better visualise the distortion caused by the increasing eccentricity, the ΔV contours are plotted over the lines highlighting the magnitude of the transfer angle. This can help the visualisation since the information on the transfer angle would not be directly visible in the porkchop plot, unlike the information on the TOF. In the following figure the variation of some ΔV contours already shown previously (here in black for the sake of clarity) are superimposed on the contours of the parameter $\overline{\phi}$ defined as follows.

$$\begin{cases} \overline{\phi} = \phi & (\phi < \pi) \\ \overline{\phi} = 2\pi - \phi & (\phi > \pi) \end{cases} \tag{3.8}$$

where $\phi = \theta_2(t_{arr}) - \theta_1(t_{dep})$.

The eccentricity considered are reported in the title of the graph.
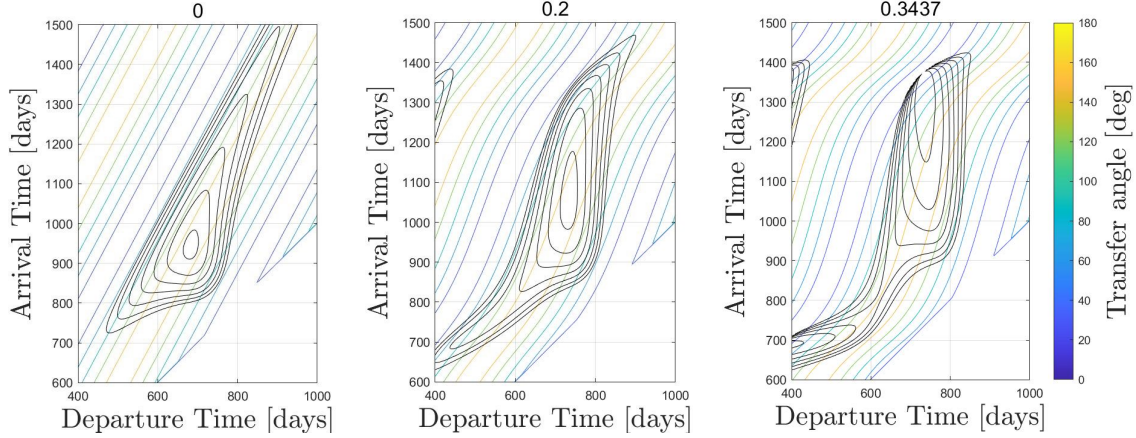
Figure 3.14: Porkchop plot completed with the information of transfer angle for different eccentricities.

The image shows that for $e_2 = 0$ and $e_2 = 0.2$ the transfer angle included in the interval between 150 and 210 deg identifies somehow the minimum. At higher eccentricities the inner contours comprehend both transfer angles values close to $\phi = 180$ deg as in the simple circular assumption and close to the ideal 0 deg transfer possible in case of CLASS II solution.

In summary, an eccentricity different from zero modifies the shape of the lines having constant ϕ. This is partially responsible for the distortion of the ΔV island represented. However, these graphs are obtained for similar phasing. Considering a bigger time window it is possible to notice that the ΔV islands are different from one launch opportunity to the successive one as soon as the e_2 differs from zero. This means that, even fixing the eccentricity, the plot does not repeat identically, so there is another factor responsible for the change of shape.

In other words, the role of phasing shall be addressed. This will be done in the next section.

3.1.1. Phasing

The concept of phasing is fundamental when referring to real life scenario. In real situations indeed the planets are (almost) never in a condition such that they align at $\theta = 0$, as was imposed before for simplicity.

Throughout this thesis, with *initial phasing* it is intended the initial angle defined by the

position vectors of the two planets at the beginning of time vector, thus resulting in the difference of true anomaly at $t = t_0$.

$$\Delta\theta = \theta_2(t = t_0) - \theta_1(t = t_0) \tag{3.9}$$

The *transfer angle* ϕ instead is the angle between the position vector of the departure planet at departure and the position vector of the arrival planet at arrival. It is the angle subtended by the heliocentric leg.

$$\phi = \theta_2(t = t_{arr}) - \theta_1(t = t_{dep}) \tag{3.10}$$

For this reason, if ϕ is a NxM matrix of values which differ considering departure and arrival times, $\Delta\theta$ is a scalar value defined at time $t = 0$ or whenever a new analysis is performed. For example, if a new analysis is started any successive time the Earth transits from its periapsis, the phasing of Mars will be always different (a part from extremely long time intervals). So, $\Delta\theta$ is defined at the beginning of each simulation and its value strongly affects the position and the shape of the contours, even when eccentricity is fixed.

The importance of phasing is extremely relevant when dealing with long intervals of time. Indeed, since the periods of the two planet orbits are neither equal nor multiple (unless specific cases in which the synodic period is an integer number), from one launch opportunity to the next one a different initial phasing affects the relative position of the planets. This generates different phasing-TOF combinations and in turn results in different shape, size and location of the contours. In other words after a synodic period the planets will be aligned again but not at $\theta = 0$. Consequently, if a simulation is started any time one of the planets transits from its periapsis (imposing t_0), the phasing will be different for any different transit. Moreover, once the orbits are fixed, like in real case scenarios, the only parameter which can vary is the phasing which embeds the time evolution. In an infinite time interval, indeed, all the different phasing-TOF combination can be obtained.

Figure 3.15 shows the ΔV contour lines obtained in the same launch opportunity and for different values of the initial $\Delta\theta$. In this figure the true anomaly of Mars is modified introducing a negative θ_{Mars} (specifically $0, 15, 30$ and $45 deg$) while θ_{Earth} is fixed and equal to zero. Considering X and Y the position of planets in the plane of the orbit, the only variation of eccentricity modifies the X coordinate of planets at t_0 (refer to Figure

3.2). However, modifying the initial phasing, an offset is imposed to θ_0 so both X and Y initial position will change with respect to their values in the standard case of null phasing: x_{10}, y_{10}, x_{20} and y_{20}. The scenario is summarised in Table 3.3.

	$\theta_1(0)$	$\theta_2(0)$	$X_1(0)$	$Y_1(0)$	$X_2(0)$	$Y_2(0)$
variable $\Delta\theta$	0	$\overline{\theta_2}$	x_{10}	y_{10}	$\overline{X_2}$	$\overline{Y_2}$
null $\Delta\theta$	0	0	x_{10}	y_{10}	x_{20}	y_{20}

Table 3.3: Mars phasing scenario.

In Figure 3.15 the eccentricity of Mars is fixed and belongs to CLASS II. This is always an ideal but remarkable case, since the transit lines cross the inner contours from side to side, easily localising them in advance, without any computational effort.
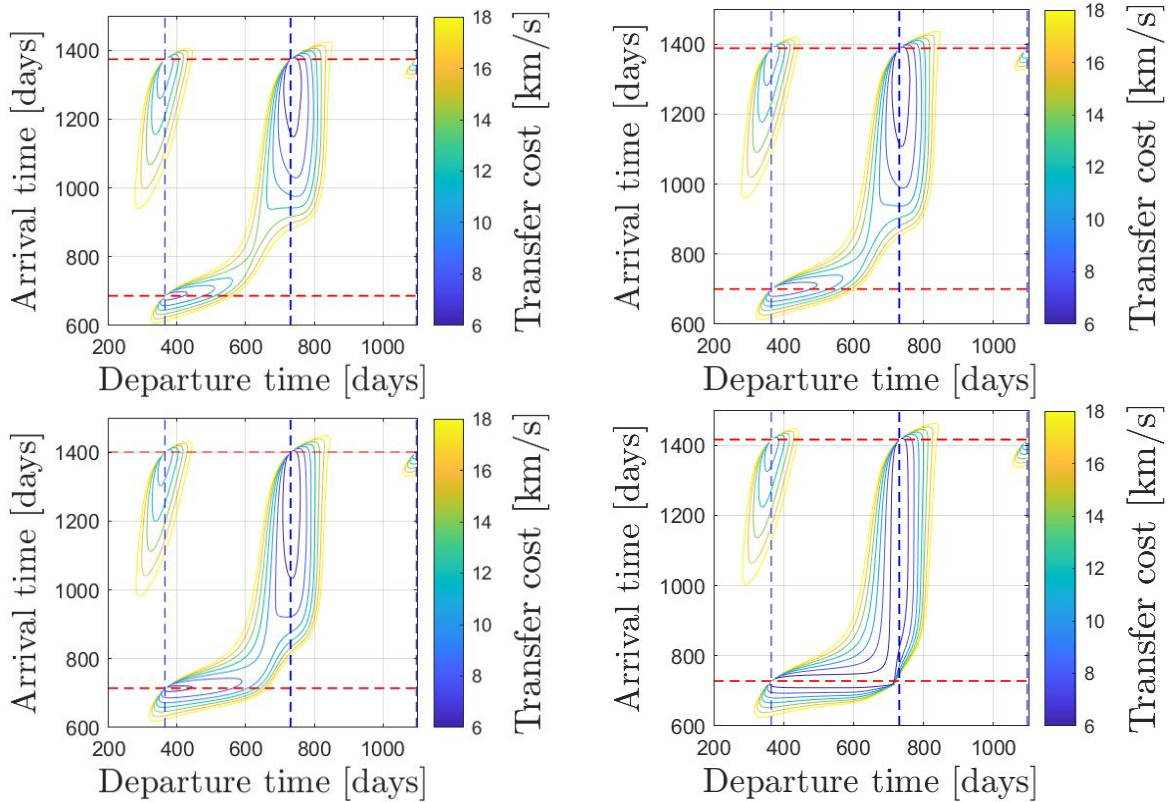
Figure 3.15: Effect of phasing for fixed eccentricity.

Figure 3.15 displays only the variation due to an offset of Mars, for this reason the vertical dashed lines are drawn for a constant date, while the horizontal ones show a slight

difference. This is correct since, the date of transit of Mars at perihelium is modified by the offset to $\theta_{Mars} < 0$ at t_0.

Above all, the principal qualitative effect of phasing consists in exaggerating the area of the inner contours. In correspondence of a specific phasing, the contour lines associated to low ΔV expands significantly, as in the case displayed in the figure obtained for an initial phasing of Mars of $-45\ deg$.

An analogous result can be derived whenever the initial θ_{Earth} is modified: although in both cases the contours are modified significantly, the magnitude and shape of the modification is not the same for the same initial $\Delta\theta$. This happens because of the different features of the orbits (one circular, the other elliptical). For this reason the contours are different even for equal values of $|\Delta\theta|$ i.e. if the phasing of $45\ deg$ is imposed to Mars and if $-45\ deg$ is imposed to Earth.

To obtain a global picture of the effect of phasing it is possible to observe how the an interesting contour (again $\Delta V = 6\ km/s$ can be a good choice) modifies its shape and location for any value of initial phasing in the whole interval from 0 to $360\ deg$.

From the literature it is known that a launch opportunity is generated any time the two planets align themselves. So, it is expected that varying the initial phasing the alignment will be anticipated or postponed. This effect causes a translation of the contour in the plane as well and allows to identify an admissible region of the plane where a specific contour is supposed to be located throughout time. And the shape of the envelop depends on eccentricity.

Now it would be difficult to represent in the same plot both the variation due to eccentricity and the effect of phasing. So, a wise way to analyse the effects is to plot separately the variation of contours obtained for different values of $\Delta\theta$ for many eccentricities belonging to CLASS I. In the following plots are represented the contours associated to $\Delta V = 6\ km/s$ for initial phasing of Mars varying from 0 to $360\ deg$. The value of eccentricity is reported in the title of the plot, while the color scale represents the different initial phasing.

The violet line is taken as reference to analyse the distortion due to eccentricity and it represents the Hohmann-like transfer discussed above.

The simple circular case shows that the translation is parallel to the Hohmann line. This result is expected since for circular orbits the Hohmann line is always identifying the minimum position. However, as analysed previously, due to the effect of eccentricity the location of contours generally moves away from the Hohmann transfer curve. Moreover, increasing the eccentricity but remaining in the eccentricity range of CLASS I, the effect is magnified and bring the contours to align to the transit lines. This result is once again

expected since for CLASS II the transit lines has been observed crossing completely the figure.
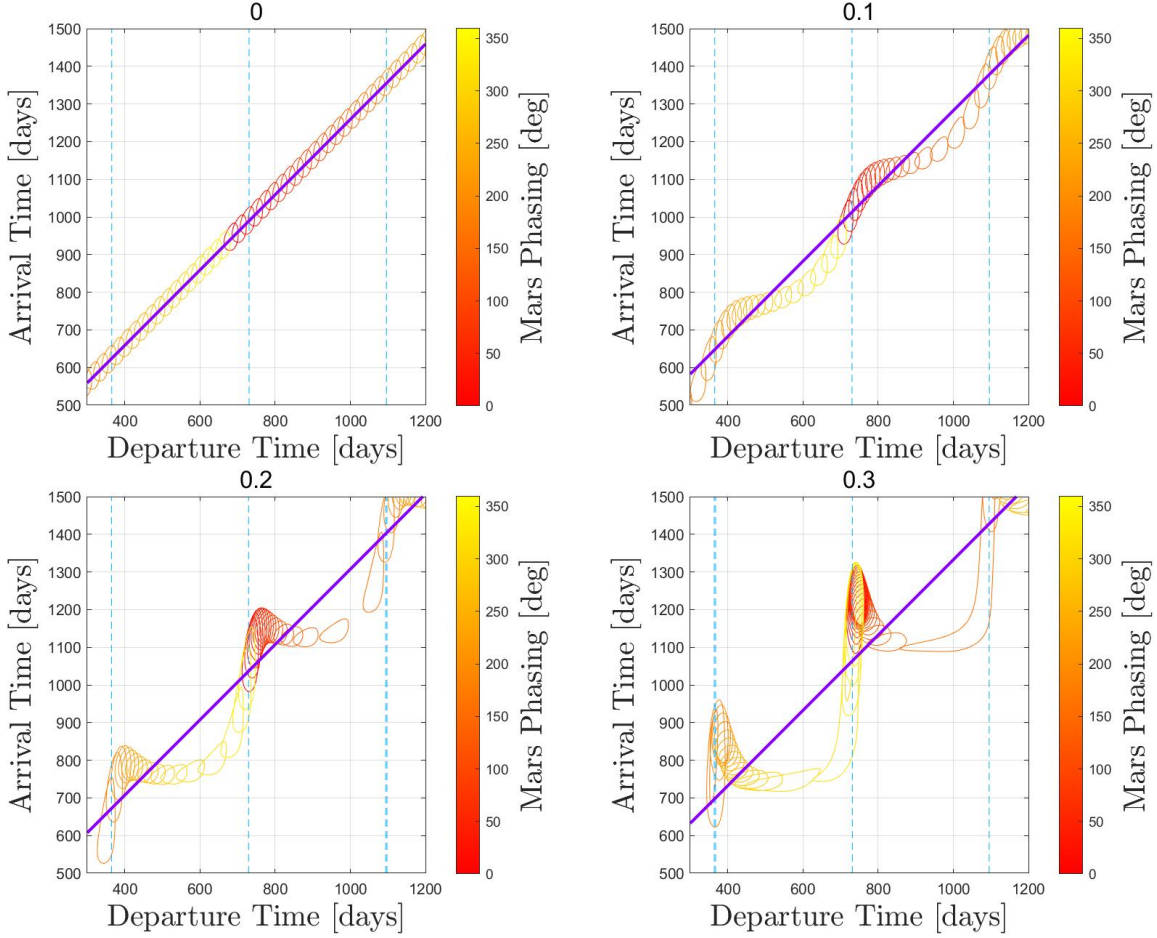
Figure 3.16: Variation of contours introducing an offset to Mars (for different CLASS I eccentricities).

The envelops show an interesting oscillating behaviour which becomes stronger with eccentricity and whose maxima are attracted by the transit lines. The higher is the eccentricity, the more the shape of the contour varies with phasing. In the case with $e = 0.3$ the interesting *L shaped* contours described earlier is noticeable in the top-right part of the plot.

After the envelop has been built varying the phasing from 0 to 360 deg, for any departure date it is possible to retrieve the top and bottom points which limit the envelop. Connecting all these limiting points the upper and lower bound of the envelop has been reconstructed as a function of the departure time and are referred to as y_{upper} and y_{lower}. Averaging their values allows to obtain a unique curve y_{mean} that retains the information

of the phasing variation depending on eccentricity.

A compact way to represent and compare different oscillations can be achieved through a change of variables of the Y coordinate of the curve just described. This transformation aims at flattening the line associated to the Hohmann transfer time for all X coordinates.

$$\begin{cases} x^* = x \\ y^* \left(x \right) = y_{mean} \left(x \right) - y_{Hohmann} \left(x \right) \end{cases} \tag{3.11}$$

where x expresses the dependency on t_{dep}, while y_{mean} and $y_{Hohmann}$ are the functions describing respectively the mean envelop and the solutions having TOF equal to Hohmann's semi-period as a function of t_{dep} itself.

With this change of coordinates, it is easier to interpolate the data and observe a common behavior of the envelop. Many interpolation methods can be applied, in this case a spline has been used to reconstruct the evolution of the contour.

In Figure 3.17 the envelops are shown in this more intuitive reference frame.
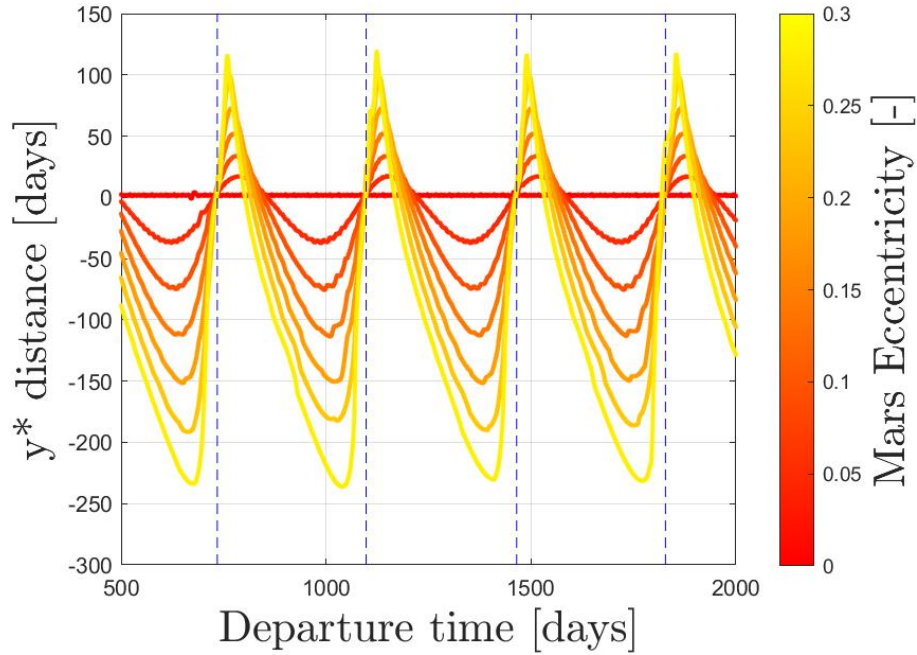
Figure 3.17: Evolution of y^* envelop due to introduced offset of Mars.

The effect of modifying Earth phasing instead is presented in Figure 3.18. The variation due to phasing is reported in a different color scale to emphasize the fact that the Earth initial phasing is considered.

As expected, the behaviour obtained with the approximation of circular orbits remains globally unchanged: the contours are always identified by the Hohmann transfer curve so

the sliding of the contour do not produce oscillation. Therefore, in this reference system they are aligned with the horizontal axis. However, varying the initial Earth true anomaly θ_0, the contours translation occurs in the opposite direction with respect to what happens in Figure 3.16 varying phasing of Mars. More in detail, if in Figure 3.16 the contours arrange themselves sequentially on the right of the initial contour, the opposite happens varying Earth phasing because the sliding is caused by the anticipation or delay of one planet with respect to the other one.
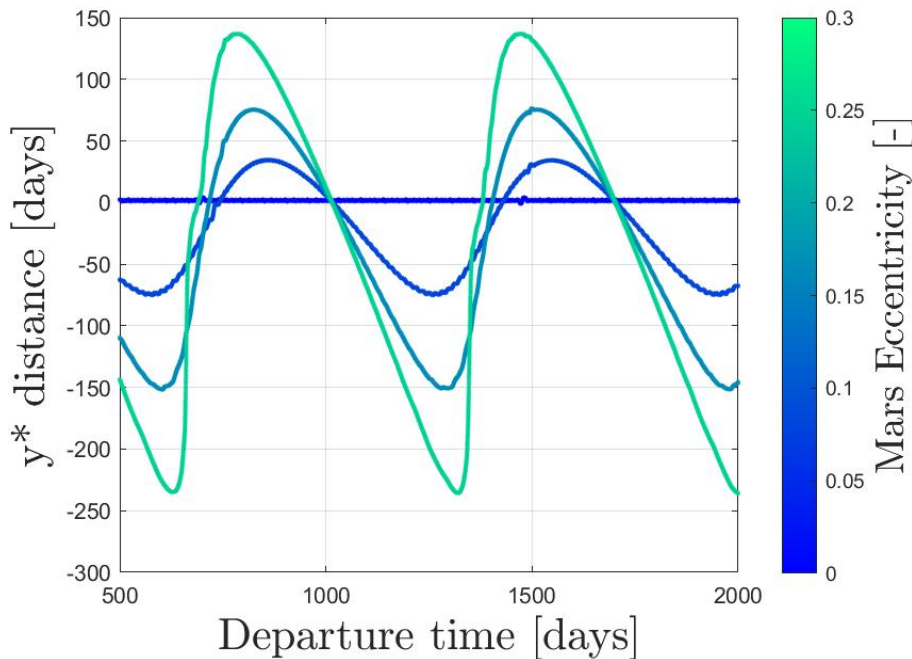
Figure 3.18: Evolution of y^* envelop due to introduced offset of Earth.

Comparing the behavior of the envelop of contours when Earth phasing is not null, the disposition follows a certain oscillating trend. For eccentricities different from zero the observable trend is that once again the contours arrange themselves following the transit lines. This time, though, the dates of Mars transits at the periapsis, which are fixed for all the different phasing of Earth.

For this reason, the frequency of these oscillations is logically lower with respect to Figure 3.17, since a peak is found any time the relevant characteristic date recurs and the period of Mars is higher than the terrestrial one.

The variation of contours due to phasing of both Earth and Mars for CLASS II eccentricity is reported in Figure 3.19. The disposition of each contour aligning with the relevant transit line is not surprising but rather totally expected. The color variation indicates the initial phasing variation. In the two graphs of Figure 3.19 the color scale is different

in order to emphasize that the planet whose offset is varied is Mars in the left image and
Earth in the right one.
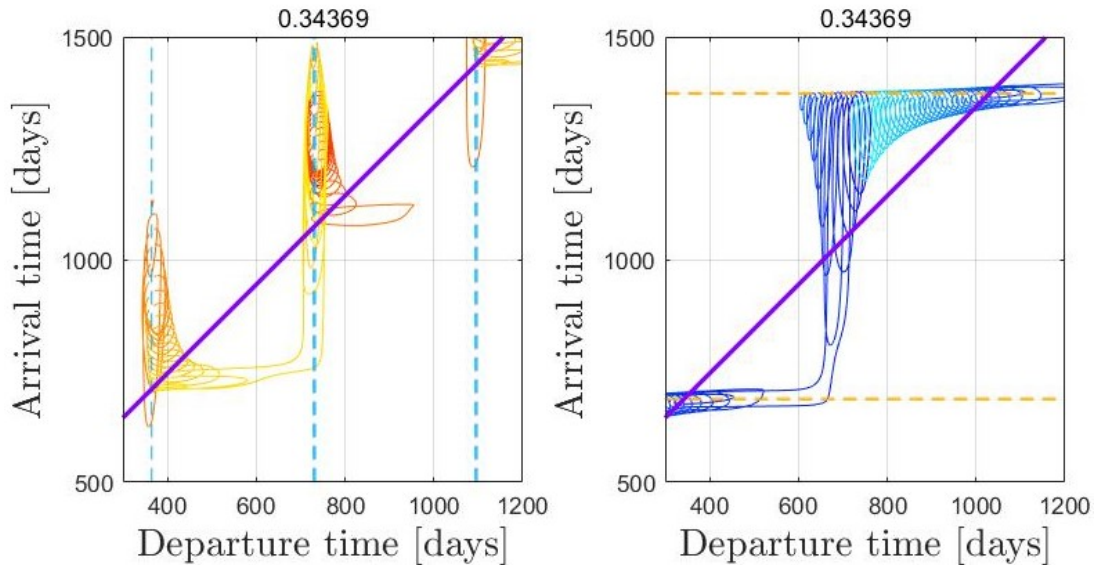
Figure 3.19: Variation of contours introducing offset of Mars (left) and Earth (right) for
CLASS II eccentricity.

Therefore, the effect of phasing can be summed up in the following way. Introducing an
offset to the initial θ of the former planets means to cause an advancement or delay with
respect to the latter. This induces a shifting of the ΔV island which slides towards one
end or the other of the Hohmann line. When the eccentricity is not zero the envelop
generated dislocates from that line producing oscillations. The transit lines are still fun-
damental since they modulates the frequency of these oscillations. On the other hand,
the amplitudes of these trends does not appear to change from Figure 3.17 and 3.18, thus
suggesting that this is linked to the size of the orbits.

Finally, an aspect which is not so clear monitoring the envelops but can be noticed through
Figure 3.16 and 3.19 is that, regardless the shape of the envelops, the transit lines attracts
strongly the position of the contours. This suggest where to look for the minimum ΔV
when designing a space transfer.

3.2.   Eccentric departure orbit

Analogously to the previous subsection, in Table 3.4 a diagram of the eccentricity ranges
for the different classes of the CE transfers is presented; immediately after, the plot
visualising the variation of the internal planet orbit is shown. Once again, the eccentricity
variation is visualised with color which scales from dark blue to light blue while eccentricity
increases and the eccentricity of CLASS II scenario is a red dashed line since it indicates
the threshold value between the other classes.

	CLASS I	**CLASS II**	**CLASS III**
range	$0 < e < e_{1tang}$	$e = e_{1tang} \approx 0.5237$	$e_{1tang} < e < e_{LIM}$

Table 3.4: Definition of classes for EC scenario.
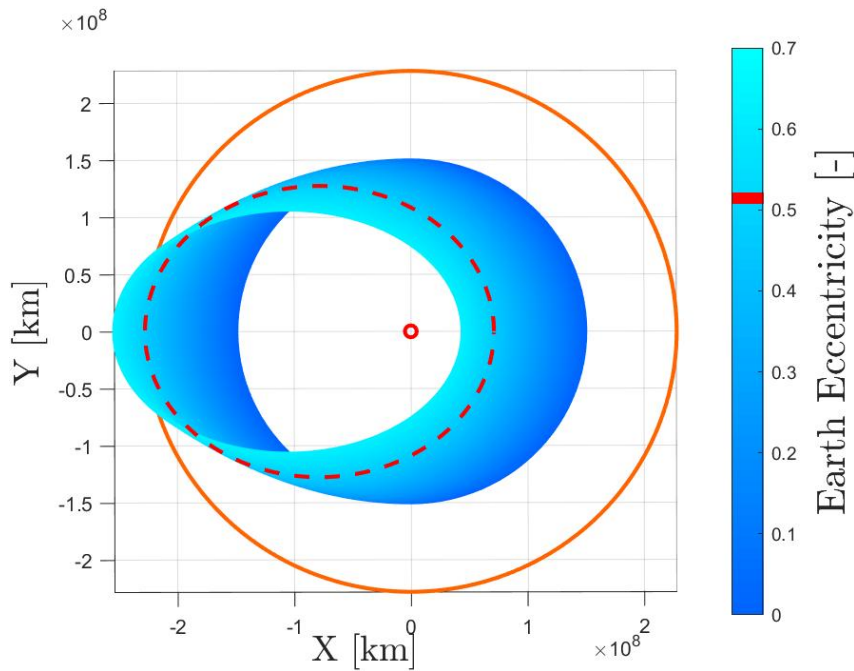
Figure 3.20: Orbit variation with eccentricity (Case 2).

In Figure 3.21 the evolution of the single porkchop plot referred to a launch opportunity is
presented. Its modification due to the different eccentricities are similar to what happens
in Case 1. This time, the island enclosing the local minimum which becomes relevant, is
located in the opposite side of the initial peak with respect to what happens in Case 1.
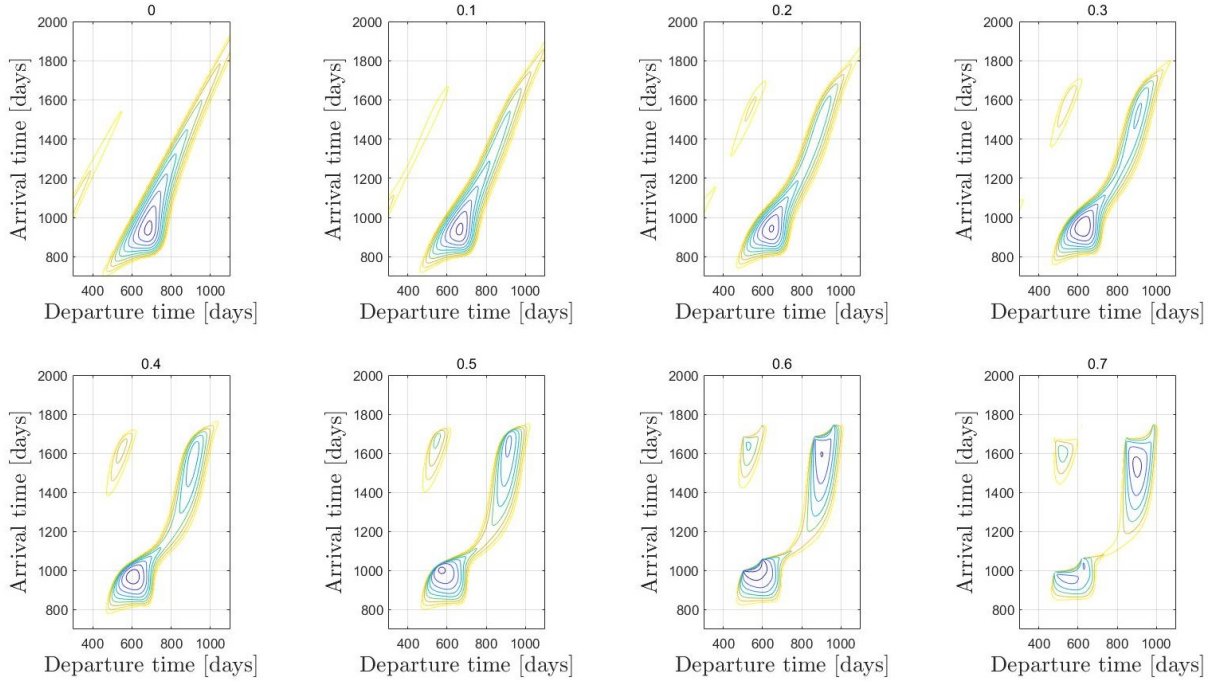
Figure 3.21: Modification of the porkchop plot for increasing eccentricity (Case 2)

The majority of the analysis carried out in Case 1 was reproduced analogously for Case 2. Some similarities and some differences are presented in the appendix A.

3.3. Role of the argument of periapsis

The argument of periapsis ω adds another degree of freedom in the analysis. Its role, indeed, introduces another complication since it follows the choice of t_{dep}, t_{arr} (or equivalently θ_{dep} and θ_{arr}), eccentricity e and initial phasing between the planets $\Delta\theta$.

As reported at the beginning of Chapter 3, the combination of the eccentricity of the orbits discriminates three different cases reported in Figure 3.22. In principle, for each of the three cases the effect of the variation of ω_1, ω_2, both eccentricities and both initial offsets with respect to eccentricity vector (which defines $\theta = 0\ deg$) could be analysed.
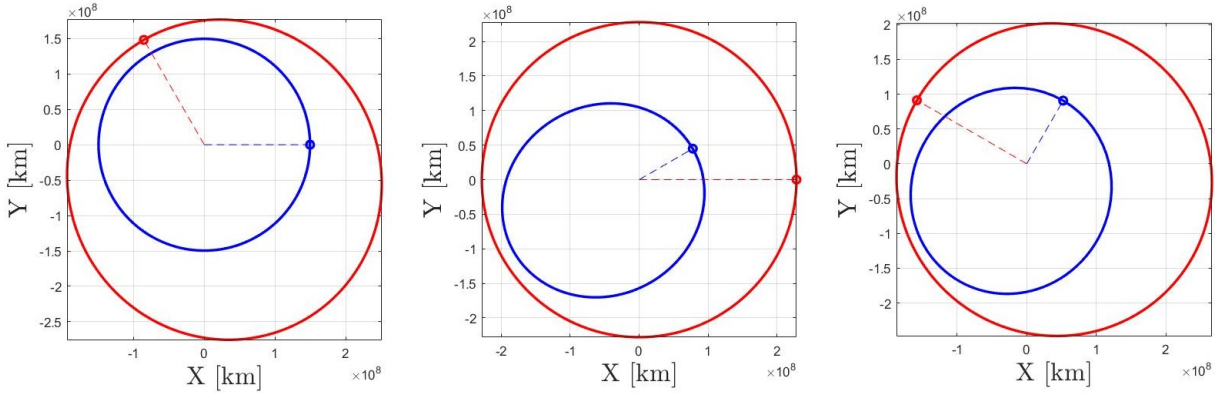
Figure 3.22: Variability of argument of periapsis in Case 1, 2 and 3.

In order to analyse properly in which way every parameter affects the envelop of the pork-chop plot, these degrees of freedom are analysed de-coupled and not together, otherwise the representation results to be chaotic. Initially, the effect of ω is analysed monitoring the Case 1 scenario, where the only argument of periapsis that matters is ω_2 because the inner orbit is circular. Analogous results are derivable for Case 2.

While analysing the effect of ω_2 alone, the phasing is freezed, so for any ω_2 the θ_2 (t_{dep}) is not modified. Consequently, the starting location of Mars at the beginning of the time vector follows the rotation of the eccentricity vector, thus modifying the coordinates $X_2(0)$, $Y_2(0)$ but not $\theta_2(0)$. X and Y represent the position coordinates of the planets in the orbital plane, so $\overline{X}$ and $\overline{Y}$ indicate that they are modified (due to a different ω) with respect to the positions x_0 y_0 obtained for $\omega = 0$.

	$\theta_1(0)$	$\theta_2(0)$	$X_1(0)$	$Y_1(0)$	$X_2(0)$	$Y_2(0)$
variable ω_2	0	0	x_{10}	y_{10}	$\overline{X}_2$	$\overline{Y}_2$

Table 3.5: Variation of Mars argument of periapsis scenario.

In Figure 3.23 the effect of variation of the contours $\Delta V = 6$ km/s due to the different orientation of the eccentricity vector of the external orbit (which is the effect of ω_2) is compared for three different eccentricities belonging to CLASS I.

Once again, the reference frame is chosen to be aligned with the Hohmann transfer line and the parameter y^* is investigated.
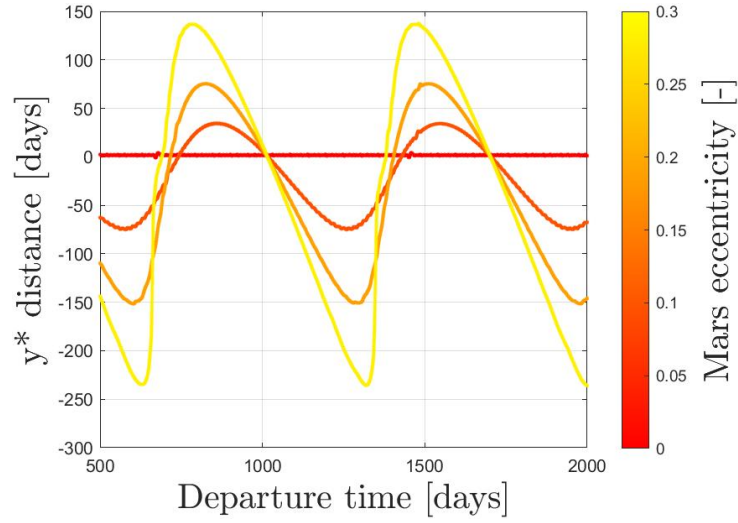
Figure 3.23: Effect of ω_2 on the trend of contours $\Delta V = 6\ km/s$ for different eccentricities (Case 1).

The effect is almost identical to what happens in presence of phasing of Earth. This is not surprising. The reference frame can be updated considering it fixed to the eccentricity vector which is rotating. In this case, there is no distinction with the situation described earlier when the Earth initial θ_2 was varied and ω_2 was fixed. This is valid because Earth orbit is circular so its eccentricity vector is not defined and the geometrical position of the point such that $\theta_1 = 0$ is not univocal. So for any eccentricity the evolution observed is analogous to what was depicted in Figure 3.18.

	$\theta_1(0)$	$\theta_2(0)$	$X_1(0)$	$Y_1(0)$	$X_2(0)$	$Y_2(0)$
variable ω_2	$-\omega_2$	0	$\overline{X_1}$	$\overline{Y_1}$	x_{20}	y_{20}

Table 3.6: Variation of Mars argument of periapsis scenario considering a reference frame rotating with the apse line.

To better comprehend the situation, the previous plots are completed with the plots in Figure 3.24 where for a fixed eccentricity (chosen to be $e = 0.3$) the behaviour of the oscillations is monitored varying freely ω_2 inside the range 0-to-360 deg but considering also different initial θ_2.

	$\theta_1(0)$	$\theta_2(0)$	$X_1(0)$	$Y_1(0)$	$X_2(0)$	$Y_2(0)$
variable ω_2, $\Delta\theta$	0	$\overline{\theta_2}$	x_{10}	y_{10}	$\overline{X_2}$	$\overline{Y_2}$

Table 3.7: Variation of Mars argument of periapsis and initial phasing.

The effect is that for these arbitrary values of the initial θ $(90, 180, 270 \; deg)$ the envelop experiences a translation with respect to the Hohmann transfer line. In this frame of reference this sliding is obviously observable as a horizontal translation whose width is around 215 $days$.
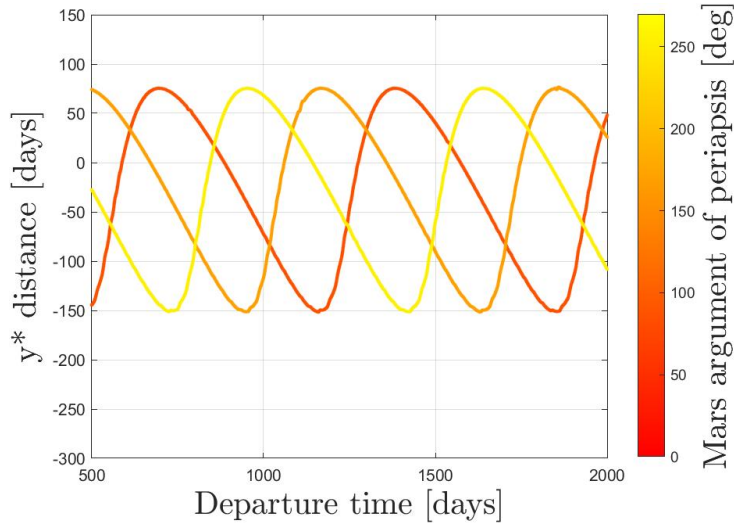
Figure 3.24: Effect of ω_2 on the trend of contours $\Delta V = 6 \; km/s$ for different initial phasing (Case 1).

The result of this analysis reveals that the effect of eccentricity is to modify the amplitude of the oscillations, while the position on this family of contours is dictated by the initial position in the plane defined by the two planets. This can be affected by two factors: the orientation of the periapsis (ω) which is fixed for any real orbit and by the phasing (θ) which varies from one launch opportunity to the following one.

Finally, it is possible to analyse the effect of ω_2 as decoupled from the phasing. In other words varying the orientation of the eccentricity vector removing the effect of phasing, the initial position of Mars does not have to follow the imposed rotation of the apse line.

	$\theta_1(0)$	$\theta_2(0)$	$X_1(0)$	$Y_1(0)$	$X_2(0)$	$Y_2(0)$
variable ω_2	0	- ω_2	x_{10}	y_{10}	$\overline{X_2}$	y_{20}

Table 3.8: Variation of Mars argument of periapsis scenario decoupled from phasing.

This way, Mars is always aligned with Earth and Sun at t_0 and the modification of porkchop plot is only caused by the orbit orientation (ω_2).
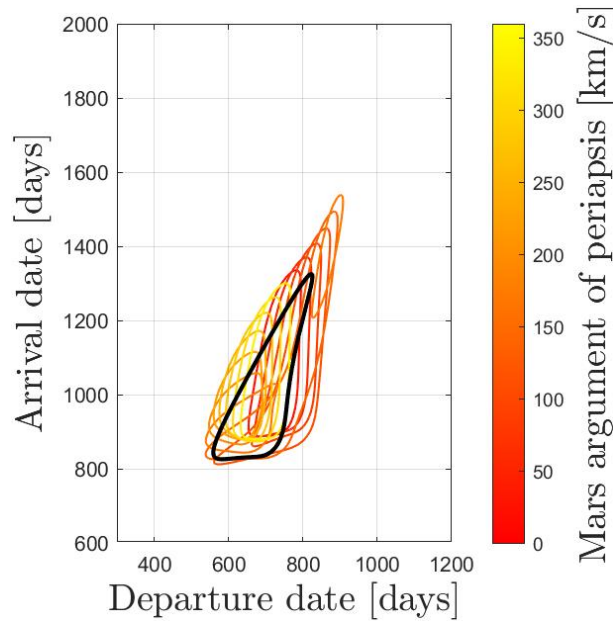
Figure 3.25: Variation of the ΔV contour caused by the orbit orientation (*omega*) decoupled from phasing.

This time, the definition of an envelop would be impossible, since the sliding along the Hohmann line does not occur. The variation, instead, consists in modifying the shape and slightly the location of the contours. Indeed they are maintained in the region defined by the porkchop plot obtained for circular orbits and with null phasing (planets aligned at t_0) reported in black.

This result shows that the sliding along the Hohmann line is caused by the angular distance between planets at t_0, either induced by phasing or by ω. Contrarily, the rotation of eccentricity vector alone does not imply a sliding but for any ω concentrates the contours in a specific region. Whatever the orbits orientation is, the region of the plot where expecting to find the contours depends on the initial angular distance between the planets.

3.4.   Eccentric departure and arrival orbits

Case 3 of this dissertation would consider the modification of porkchop plot when both eccentricities are considered. In this case, however, the effect of eccentricity would have two separate degrees of freedom since the eccentricity of one orbit and the other are independent. For this reason, Case 3, which in some cases embeds the concatenated effects of the previous 2 cases, is treated here briefly, without repeating the results which are common to the previous scenarios.

Given the splitting of one single degree of freedom into two different ones, it is not easy to track and distinguish on the same graph the effect of both the two eccentricities at the same time. This leads to the need of referring to parameters which can be helpful to understand the situation. In addition to the minimum ΔV inside a time window, the modification of specific contours is monitored. Given for example the contour level $\Delta V = 10 \ km/s$, it is possible to analyse the area occupied by such a contour on the porkchop plot building a quadrilateral region which bounds the contour in its four most extreme cardinal points. Successively, it is easy to calculate analytically the value of the interested area. Reminding what has been discussed previously in Case 1, enhancing the eccentricity the minimum ΔV (as well as the contour itself) moves on the plane being attracted by specific dates. The following step is to analyse how the trend is modified considering the eccentricity of the Earth too. To do so, the θ domain is used. Considering an arbitrary contour level, the quadrilateral enclosing precisely the contour is built to delimit the region and compute the θ ranges. Then the process is repeated for all the eccentricity considered. Mars eccentricity is expected to move the θ ranges enclosed by that contour around the multiples of 2π, at least this is the effect when Earth eccentricity is null. In this domain, the centre of each quadrilateral can be used as indication of the mean value of the departure θ, and the distance between this value and the multiple of 2π is called $\theta_{Mismatch}$.

$$\theta_{mean} = \frac{min(\theta_{dep}) + max(\theta_{dep})}{2} \tag{3.12}$$

$$\theta_{Mismatch} = \theta_{mean} - 360 \ deg \tag{3.13}$$

In this figure it is possible to observe the trend of the mismatch as a function of e_2. The multiple curves describe the situation for the respective value of e_1 (described in the legend).
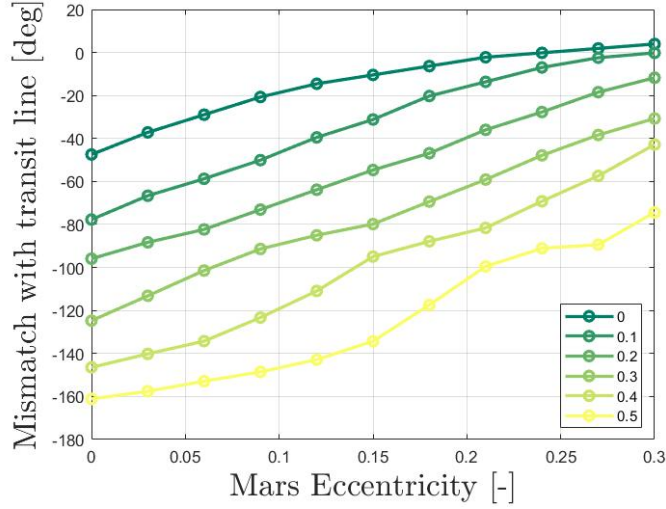
Figure 3.26: Mismatch between the θ_{mean} and the asymptotic condition (360 deg) as a function of eccentricity.

The top curve in the graph shows the expected trend already described earlier: when $e_1 = 0$, increasing e_2 the contour is attracted by the transit line and consequently $\theta_{Mismatch}$ tends to zero. Considering now all the other curves, it is possible to deduce that the effect of e_1 behaves as a disturbance with respect to what has been previously described. It is possible to confirm the tendency of the Mars eccentricity to reduce the mismatch but, in the end, the introduction of the Earth orbit eccentricity produces a monotonic effect in the opposite direction. This effect can be analysed making reference to the minimum ΔV whose trend can be analysed for varying values of e_2, having fixed the specific value of $e_1 = \bar{e}$ as in the left plot of figure 3.27. Next to this plot, the same analysis is performed monitoring the surface on the porkchop plot enclosed by the contour level $\Delta V = 10\ km/s$.
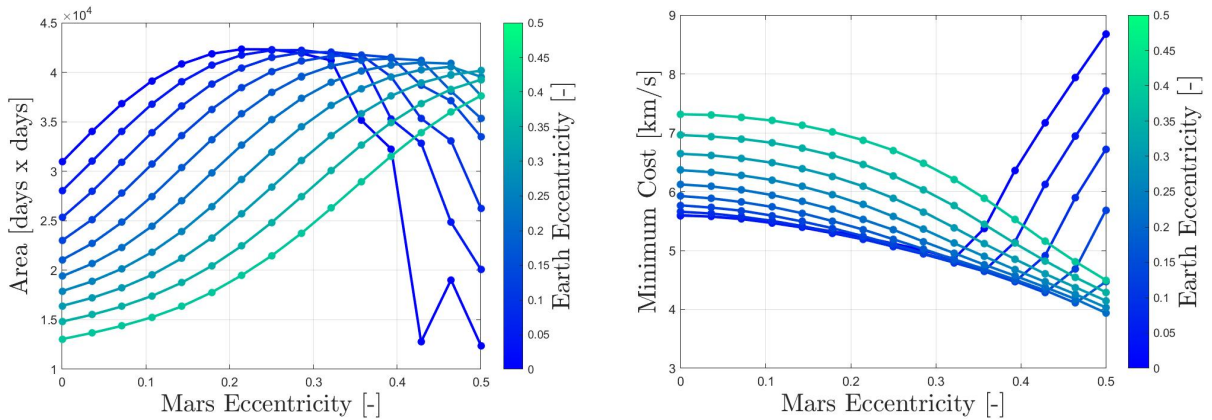
Figure 3.27: Variation of the area enclosed by specific contour (left) and minimum transfer cost (right) as a function of e_2 with the disturbance caused by e_1.

In both cases for e_2 of CLASS I (low values on x $axis$) the effect of e_1 (expressed in the colorbar) is to decrease the performance: the area in which the transfer under a specific ΔV threshold is feasible reduces when increasing the inner planet eccentricity. Similarly, the minimum transfer cost raises, showing the contrary effect of the two parameters when moving slightly away from the y $axis$.

However, in case of higher e_2, an effect which is clearly against the trend is visible.

In the case of the curve obtained for circular Earth orbit, it has been shown how the minimum is reached in case of the CLASS II scenario, where the two orbits are tangent. The couple of eccentricities describing the CLASS II situation was calculated as $e_1 = 0$ (hypothesis) and $e_{LIM} = e_2 \approx 0.3437$. However, when e_1 is no more zero the previous value of e_{LIM} does not identify anymore the CLASS II scenario. Indeed, the e_2 such that the two orbits are tangent must be recomputed and results to be higher than before.

e_1	0	0.1	0.2	0.3	0.4	0.5
e_{2LIM}	0.3437	0.4093	0.4750	0.5406	0.6062	0.6718

Table 3.9: Variation of e_{2LIM} identifying the CLASS II scenario as a function of e_1.

For this reason, when the curves cross each other lower transfer possibilities are found at higher eccentricities. Indeed, just like Woolley and Whetsel [36] have shown, when considering the eccentricities of the orbits, the minimum ΔV value decreases with respect to the case of a Hohmann trajectory, which is the minimum cost transfer between circular orbits. This result expands the previous one by noticing that the reduction in the manoeuvre cost is monotonic with the eccentricity, so when both e_1 and e_2 are high the transfer cost is reduced.

In order to generalise this result and observe the concurrent effect of both eccentricities at the same time, parameters such as the ΔV minimum and area A enclosed by the contour are summarised in the following plots. Indeed, expressing these parameters as a function of two independent variables (e_1, e_2) a 3D surface can be computed to evaluate the magnitude of the relevant parameter.
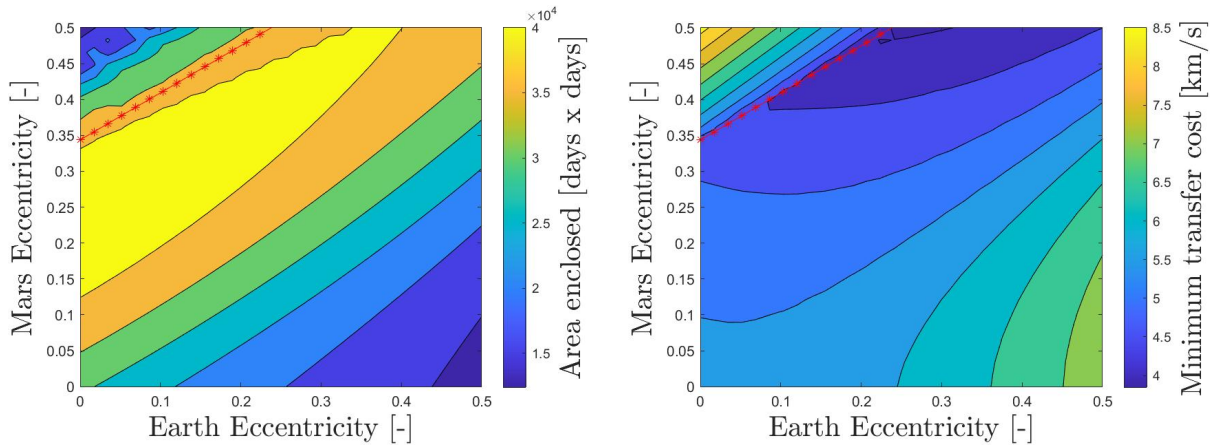
Figure 3.28: Areas interested by $\Delta V = 10 \ km/s$ contour (left) and minimum ΔV magnitude (right) as a function of any combination of e_1 and e_2.

This couple of plots embeds the results obtained in the sections considering the eccentricity of one planet at a time. These information, indeed, are visible just moving on the two axes where e_2 varies and $e_1 = 0$ or vice versa.

Moreover, the additional information on how the respective parameter is influenced by the modification of the orbital dynamics due to any combination of Earth and Mars eccentricity is described in all the other regions of each graph. First of all it is worthy to notice that, moving in the horizontal or vertical direction does not induce the same effect on the parameters under study. There is no "commutative property" in this scenario: switching the values of e_1 and e_2 produces indeed a completely different situation.

The right plot is the one displaying the minimum possible cost of an orbital transfer between two orbits given their eccentricity. From this plot emerges once again how the cost decreases when getting close to Mars eccentricity of CLASS II (reported as a red line). It is important to point out that this couple of graph is produced in correspondence of null phasing. Different results may be found in correspondence of other initial $\Delta \theta$, but this would introduce a further degree of freedom complicating very much the dissertation.

All the previous analysis can be performed abandoning the Earth-to-Mars case and considering two generics celestial bodies. In this case the dynamics would behave similarly. The differences would regard mainly the frequency of repetitions of the ΔV islands since they are dictated by the semi-major axis which influences the synodic period. The minimum would be modified consequently both in terms of location and magnitude, while the value of eccentricities identifying the CLASS II scenario would be modified considering the relation expressed in Equation (3.1). The significant aspects are preserved but would be scaled in the epoch space, as well as the transit lines.

4 | Transfer among inclined orbits

In this chapter, the role of the inclination of the orbits of the two planets is examined in order to assess its effect on the morphology of ΔV porkchop plots.

The RF is once again the one described at the beginning of Chapter 3. For this reason, all the inclinations considered case by case are always referred to the Ecliptic plane. Moreover, in this chapter the eccentricity of both orbits are equal to zero in order to separate clearly the effect of inclination.

In principle the inclination of the orbits of the planets can vary from -90 to 90 deg. However, analysing the inclination of the orbits of planets and moons in the Solar System, a big part of this scale of values can be discarded. Indeed, the orbits of planets of Solar System are almost coplanar apart from few degrees [26]. Their actual values are reported in the Table 4.1.

Planet	Mercury	Venus	Earth	Mars	Jupiter	Saturn	Uranus	Neptune
Inclination	7 °	3.4 °	0 °	1.9 °	1.3 °	2.5 °	0.8 °	1.8 °

Table 4.1: Inclination of planets orbits in Solar System.

Furthermore, among all the system of moons of Solar System less than the 20% of the moons have orbits inclined more than 30 deg and none of those belong to big moons. Therefore the focus has been shifted to the ranges of inclination from 0 to 30 deg and from -30 to 0 deg. Whenever the transfer involves asteroids or minor bodies, the ranges have to be expanded.

Analogously to Chapter 3 the analysis on the effect of inclination must be carried out considering the variation of one of the two orbits at a time. In order to help distinguishing between the cases of this chapter without confusing them with the previous characterisation, the following notation is adopted:

- Case 4: Planar-to-Inclined transfer (PI) in which only Mars inclination varies;

- Case 5: Inclined-to-Planar transfer (IP) in which only Earth inclination varies;

- Case 6: Inclined-to-Inclined transfer (II) in which both inclinations are considered.

Moreover, considering the two ways in which one orbit can tilt with respect to the ecliptic plane, another classification is introduced based on the angle η between the ecliptic plane and the plane on which the inclined orbit is laying.

$$\eta = i_{VARIABLE} - i_{ECLIPTIC} \tag{4.1}$$

where $i_{VARIABLE}$ is the inclination imposed to one of the two orbits, while $i_{ECLIPTIC}$ is the inclination of the other orbit, since it is meant to lay on the ecliptic plane. The orbits considered are always prograde and three different families are recognised depending on the situation:

- Family A: η positive;

- Family B: η zero (coplanar case);

- Family C: η negative.

All the described scenarios are depicted in Figure 4.1 where the color scales in order to better visualise each orbit with its own inclination. The color changes with the inclination and for a better visualisation two different color scales are used when considering the inclination of Mars (left) and Earth (right).

In all these images the green dashed line represents the *line of nodes* that is the imaginary line identifying the intersection of the each inclined plane with the plane of reference (the ecliptic one). At this stage, the RAAN of both orbits is imposed as zero, consequently the line of nodes remains fixed throughout the following analysis.
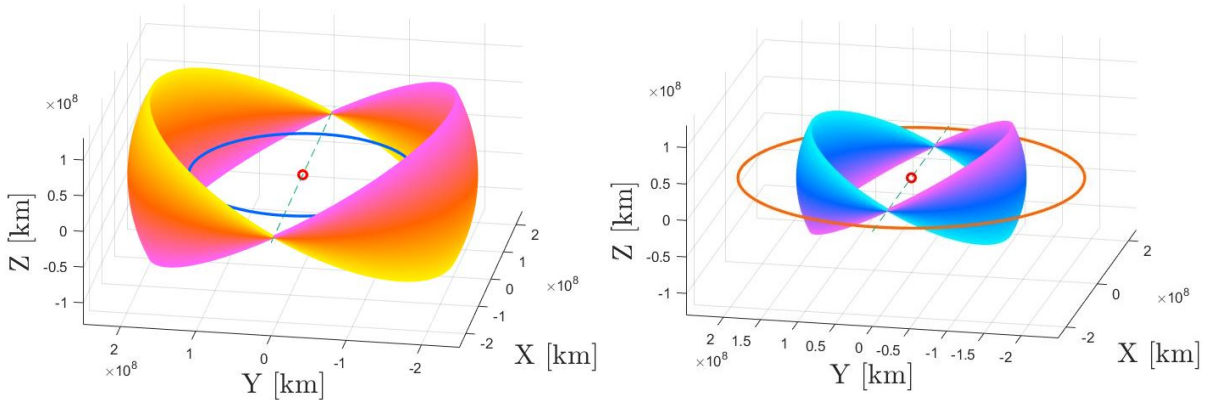
Figure 4.1: Orbit inclinations considered (Case 4 and 5).

4.1. Inclined arrival orbit

Starting with the Family A of Case 4, the analysis is produced for different values of i_2 between 0 and 30 deg and the porkchop plots in Figure 4.2 are produced. The same inclinations with the opposite sign (Family C) generate ΔV contour lines that are identical to the ones produced in the Family A case. The problem is indeed symmetric with respect to the ecliptic plane. This result is not unexpected since the dynamics of the planet whose orbit is inclined does not vary mirroring it with respect to the plane at $Z = 0$. Furthermore, switching the planet whose orbit is progressively inclined, the result does not vary: the porkchop plot remains identically unchanged. Then, the scenario described by Case 4 and Case 5 is equivalent. In other words, what matters is not the actual values of i_1 and i_2 but just the difference $|\Delta i|$ between them.

Considering the regularities just described, from now on the analysis is carried out just using the Family A of Case 4 to show all the results. Figure 4.2 shows the ΔV contour lines obtained for different inclinations.
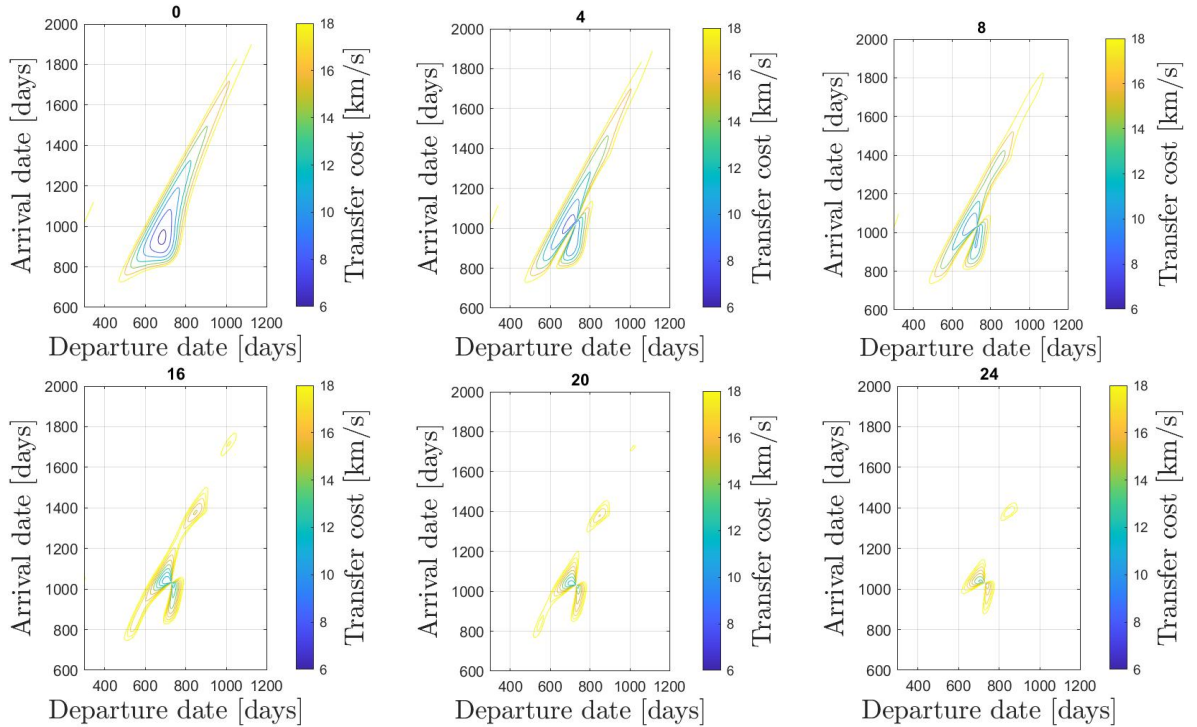
Figure 4.2: Porkchop plot for Case 4 and 5, Families A and C.

For a matter of aligning to existing conventions, the Earth is considered to lay on the ecliptic plane while Mars inclination is varied.

Consequently, the RF is centred in the Sun and defined as follows:

1. *X axis* aligned with the vernal equinox;

2. *Z axis* aligned with terrestrial angular momentum vector;

3. *Y axis* consequently directed according to right-hand rule;

The martian orbit intersects the ecliptic plane in two points defining the line of nodes. All the other points along the orbit are found accordingly at different quota Z.

Moreover, Case 6 does not add any complication. Even considering both i_1 and i_2 different from zero, the RF can be rotated in order to modify Earth inclination, thus recovering a scenario described by Case 4.

From a visual perspective, as noticed by Woolley and Whetsel [36], as the inclination is increased after a certain value (around 1 *deg*) the ΔV island is divided in two lobes due to the appearance of a ridge between them. This ridge gets bigger as the inclination is increased, so that the two lobes becomes more and more distant except from a small interval of dates in which always exist a connector between the two islands. For this reason, this point is known with the term *bridge* in the work of Woolley and Whetsel [36].

The effect is quite different with respect to what happens when the eccentricity is considered. The ΔV island is not just modified in terms of shape but also in dimension. The area enclosed by the more external contour level decreases indeed while the inclination increases. First, the main island is divided giving birth to smaller ones, then its area drops drastically passing 20 *deg* of inclination.

In Figure 4.3 a single contour level (i.e. $\Delta V = 10$ *km/s*) is considered and its location and size is compared for different values of inclination. The contours obtained can be observed superimposed on the same graph to be one inside the others, identifying clearly the miniaturisation. Contrarily to eccentricity, the inclination does not play a role in the evolution of θ. As a result, in this case the ΔV island are not distorted but simply reduced. The reduction in shape is driven by the increased inclination since the larger the change of plane the higher the ΔV costs.

Together with that, the plot with the different minima location for increasing eccentricity is flanked. For both graphs the colour scales from dark blue to light blue increasing the relative inclination between the orbits. The most interesting results obtained through these plots are linked to the behavior of the contours with respect to the relevant lines present in the picture. In the same way of Chapter 3, the diagonal dotted line represents the locus of solutions having a transfer angle of 180 *deg*. In this case the shape of this locus of solution remains unaltered with increased inclination, contrarily to what hap-

pened increasing eccentricity (see Figure 3.13). Other relevant lines are the horizontal and vertical lines which this time represent the dates of transit of each planet over the line of nodes.
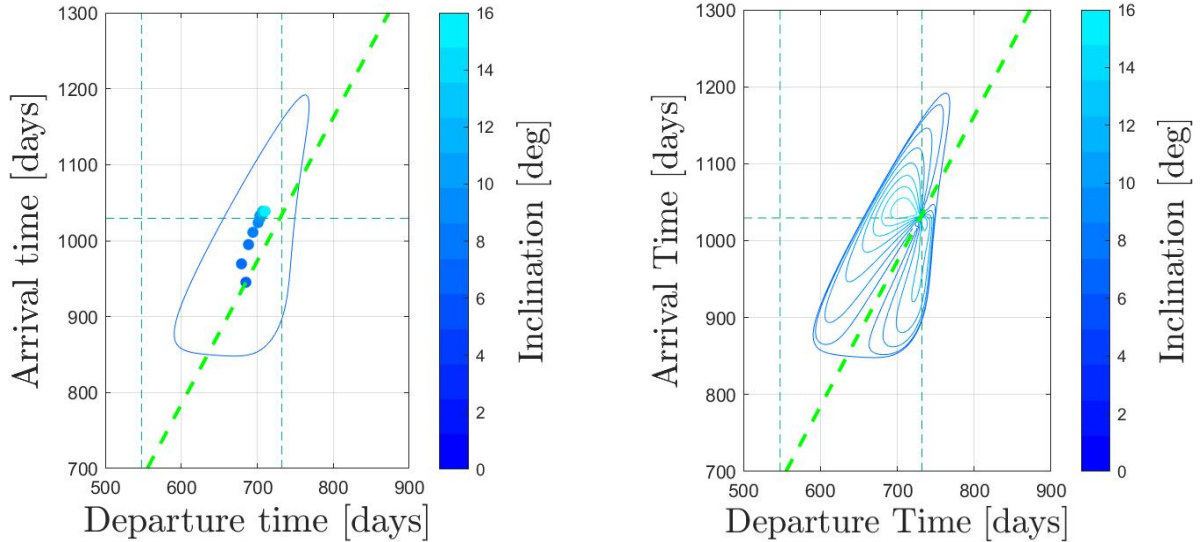
Figure 4.3: Effect of inclination on minima location (left) and on specific contour levels (right) i.e. $\Delta V = 10 \; km/s$.

The left plot in Figure 4.3 highlights how the location of the minimum ΔV for a specific launch opportunity modifies its location. For zero inclination, indeed, the location of the minimum is identified by the line of solutions having $\phi = 180 \; deg$, as the problem falls into the simpler coplanar case, already described by Menzio [22]. However, whenever the inclination is enhanced, the minima moves, being attracted by the closest among the intersection points between an Earth transit line and a Mars transit line. In other words, the research reveals that the more convenient solutions at inclination different from zero are those which foresee both a departure and arrival close to the line of nodes.

In addition to that, the right plot helps recalling an important feature of this problem which is the fact that the ridge is identified on the graph exactly by the line of 180 deg transfer which separates clearly the two lobes as pointed out by Woolley and Whetsel [36].

Figure 4.3 underlines that the position of the bridge is found where both the lines of transit from nodes meet the 180 deg transfer line. In other words, the only eventuality in which the transfer having $\phi = 180 \; deg$ is possible is when departure and arrival point both lay on the line of nodes. Increasing the inclination the locus of minima must move away from the 180 deg line because of the generation of the ridge. At the same time, the minima are attracted by the only point (when $i_2 \neq 0$) that admits $\phi = 180 \; deg$: the bridge. In other

words low ΔV solutions tend to emulate as much as possible a Hohmann-like transfer.

A clarification is needed to explain why the locus of solution $\phi = 180 \ deg$ is not varied with inclination. This is due to the circularity of both orbits and consequently of proportional true anomaly variation with time, as expressed in Equation (2.13). This can be compared with Chapter 3, where contrarily the eccentricity do have an effect, visible in Figure 3.1. As a result, the contour lines having constant ϕ consist in straight lines with fixed slope. Its value depends in fact only on the size of the two orbits, which dictate the synodic frequency through Equation (2.16). Precisely, it is a function of the difference between the semi-major axis of the two orbits. The more the two orbits have similar size, the more the fan gets close to the slope of 45 deg, while the higher is the difference between the radii the more the lines get close to become parallel with the vertical direction. The fan of ϕ lines is shown hereafter in Figure 4.4 together with the contour line relative to arbitrary i_2 and ΔV level, here in black, that has its characteristic aspect. The effect of i_2 is limited to the variation in area of the contours and overall cost of the transfer.
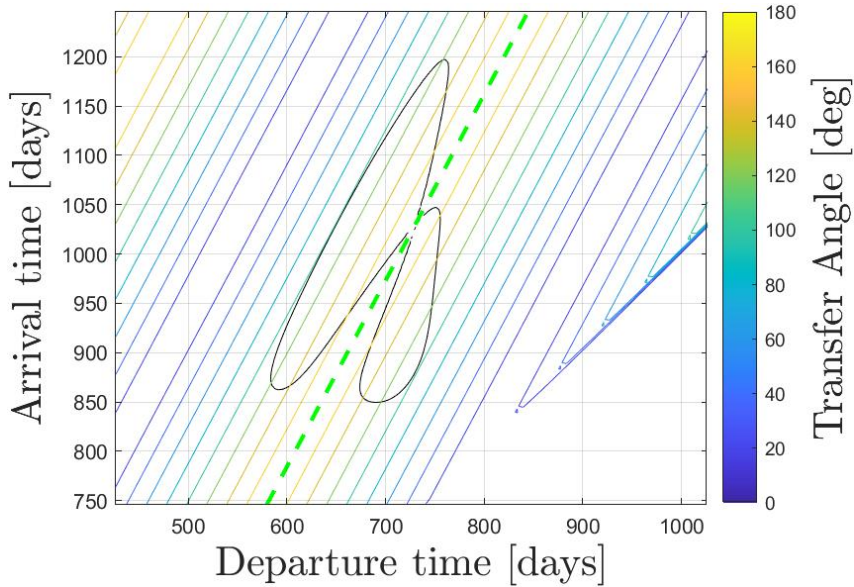
Figure 4.4: Constant ϕ fan with respect to a generic ΔV contour.

Furthermore, the regularities dictated by the line of node transits can be analysed. The porkchop plot is produced for a time window in which two main islands exist. In this case, for the sake of clarity, the date of transit over the ascending node is drawn in green as before, while the line referred to the transit over the descending node is drawn in bordeaux in order to be distinguishable.
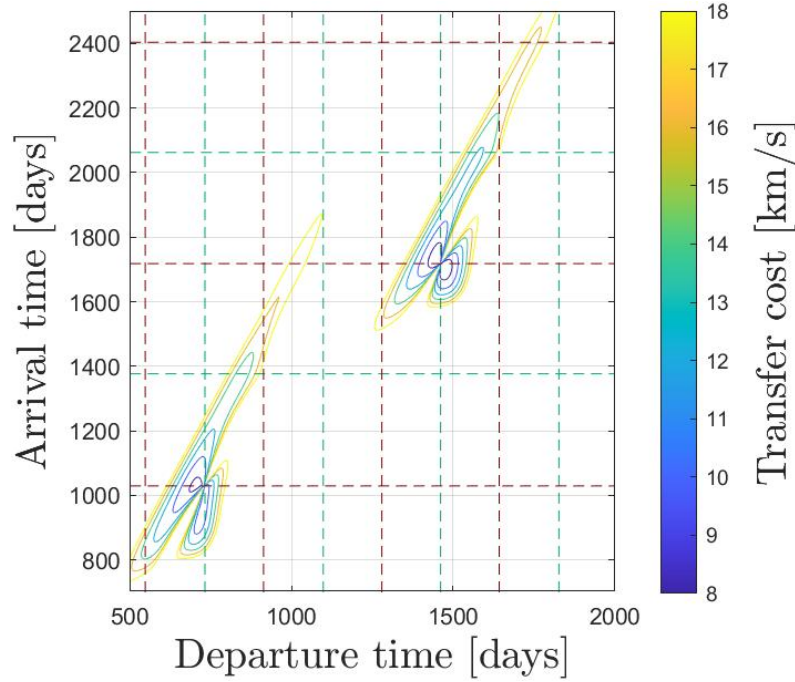
Figure 4.5: Porkchop Plot highlighting transit lines over two launch opportunities.

First of all it is noticeable how the two islands are similar in shape but not exactly the same. The same effect was obtained in the eccentricity case, with larger distortion. The reason was attributable to the phasing whose effect was magnified by eccentricity, differently from this case. The phasing plays a role also for inclination because for different phasing the alignment occurs at different θ along the orbits, thus having difference in the quota Z.

More interesting in this plot is the visual distinction between the dates associated to the ascending and descending node. Figure 4.5 shows that the bridge location (always laying on the 180 *deg* line) in each island it is found in correspondence of the solution having the departure from the ascending node and the arrival at the descending node. Observing the graph, a bridge is located on the porkchop plot every four transit of the Earth over the line of nodes and every two transit of Mars over the same line. The repetition of this pattern is linked to the synodic period, as already reported in literature, but the two effects are not the same. In correspondence of any launch opportunity a ΔV island is generated, so one every 2.14 years. A bridge, instead, is found on the porkchop plot every 2 years since its position is dictated by the transit lines. The slight difference between these two repetition periods quantifies the diversity with respect to the circular case where a peak was found every synodic period. This regularity allows to identify a priori the locus of the bridge, without running the algorithm but just observing the characteristics of the orbits.

The dates associated to other intersection points found on the plot between two successive bridge locations present ΔV higher than 20 km/s so they are not convenient. This was not expected, given the circular nature of the orbits, since generally a transfer starting from descending node of Earth and arriving at ascending node of Mars will have a similar trajectory (thus a similar cost) than the other way round. This is once again due to phasing. Indeed, for certain values of the initial phasing (here not considered), the bridge location will be identified actually by the solution departing from Earth at the descending node and arriving at Mars at the ascending node. This is properly due to the discrepancy between the synodic period and the interval between two transits over the line of nodes. Solutions identified at the intersection point between transit lines at the ascending (descending) node for both planets present high ΔV, since these present generally high TOF or high ϕ.

Departure and arrival ΔV contour plot

First of all, even considering separately the two impulsive manoeuvres, the symmetry discovered at the beginning of this Chapter 4 is preserved. The contour plots of the departure and arrival ΔV generated for Case 4 and Family A describe all the possible scenarios.

With the same hypotesis of Figure 4.5 (no phasing considered), it is possible to evaluate how the ΔV is distributed between the two manoeuvres. The contour plots generated and displayed in Figure 4.6 help shedding a light on what happens when departing from descending node and arriving to ascending node, focusing on the region of the ridge. In correspondence of these dates, multiple bridges are formed, revealing that actually these combination of dates are theoretically relevant. However, when summing the cost of both manoeuvres, the combination results in ΔV lower than the threshold only for the dates associated to the main bridge.
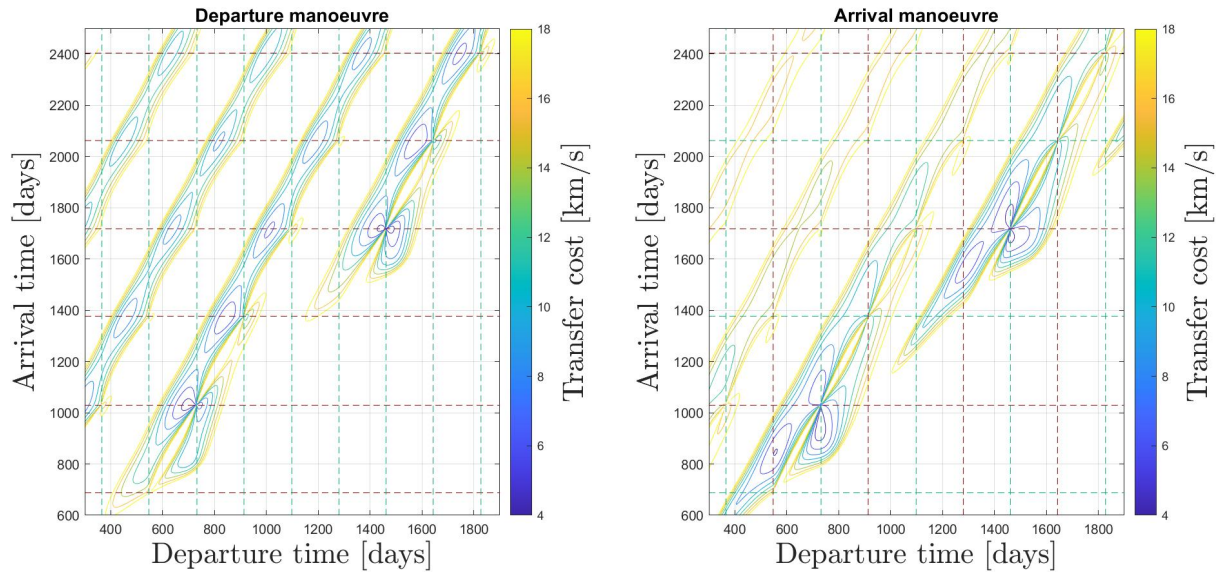
Figure 4.6: Contour Plot for departure (left) and arrival (right) manoeuvre.

More in detail, each contour plot sees its left lobe getting populated by small islands at low ΔV (in addition to the main one) which disappear in the total ΔV graph since their counter part is at high cost. In the departure plot they are found for higher departure and arrival time; in the arrival one, they are found for earlier dates.

From the morphology point of view, another insight can be visualised from the plot of the contour lines at one specific ΔV level for increasing values of inclination. This allows visualising on the same graph which is the separate effect of inclination on the two manoeuvres of the transfer. In Figure 4.7 the contour at $4\ km/s$ are observed for a range of inclination (described with the color scaling) such that the variation is significant.
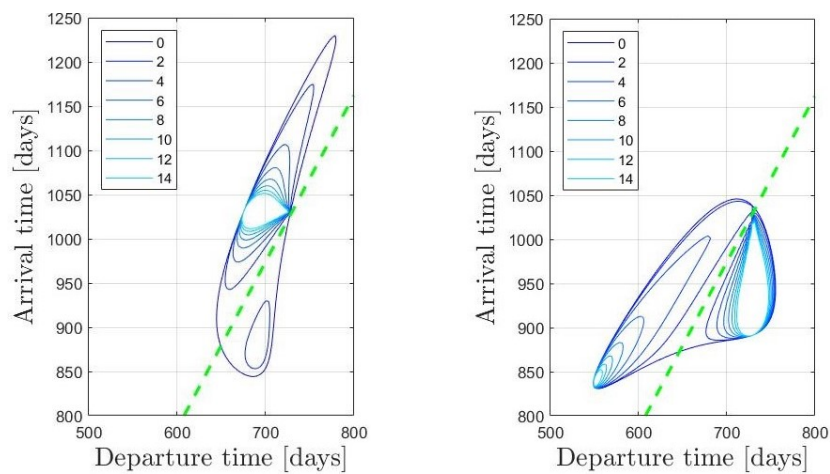
Figure 4.7: Effect of inclination in modifying the contour levels (i.e. $\Delta V = 4\ km/s$) related to departure (left) and arrival (right) manoeuvres.

In the two subplots, the two lobes in which the contour plot is divided by the 180 *deg* transfer line show two different trends. At departure it is observable that all the contours in the left lobe are connected to the bridge even when inclination reduces their area, while below the 180 *deg* line the contours at this specific level tend to disappear after a certain inclination, giving no way to perform transfers in that region of time. The opposite instead happens in the right plot where in the right lobe are produced contours which are connected to the bridge and in the left one the contours are distanced from the ridge and dislocate reducing their dimension in a more observable way.

Increasing the value in the contour level the area enclosed by each curve increases and new areas are formed because the separate manoeuvres have more than one bridge.
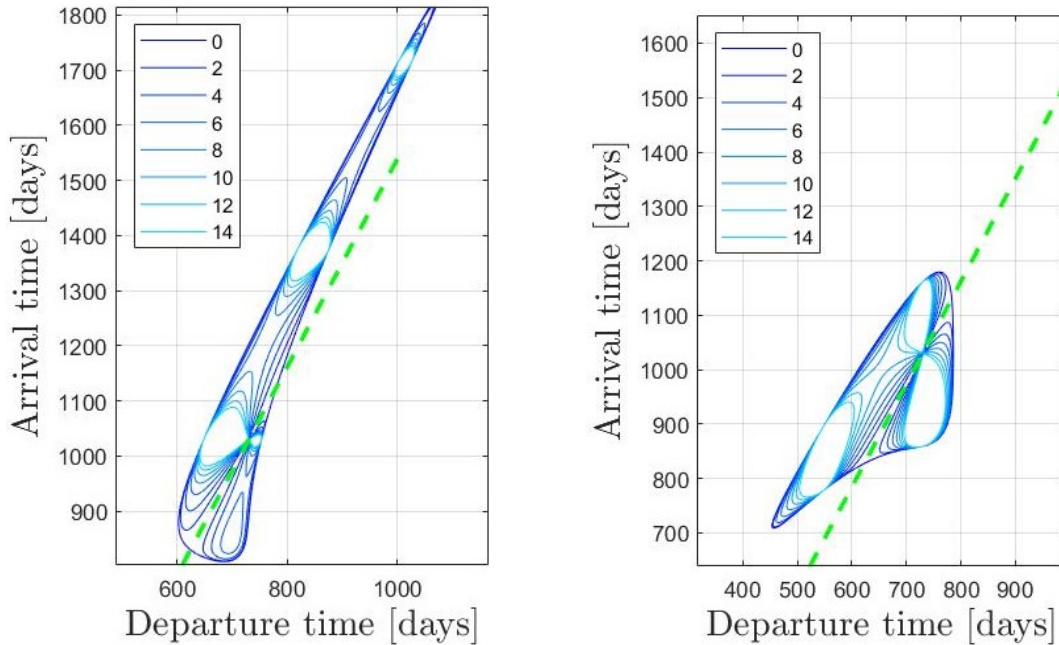
Figure 4.8: Effect of inclination in modifying the contour levels (i.e. $\Delta V = 6 \ km/s$) related to departure (left) and arrival (right) manoeuvres.

The bridge now connects again the contours on both the two lobes but the admissible regions are not limited to the region close to the bridge. For both the departure and arrival plot, the effect of inclination is to reduce the area of regions in which a manoeuvre at specific cost is possible. The ΔV island does not experience just a miniaturisation but more a fragmentation. Increasing the relative inclination, in both plots of Figure 4.8 the left lobe is populated by smaller and smaller regions in which is possible to operate a transfer, each one emerging in correspondence of transit lines where a local bridge is formed as described in Figure 4.6.

An interesting aspect comes from the analysis of the transfer orbit and how it is inclined. Especially, it is worthy wondering how the change of plane is performed and divided in the two different manoeuvres. Being the change of plane an expensive manoeuvre, it is expected that most of the inclination is changed when further from the Sun.

To do so, the contour plot of the inclination ratio ψ defined as follows has been performed.

$$\psi = \frac{i_{transf}}{i_2} \tag{4.2}$$

where as usual i_2 represents the total Δi since i_1 is zero. Similarly, i_{transf} represents the inclination with respect to the ecliptic plane.

A really important aspect is that this ψ plot does not vary when the relative inclination is increased, thus indicating that no matter the Δi the ratio of the total inclination covered by the first manoeuvre is the same. The result is reported in Figure 4.9.

Figure 4.9: Contour plot for the parameter ψ.

Limiting ψ in the interval of interest from 0 to 1 (so considering only the transfer or-

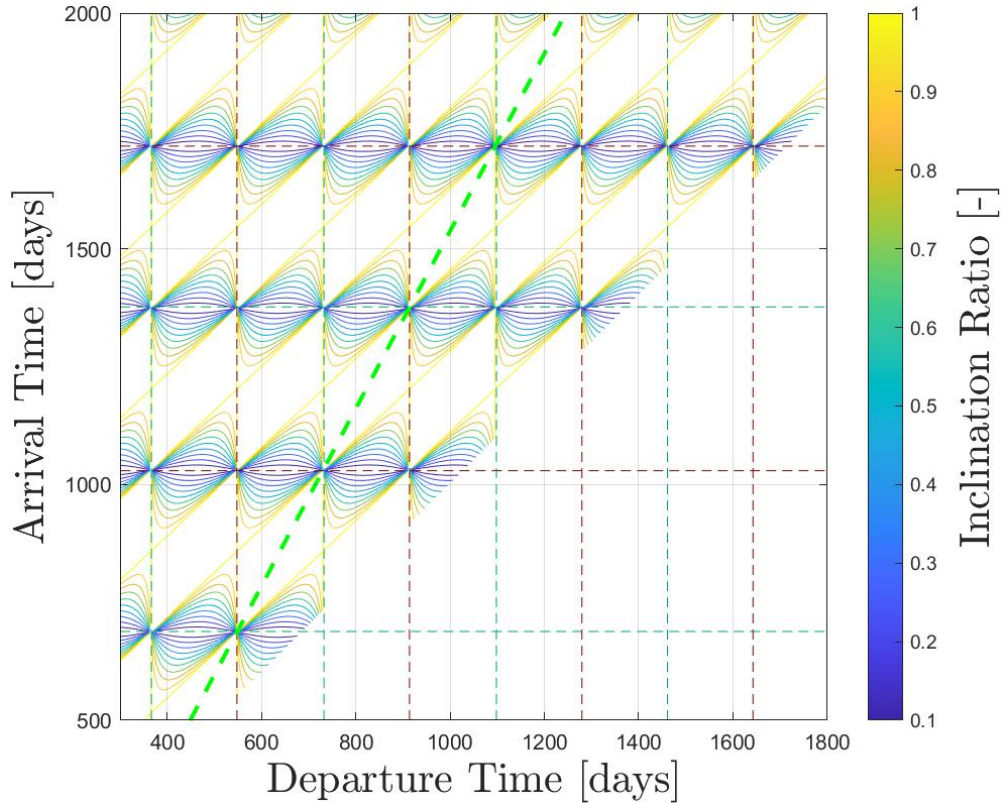bits which have an inclination lower than the one between the orbits) many identical rhomboidal islands populates the ψ plot in a symmetric order which, once again, align with the transit lines. Figure 4.9 shows that the rhomboids have two sides lying over the departure planet transit lines and two transverse sides inclined by 45 *deg*. All the rhomboids are connected to each other at the node crossings generating on the plane a sort of "chequerboard effect". They divide the epoch space in areas in which the transfer is possible through orbits having ψ lower than 1 and higher than 1.

The empty rhomboids are not regions in which the transfer is not possible. Some of them are crossed by the 180 *deg* transfer line, region in which the transfer is possible only in correspondence of the aforementioned bridges. However, a fraction of these rhomboids is not off limits, and this is seen extending the interval of interest, in example for ψ from 0 to 2. Figure 4.10 shows how the rhomboids extend their extremities in the diagonal directions connecting each other in rows parallel to the 180 *deg* transfer line, and so parallel to the ridge. This means that actually the 1 does not represent an upper limit for the parameter ψ: in some cases the transfer orbit must be more inclined than the arrival orbit with respect to the ecliptic plane in order to match the TOF and ϕ considered.

Moreover the adjacent rows of rhomboids have an alternated nature: they are referred to the two orbit solutions present in the theory of Lambert problem [27]. Indeed, considering the two rows adjacent to the 180 *deg* line, it separates the long transfers on the left and short transfers on the right. These are also the two rows of rhomboids which are interesting in this analysis since the other couple of rows are produced when the transfer is performed after more than one revolution.
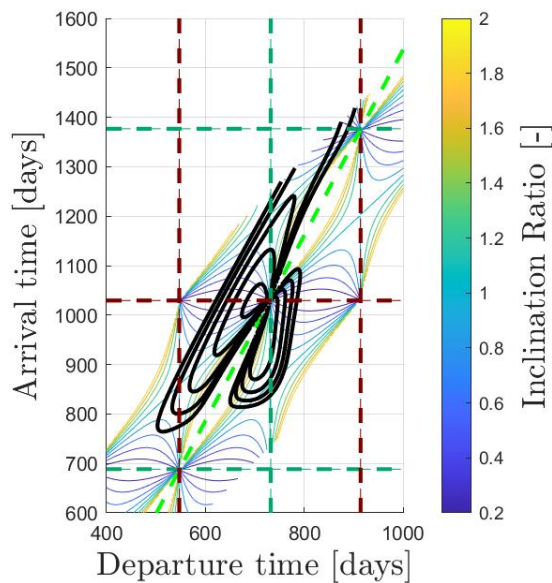

Figure 4.10: ψ plot with ΔV contours superimposed.

In Figure 4.10 the ΔV islands are superimposed (in black to avoid mixing the color sclaes) to the ψ plot to observe in detail the region of interest which is the one close to the 180 deg transfer. The plot shows the connection of rhomboids in rows parallel to the 180 deg transfer line. The empty rhomboids get partially filled by the new orbits considered but still leaving no solutions in correspondence of the ridge.

From Figure 4.9 and 4.10 one can observe that the vertical sides of the rhomboids (linked to $\psi = 1$) are aligned with the transit lines of Earth showing that, departing from the line of nodes, the transfer orbit is already inclined as the arrival one and the change of plane is totally performed at departure. Contrarily, the value of ψ in the regions around the horizontal lines (so in correspondence of arrival when Mars crosses the line of nodes) is close to zero, showing that the transfer orbit in this case lays on the ecliptic plane and the spacecraft performs all the change of plane when arriving at Mars.

Moreover, it is observable that some connection points are present. In Figure 4.9 the lines of solutions having $\psi = 1$ connect each other in the direction parallel to the ridge forming the rows already mentioned, while in the direction parallel to the other diagonal of the rhomboid (the horizontal direction) all the differently coloured line converge in the same points. These points represent the transfer orbits starting and finishing when the respective planet is in correspondence of the line of nodes, this can be deduced observing the intersection between the transit lines. In this cases, the initial and final point of the transfer orbit lay on the line of nodes and all the different inclined transfer orbits are possible.

The information needs to be completed with the eccentricity of the transfer orbit, at least for the most interesting situations. Inclination ratio is not enough and for this reason the e_{transf} porkchop plot is displayed in Figure 4.11. Here the contours are produced for $i_2 = 5\ deg$ and superimposed on the graph with a different colour to help the visualisation.

It is possible to notice that e_{transf} has a minimum value dictated by the size of the two orbits, as expected from Lambert's theory [8] [27]. This minimum value corresponds to the $e_{min} = e_H$ calculated as the eccentricity of the Hohmann transfer given two circular orbits.

$$\begin{cases} r_{p_H} = r_E \\ \\ r_{a_H} = r_M \\ \\ e_H = \dfrac{r_{a_H} - r_{p_H}}{r_{a_H} + r_{p_H}} = 0.2053 \end{cases} \tag{4.3}$$

where r_{p_H}, r_{a_H} represent the periapsis and apoapsis radius of the Hohmann's transfer orbit respectively.

The e_{transf} plot shows that the low ΔV contours get close as much as possible to the Hohmann transfer, both for short and long transfers, so in both sides of the 180 *deg* transfer line. A different scenario happens in the ψ plot where the long transfers solutions at the inner contours prefer low values of ψ. Contrarily, the short transfer is more efficient when the same values goes beyond 1, so aligning with the vertical transit lines. So, the most efficient long and short transfers are a similar trajectory in terms of eccentricity but their inclination is significantly different.

Finally, it is interesting to note that e_{transf} reveals appears low even in the region of the ridge. However, these solutions require to inject the spacecraft on a more inclined transfer orbit that results in a high value of ψ and ΔV. This prevents the manoeuvre to be feasible.
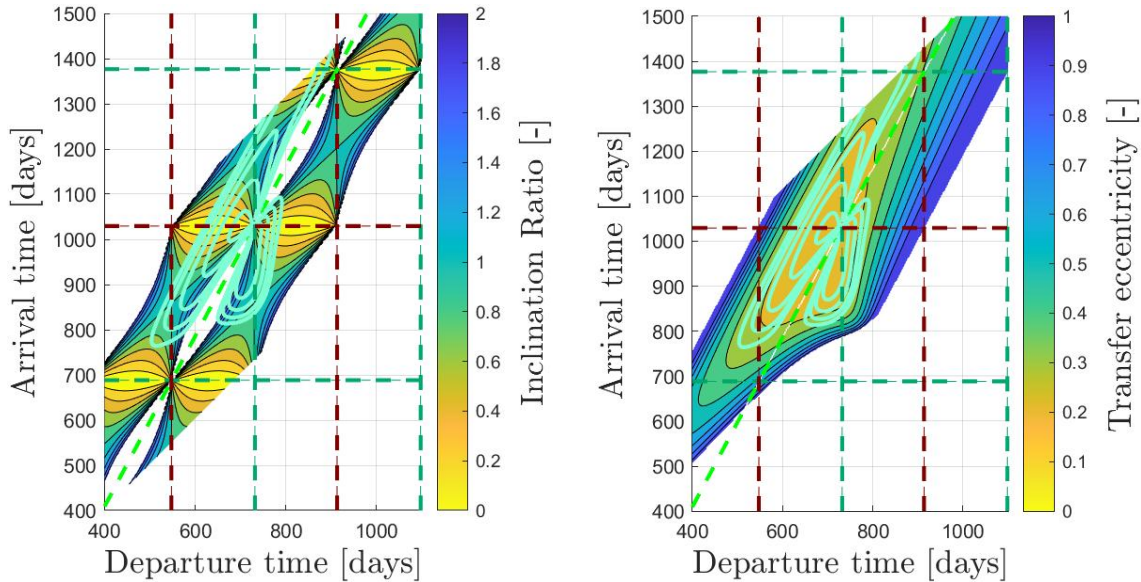
Figure 4.11: ψ plot (left) and e_{transf} plot (right) for $\Delta i = 5$ *deg*.

In any case, the regularity of minima location which underlines the trend of the solutions of emulating a Hohmann's transfer can be referred once again to the TOF.

Indeed, fixing the departure and arrival point on the line of nodes, the ΔV can be monitored imposing the TOF of the transfer. What emerges from this analysis is that, analysing the variation of the minimum ΔV with respect to the TOF, the minimum of the curve is obtained for half of the period of the Hohmann's transfer orbit defined as follows.

$$\begin{cases} r_{p_H} = r_E \\ r_{a_H} = r_M \\ a_H = \dfrac{r_{p_H} + r_{a_H}}{2} \\ TOF_H = \pi \sqrt{\dfrac{a_H^3}{\mu}} \end{cases} \tag{4.4}$$

This aspect stands for each value of the relative inclination. Although needing obviously a higher ΔV in terms of magnitude, the curve maintains the minimum in correspondence of the Hohmann's transfer. This result is displayed in the following figure summarising all the curves relative to different inclinations in a unique plot.
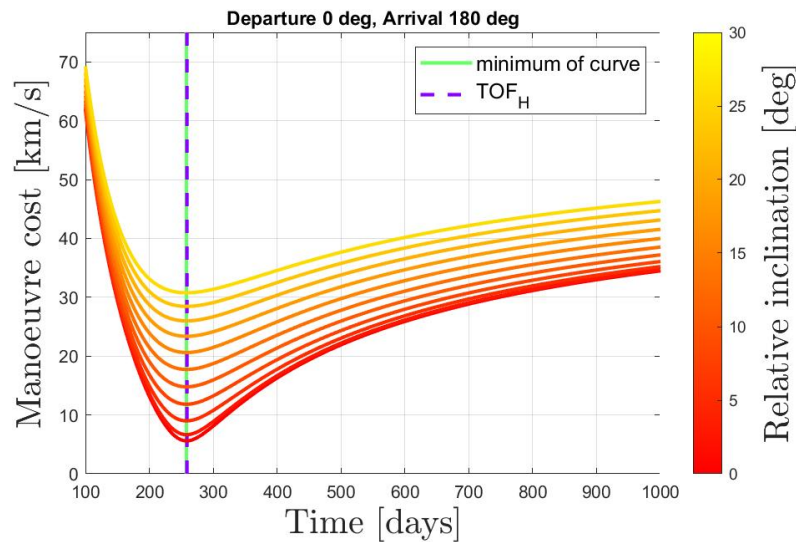
Figure 4.12: Trend of minimum ΔV as a function of TOF for fixed ϕ and different i.

This is not true anymore if the assumption to perform a transfer from node to node is removed. As expected, indeed, imposing i.e. $\phi = 160 \; deg$ the equivalent Hohmann's transfer does not change its value because the definition is still the same, but the minima of the curves align with a TOF which is different from Hohmann's semi-period. Given a particular configuration (fixing i), and choosing to depart when Earth is in proximity of the ascending node, the curves relative to many possible transfer angles (i.e. from 100 to 260 deg) can be plotted on the same graph. This is equivalent to monitor a specific transfer angle line on the porkchop plot, following each transverse line present in Figure 4.4.
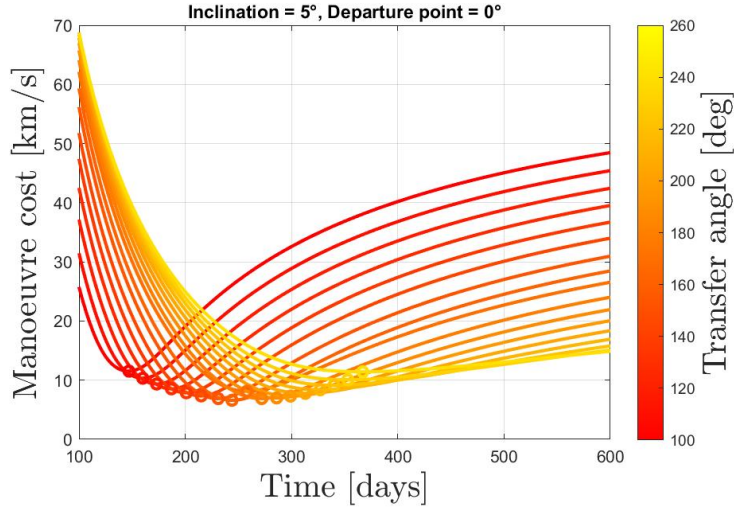
Figure 4.13: Trend of minimum ΔV as a function of TOF for fixed i and different ϕ.

The minimum, highlighted with a circle, varies in magnitude and translates towards the right when ϕ is increased, since higher ϕ transfers are less expensive if covered in higher TOF, while the curves flattens.

TOF and the ϕ are linked by the orbital dynamics of planets, so they cannot be varied at will to pursue the minimum of the curve. However, when considering a particular launch opportunity, a certain phasing exist between the two planets. For this phasing, for any curve of the graph (fixed ϕ) the laws of motion impose one specific TOF to cover that angular difference. Precisely, defining the time of a particular transit of Earth from the ascending node as $\overline{t_d}$, it is possible to recover from ephemerides the angular position of Mars $\theta_M(\overline{t_d})$. Therefore, for any $\theta_M(\overline{t_d})$ (which is the phasing, different at any successive launch opportunity) it is possible to calculate for any curve, so for any $\overline{\phi}$, the TOF needed to cover that angular distance. Being the orbit circular, the equation is simply:

$$TOF = t_a - \overline{t_d} = \sqrt{\frac{a_M{}^3}{\mu}}\left(\theta_a - \overline{\theta_d}\right) \tag{4.5}$$

where θ_a is retrieved once knowing the initial position $(\overline{\theta_d})$ and imposing ϕ.

This way, for any phasing, connecting all these successive matching points it is possible to evaluate the cost needed for the transfer as a function of TOF and ϕ enabling to plan the mission comparing the different possible transfer angle choices and their cost. In other words this is the case where the engineers can pursue the minimum transfer achievable. Figure 4.14 shows the locus of transfer solutions for a determined phasing.
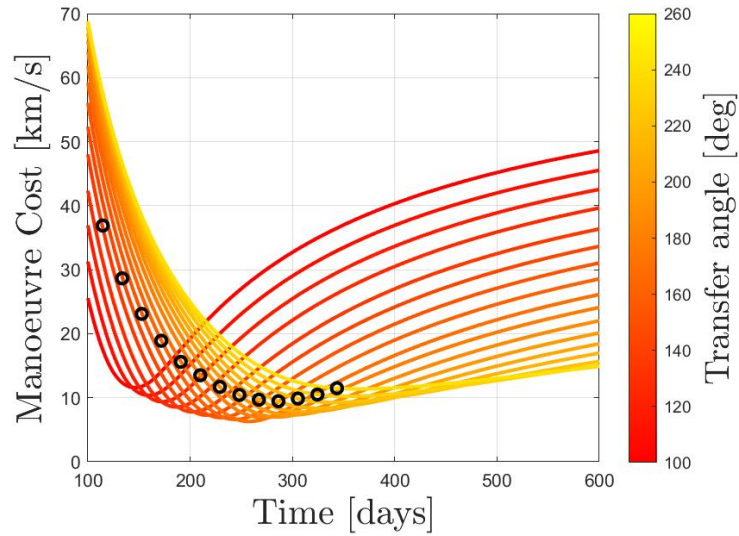
Figure 4.14: Possible transfer solutions for fixed i and phasing.

In Figure 4.15 instead the locus of transfer solutions for many different phasing conditions are superimposed on the same graph. This allows an immediate selection of the more useful ϕ curve based on the specific launch opportunity. The same reasoning performed up to now is valid also when the arrival is scheduled to be in correspondence of the node and the departure is variable. Both these results are visible in Figure 4.15.
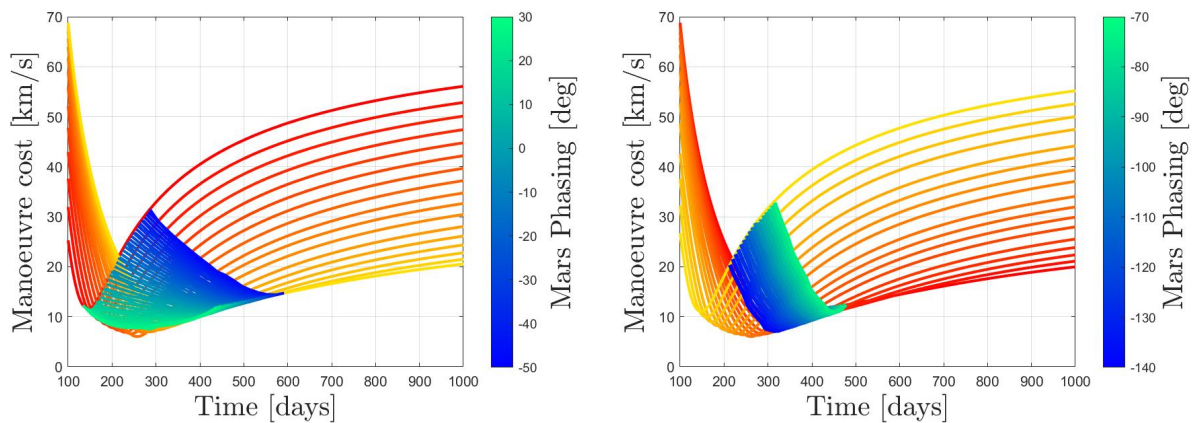
Figure 4.15: Possible transfer solutions for fixed i as a function of phasing when fixing the departure (left) or the arrival (left) on the line of nodes.

Once again, for the analysis to be complete it is crucial to better understand the effect of phasing.

4.1.1. Phasing

In this paragraph the effect of phasing is considered and its effect on the modification of
the porkchop plot is underlined. This consists once again in introducing an initial offset to
the true anomaly of one of the two planets at the initial time of the simulation. Reminding
that the orbits are circular, it is clear that the true anomaly is directly proportional with
time. For this reason, the variation of the initial phasing introduces a shift of the ΔV
contour lines along the Hohmann transfer line.

In order to visualise the effect of phasing, the inclination is fixed to a value different
from zero and the contour of a specific ΔV level (i.e. $\Delta V = 10\ km/s$) is plotted for
different values of the initial offset. However, unlike the case of Chapter 3, the increase of
inclination does not induce oscillations in the trend of the contours, but only a reduction
of the area. This is once again due to the circularity of the orbits and this also explains
why the trend of contours follows the Hohmann's transfer line: because for circular orbits
it always identifies the position of the contour.

The result is displayed in Figure 4.16 and shows the sliding of the contour along the
Hohmann line for phasings spanning from 0 to 360 deg and identified on the graph with
color that scales accordingly from red to yellow and from blue to light blue.

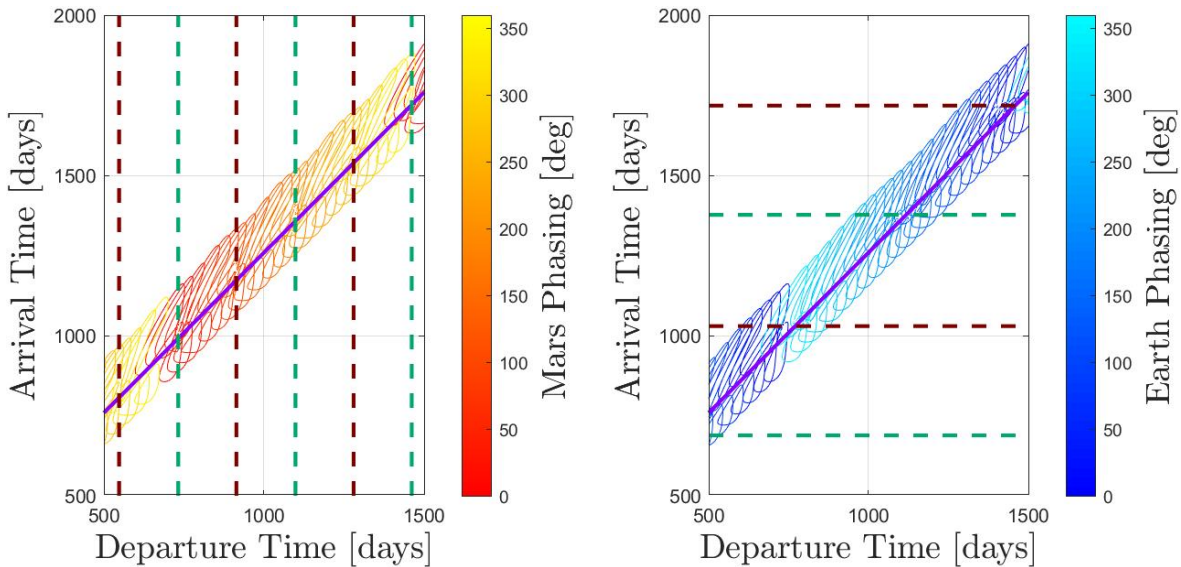Figure 4.16: Effect of phasing of Mars (left) and Earth (right) on the contour at $\Delta V =$
13 km/s.

The translation of the figure is towards the two opposite extremities of the Hohmann
lines in the two cases. The same effect was noticed in Chapter 3. For the sake of clarity,
in each of the two graphs are reported only the lines of transit of the planet whose

phasing is unaltered. Indeed, in the right plot for different values of the initial phasing the horizontal transit line would shift in a different date and the readability of the plot would be compromised.

For the purposes of this thesis the following analysis can be indifferently driven by one or the other. The choice of consider the phasing of Mars was arbitrarily performed.

The introduction of phasing alters as expected the locus of the 180 *deg* transfer line. Indeed, modifying the initial offset, is not surprising that the transfer having $\phi = 180\ deg$ occurs at a different date. However, in this chapter this characteristic line indicates the ridge position, so the shape of each single contour is strongly modified due to phasing because the 180 *deg* line always follows this regularity.

The modification of the shape of the single contours is attributable to the $\Delta i \neq 0$. Indeed, when the orbits are coplanar the shape of the contour is unaltered and the only effect is the sliding along the Hohmann line. When a relative inclination exists, the modification in shape of a specific contour (i.e. $\Delta V = 10\ km/s$) is a combination of Δi and phasing and can be very consistent. Three examples are reported in the figure hereafter for different values of phasing of Mars reported at the top of the respective graph.
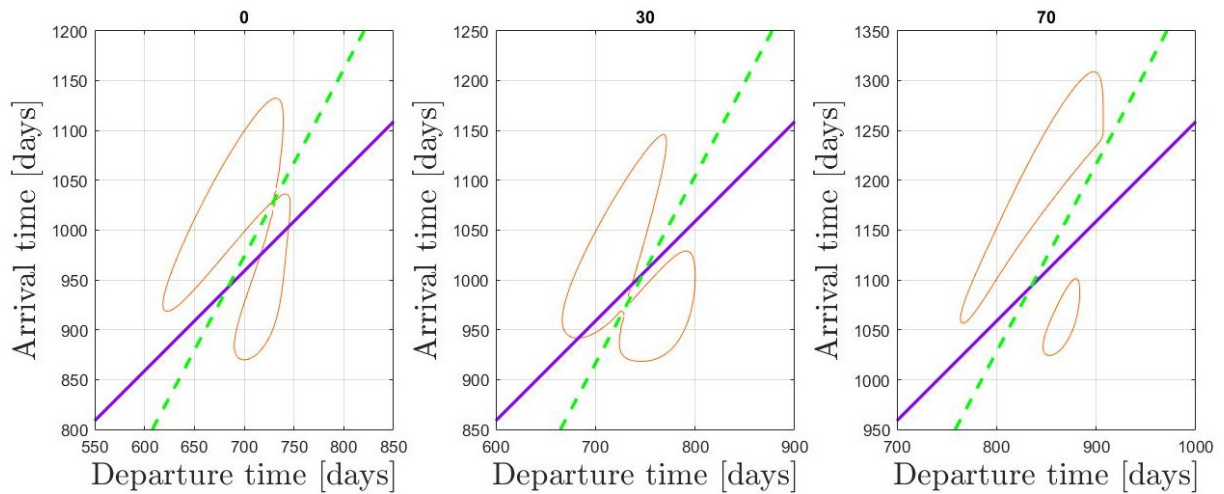
Figure 4.17: Contour $\Delta V = 10\ km/s$ for initial phasings equal to 0, 30 and 70 *deg*.

From the values of the ticks on the axes it is observable the sliding along the Hohmann line and towards its upper right end. However, what is immediately noticeable is the remarkable change of shape of the two lobes. Particularly, for a specific phasing, the bridge can be found above the Hohmann line (like in the case of offset of 0 *deg*) or below it (as happens for 30 *deg*). In some cases and for a certain interval of values the bridge even disappear: the two lobes are completely separated. At the application level this means that fixing a specific ΔV contour, for certain intervals of phasing, the com-

bination of dates identifying the bridge does not appear because they require a higher cost.

In summary, knowing the analytical position of the bridge is very important since it permits to identify the correct region in which the island is located. The precise qualitative feature of the bridge connecting the two lobes, instead, must take care of the phenomenon of the phantom bridge that depends on the specific ΔV contour level. A black asterisk is added when a certain bridge is not corresponding to a connection of the two lobes for the generic level $\Delta V = 10 \; km/s$.
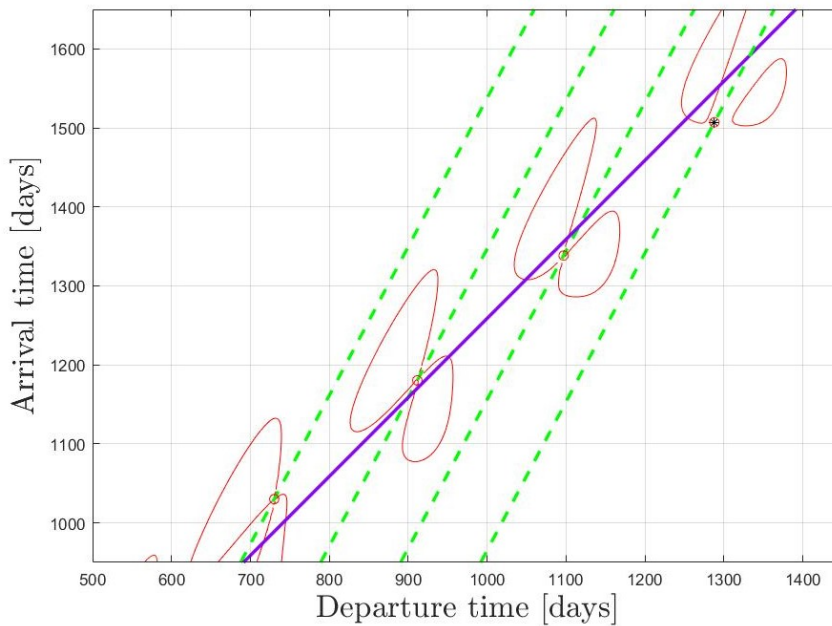
Figure 4.18: Localisation of real and phantom bridges.

Additional important regularities are found out when dealing with the location of the bridge for varying phasing. To this purpose, the choice of reporting on the same graph the position of multiple bridges (without the specific contour to avoid messing up the visualisation) in the interval $[0 - 360 \; deg]$ comes straight ahead. Particularly, considering the sliding along the Hohmann's line as a function of phasing, the position of the bridge is expected to follow this trend and move almost parallel to this line. Indeed when the orbits are coplanar, the bridge is actually not defined since there is no separation in the two lobes but the contours slides suggesting this trend. However, the variation of the locus of bridge is related to the transit lines when the Δi is increased. As a result, when considering Δi different from zero, the bridge dislocates from the Hohmann line occupying both the upper and the lower region. Figure 4.19 shows once again that they are attracted by the relevant dates in which the the planet transits from the line of nodes (the one whose

initial θ is kept fixed, so Earth in this case). The only exceptions in which the bridge is not found on a transit line occurs when the two lobes are not connected giving birth to the phenomenon of phantom bridge. In these cases the bridge is undefined and the solutions are marked in black.
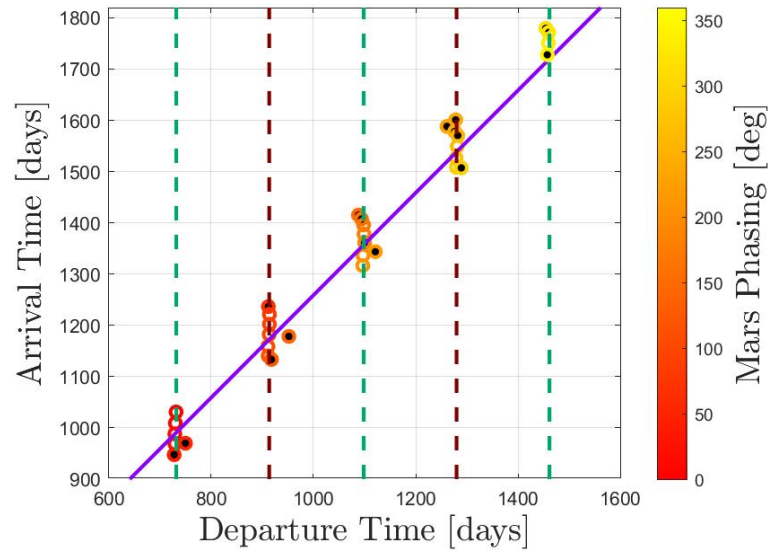
Figure 4.19: Location of bridges for different initial phasing when $\Delta i \neq 0$.

When inclination is increased, the areas of the contour tends to decrease, as a consequence the number of bridges highlighted with the black asterisk increases. So, the situations in which for $\Delta V = 10 \ km/s$ the bridge is a phantom bridge, increase in number with inclination and they are more frequent in the region most far away from the Hohmann line.
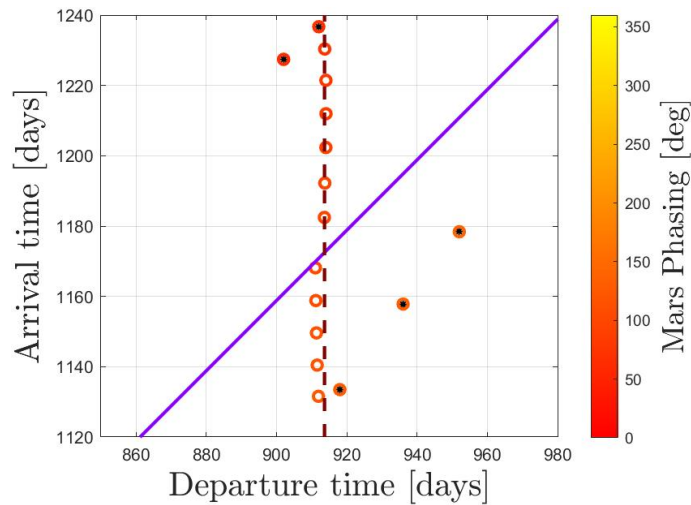

Figure 4.20: Location of bridges for different initial phasing when $\Delta i = 5 \ deg$, detailed view.

The enlarged picture presented in Figure 4.20 shows the detailed behaviour focusing the attention on the second vertical transit line for the case $\Delta i = 5\ deg$. The bridges align themselves in groups over subsequent transit lines, arranging from top to bottom, passing over the Hohmann line. The reason is easily explained since the analytical bridge is always found at the intersection between two transit lines; the situation is depicted as follows:

- Imposing a positive offset at the initial θ of Mars, the contour slides along the Hohmann line upwards;

- The date of transit of Earth from a specific node is fixed, so the vertical line too;

- The date of transit of Mars from a specific node is decreased in time since the positive offset at $t = t_0$ reduces the distance to be covered allowing an earlier encounter. As a consequence the horizontal line of transit is moved downwards.

When one transit line is populated, the position of the bridge jumps to the following transit line. The reason of these jumps is linked to the evolution of the shape of the inner contours. In Figure 4.21 this is illustrated observing the effect of Mars phasing which varies from 0 to 90 deg. In every sub-figure are reported the different contours enclosing the solutions at $\Delta V \leq 10\ km/s$ for inclinations belonging to the interval $[0 - 16\ deg]$ together with the respective minimum. The color of the contours scales from dark blue to light blue for increasing inclination, while the background reports the transfer angle ϕ fan. As expected, the external contour of the island (obtained for two coplanar orbits) moves but does not modify its shape with phasing. The opposite happens instead for all the other contour levels which not only reduce their size but also are subjected to a change of shape.

The effect of phasing is double. At higher level there is the upwards translation of the island along the Hohmann line while at lower level the bridge moves downwards inside the island itself. In Figure 4.21 a subcycle of the movements of the bridge is shown. The jump of the bridge can be explained. When the phasing is such that the bridge has reached the most bottom part of the main island, the island itself has started including the successive intersection between transit lines. As a consequence, the following bridge descends the main island and the minima position modifies getting close to the new point in which a 180 deg transfer is possible.
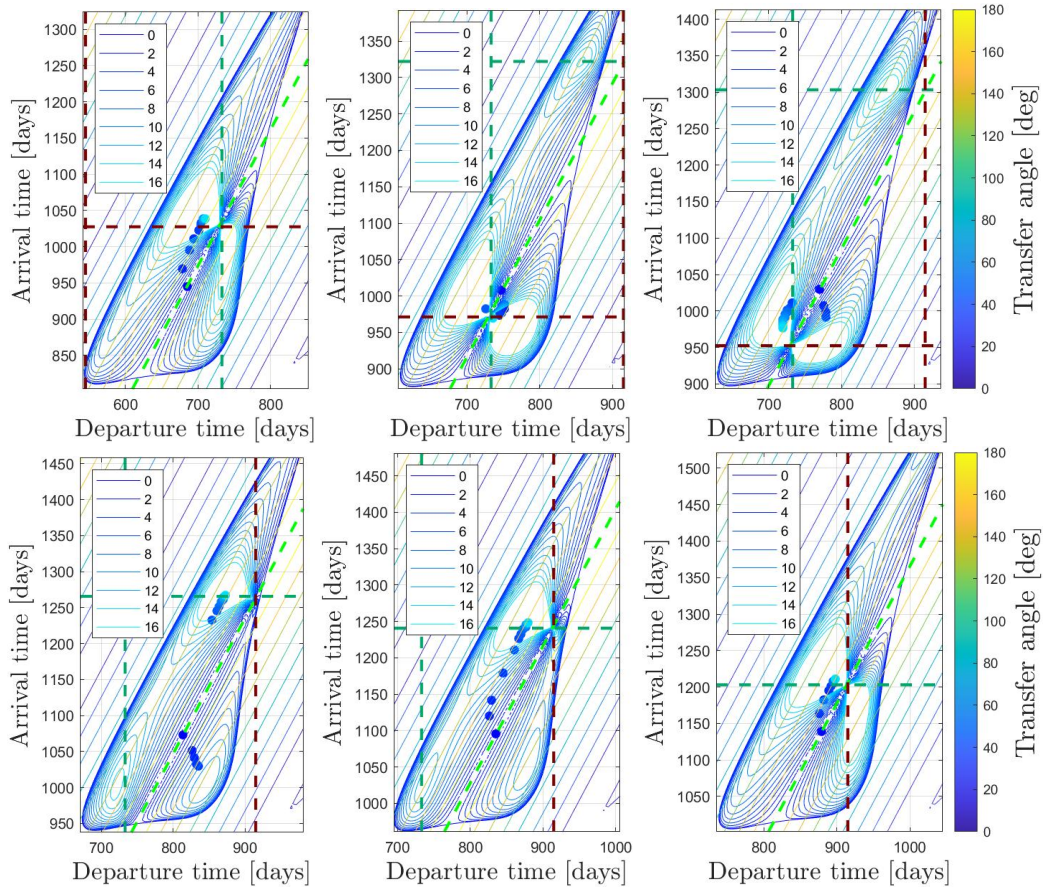
Figure 4.21: Variation of contours and minima location with phasing for different inclinations.

This explains what was announced describing Figure 4.6: the bridge is not always identified on the graph by the intersection point whose solution is the transfer from Earth at ascending node to Mars at the descending node, but also the other way round. The fact of falling in one of these two situations is caused by the specific phasing.

Moreover, observing the repetitiveness of the behaviour just described, a period can be defined to characterise these oscillations. To do so, for every initial phasing, the bridge position is calculated. Especially the distance on the *y axis* between each bridge and the Hohmann line is analysed. The procedure is equivalent to change the reference system with a new one defined as already done in the previous chapter with Equation 3.11 where y_{mean} is substituted by y_{bridge}. Therefore, the distances of the bridges from the Hohmann line are retrieved, highlighting the trend visible in Figure 4.22. The variation of phasing causes the internal modification of the contours and the evolution of the bridge from top to bottom is visible moving on the *x axis*. This recalls the trends suggested by Figure

4.19 and 4.20. After having reached the minimum, the y^* *distance* increases slightly its value before a sharp change in sign and magnitude occurs in the graph. This is the jump observed in the previous graphs which moves the bridge over the successive transit line.
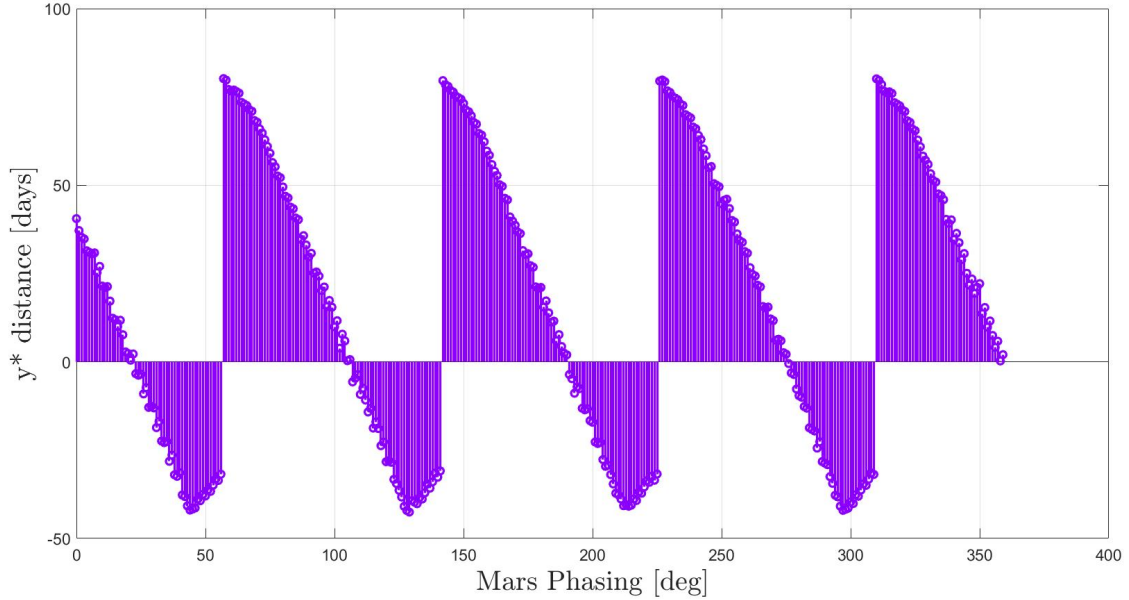
Figure 4.22: Distance between bridge and Hohmann line varying phasing of Mars.

A sub-cycle can be defined by the interval between two successive jumps as well as the interval between two successive intersection between the curve of bridges and the horizontal line $y = 0$ *days* which identifies the Hohmann line.

The period of these oscillations highlights phasing conditions when the resulting contours are similar. It has been evaluated to be:

$$T_{oscill} \simeq 84 \ deg \tag{4.6}$$

This is a period in terms of phasing, not in terms of time. Comparing now the top left and the two bottom right plots present in Figure 4.21 it is observable a similarity in the shape and position of the contours: this happens because the meaning of T_{oscill} is a repetitiveness and similarity of the launch conditions inside the interval $[0 - 360 \ deg]$. In other words the launch conditions are very similar in terms of porkchop plot whenever $\Delta\theta = k \ T_{oscill}$. Moreover, this period can be linked to the synodic period of the two planets. Indeed, in Figure 4.22 the range on $x \ axis$ is not covered by exactly four periods but something more and the extra is linked to the size of the orbits.

A clarification is needed: having an initial offset of 0 and 360 *deg* does not provide the same result because the focus is on the same island which slides along the Hohmann line. Clearly the starting configuration is the same, both planets at the beginning of time are aligned with the line of nodes and their θ is null. Indeed when the offset is 360 *deg* the porkchop plot is the same as the one for offset zero, but the contour monitored has reached the location belonging to the following launch opportunity. For this reason, the difference suggested by Figure 4.22 between the plot corresponding to 0 and 360 *deg* can be associated to the synodic period being not an integer number. In other words,the interval of variation is covered by a number of oscillations and something extra:

$$2\,\pi = 4\,T_{oscill} - \overline{x} \tag{4.7}$$

4.2. Role of the right ascension of the ascending node

Keeping fixed all the other parameters, the variation of the RAAN of an inclined orbit consists in changing the point in which the planet orbit crosses the orbital plane (the ecliptic in this case) of the other. In previous chapters, the simulations considered both Ω_1 and Ω_2 to be equal to zero, thus implying the line of nodes to lie on the $x\ axis$.
The following analysis accounts for all the possible values of Ω spanning a complete revolution of the line of nodes, so from 0 to 360 *deg*. Considering the Earth orbit as laying on the ecliptic plane, the only interesting parameter is Ω_2 because only Mars orbit is inclined.
The family of orbits obtained varying Ω_2 is portrayed in the Figure 4.23 in which the color of the martian orbit varies from orange to yellow for increasing value of the RAAN. All the family of orbits share the same relative inclination with respect to the fixed orbit of Earth.
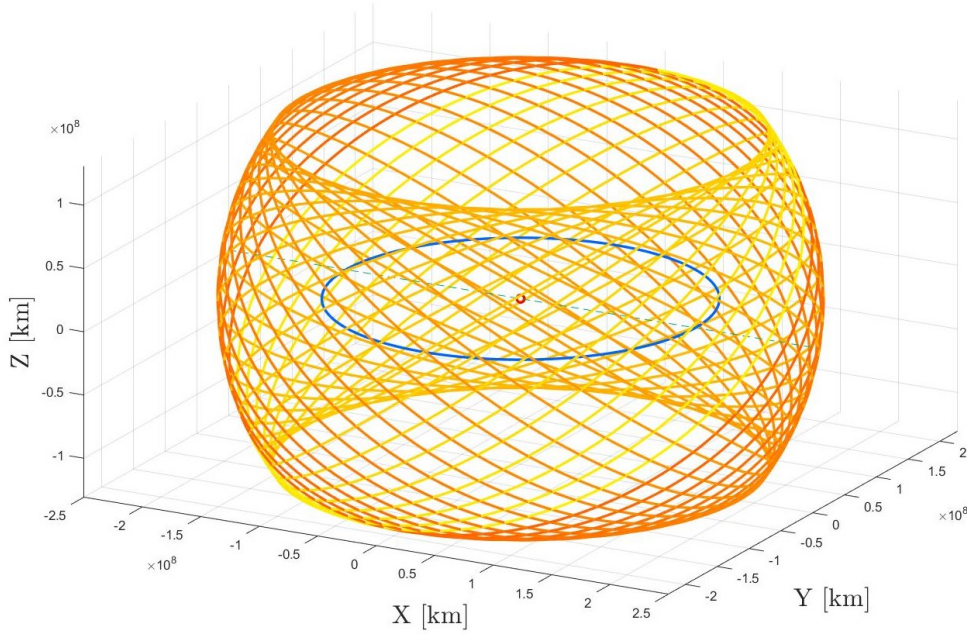
Figure 4.23: Family of orbits obtained varying the RAAN of martian orbit from 0 to 360 deg.

To evaluate properly the effect of a change in RAAN, all the other varying elements are fixed: the time window, the relative inclination and also the $\Delta\theta$. Reminding that $\Delta\theta$ is defined as $\Delta\theta = \theta_2(t = t_0) - \theta_1(t = t_0)$, and imposing that $\theta_2(t = t_0) = \theta_1(t = t_0) = 0$, this means that $\Delta\theta = 0$ and in this case both planets at t_0 are located at quota $Z = 0\ km$. However, Mars starting point will follow the rotation of the line of nodes (modifying its X and Y coordinates at t_0), while Earth will be still at its original location, the $x\ axis$, because its parameters were not varied.

Therefore, if in case of phasing the orbit was freezed and modifying the initial phasing influenced the planet position at t_0 in terms of X and Y, in this chapter the starting point quotas Z are imposed as null and the variation of initial position is given by the orientation of the orbit itself rotating the line of nodes.

For the configuration just described, the porkchop plot can be calculated. Even in this case, varying the value of Ω_2 the main effects are a translation of the islands together with a modification in shape. In order to analyse the effect of Ω_2 in the whole interval $[0 - 360\ deg]$, the specific contour $\Delta V = 10\ km/s$ is considered and its plot is visible in the left plot of Figure 4.24. Referring to this specific contour it is possible to notice qualitatively from the figure some intervals of RAAN in which the lobes are separated. Their behaviour is recurring, as well as the behaviour of the border of the envelop which

is dictated by Mars transit lines.

In order to better understand this, the effect of RAAN is compared to the previously described effect of phasing which is flanked in Figure 4.24. The behaviour is analogous. Indeed, the variation of Ω_2 is equivalent to the effect of varying Earth phasing (the planet whose parameters are unchanged). Considering a reference frame in which $x\ axis$ is stick with the rotating line of nodes, the scenario is equivalent to consider simply a negative phasing for Earth.
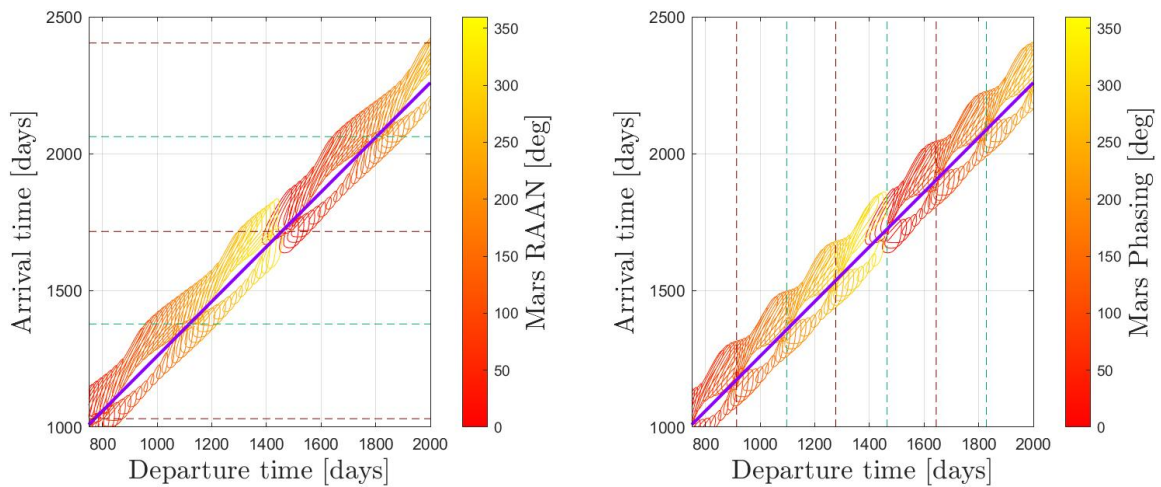
Figure 4.24: Envelop comparison of contours $\Delta V = 10\ km/s$ when varying RAAN (left) and phasing (right).

The oscillations of the border of the envelop reflect the regularities described earlier. The width of the envelop is function both of the characteristics of the orbit (the size of the contour decreases when inclination increases) and of the settings of the analysis (lower ΔV levels produce smaller islands). Particularly, the envelops are enlarged the more the relative inclination is close to zero and the higher is the ΔV considered to generate the envelop. The borders, instead, have an oscillating trend influenced by the relevant transit lines. In the left figure the frequency is dictated by the transit of Mars from the line of nodes, while the opposite happens in the right figure in conformity to what has emerged in the section related to phasing.In confirmation of this, the bridge location can be plotted as well as a function of the RAAN. The result is portrayed in the following figure and once again verified what has been just reported: the bridge location is attracted by the horizontal lines.

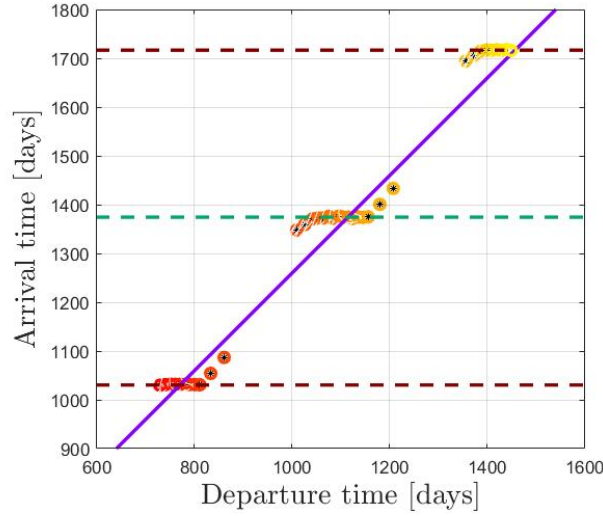Figure 4.25: Location of bridges for different values of Ω_2 when $\Delta i = 5\ deg$.

Similarly to Chapter 3, it is possible to decouple the effect of RAAN and phasing removing the hypothesis that $\theta_2(t_{dep})$ follows the rotation of the line of nodes. It is possible indeed to vary the orientation of the orbit rotating the line of nodes but keeping fixed the X and Y coordinates of Mars at the beginning of time. This way Mars, Earth and the Sun start their motion always aligned in the (X, Y) plane and consequently the quota $Z_2(t_{dep})$ varies with Ω_2. This allows to study the effect of the orbit orientation decoupled from phasing. The analysis is performed simply imposing that for any $\Omega_2 = \overline{\Omega}$ the initial true anomaly is $\theta_2(t_{dep}) = -\overline{\Omega}$. The contours obtained from different inclinations are completely enclosed by the one obtained for coplanar orbits and null phasing (planets aligned at t_0), so they are bounded in a precise region of the epoch space. The variation of Ω varies the shape of the contours, but does not produce the sliding along the Hohmann line. Furthermore, the 180 $line$ is fixed because its translation is affected only by the initial angular distance between planets. For this reason, since this line is constrained to divide the island in the two lobes, the effect obtained is a slight translation in the direction parallel to the ridge. This variation can be observed in Figure 4.26.
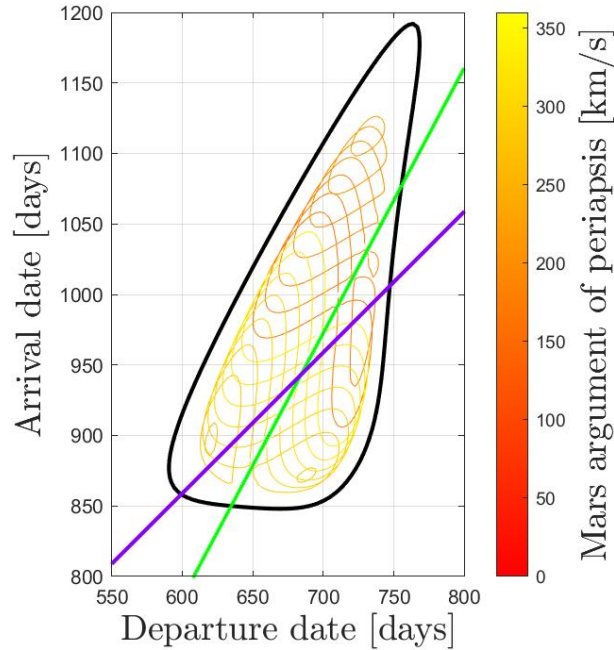
Figure 4.26: Variation of the ΔV contour caused by the orbit orientation (Ω) decoupled from phasing.

4.3. Grid reduction

The computational power required by the algorithms grows as much as the analysis gets detailed. Therefore, a grid reduction can be fundamental, especially when combined with the pruning technique as described in [22]. This means that the analysis can become smarter applying the algorithms in a wise way. Instead of considering the whole vectors of departure and arrival dates, a grid reduction would limit the number of significant points without losing meaningful solutions.

Depending on the contour level to be considered, the borders of the envelop can be reconstructed retrospectively to limit the analysis in a specific region of the plane. This can be done both for the envelope obtained varying phasing and for the one obtained for varying RAAN. To do so, the reference system is rotated with respect to the Hohmann line to monitor the oscillations as expressed by Equation (3.11) where $y_{envelop}$ substitutes y_{mean}. $y_{envelop}$ is referred to the envelops like the ones present in Figure 4.24. Basically, knowing the expression of these curves (or a valid approximation), for every departure date, the arrival date would be searched only among the dates enclosed between the value of the upper and lower bounding curves. Thus, for any phasing (or RAAN), the expensive algorithm would search for interesting solutions only inside the belt enclosing the Hohmann line and limited by the bounding curves because it is known that in this belt there are

the solutions. This allows reducing the cost of the algorithm since the expensive Lambert solver would not be run for 360 planes of dates but just for 360 belts.

This might seem not worthy because, in order to limit the region of plane considered, the algorithm must be have been run to find the limiting curves. However, the first run needed to find the limiting curves can be done with a more loose time vector grid, since what matters is to eliminate all the dates which are certainly far from the region of the belt. Afterwards, detailed analysis can be done inside the belt itself. The grid discretisation can be modified: a time window which is more dense of dates can be produced only between the two boundaries to improve the quality of the analysis and get more precise contours.

Moreover, applying to real cases, so keeping fixed the orbital dynamics, precisely the semi-major axes, the relative inclination and the RAAN, the bounding curves are not variable. Thus, having built the belt once, the contour will only slide in a different place along the belt (due to phasing), but the limited region of the plane to be considered will not change.

In Figure 4.27 the upper and lower bounding curves are represented for different inclinations. As already known i_2 shrinks the contours. The mean of these oscillating bounding curves consequently gets closer to zero. Additionally, the limiting curves maintains the frequency of oscillations (related to transit lines) but modifies its amplitude as the inclination increases. For this reason, the grid reduction gets easier realising that, for each inclination, the envelop is bounded inside the one obtained in the circular case. This last one is almost a straight line and defines the belt simply quantifying the y^* distance of the upper and lower bounds.
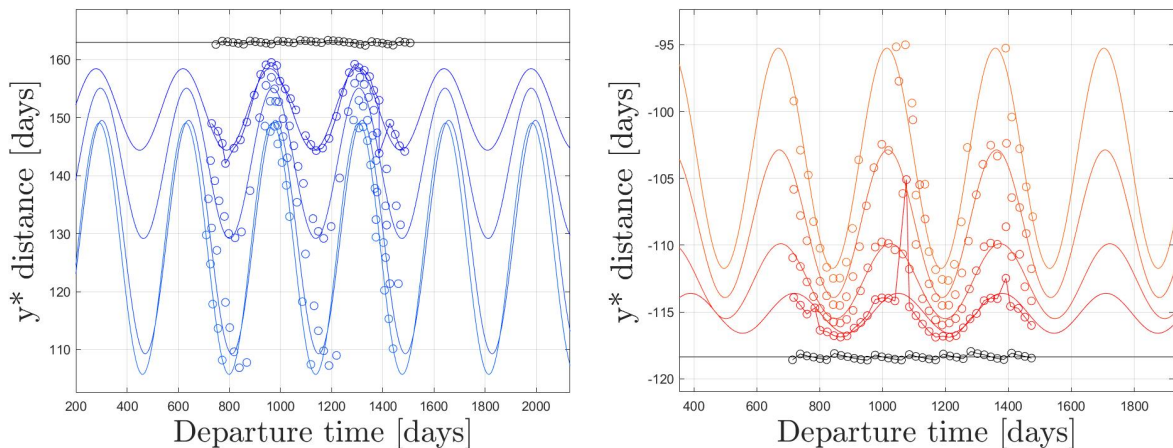

Figure 4.27: Upper (left) and lower (right) envelop bounding curves.

The belt related to the circular case can be used for any i_2 and it is simply defined by

the two offset y_{UP}^* and y_{LOW}^*. The analysis can be extended to different contour levels, modifying the width of the belt. Moreover, an analysis on the semi-major axis can be useful to apply this reasoning to other system configuration. Since the area of the ΔV islands varies with the difference $(a_2 - a_1)$, the belt width is also function of the parameter A_m which acts as a multiplier for the outer planet semi-major axis. This way the values of y_{UP}^* and y_{LOW}^* can be calculated and tabulated as a function of ΔV and A_m in order to know in advance the width of the belt where the contour is going to be found.

A further reduction considers the detailed analysis not in the whole belt but just inside a four-sided quadrilateral. It is already known that the contours slide along the Hohmann line for varying phasing and that the ridge is identified in any case by the 180 *deg* transfer line. For this reason, as it is shown in Figure 4.28, it is possible define two corridors. The first one is built considering two straight lines parallel to the Hohmann line and tangent to the most far point of the contour in both the two directions. The same procedure is done for the 180 *deg* transfer line. In this way the contour is always enclosed by the quadrilateral defined by the intersection between these 4 straight lines.

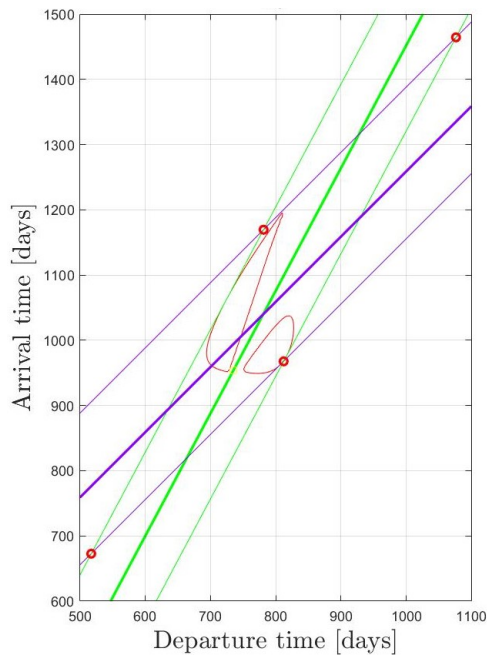Figure 4.28: Quadrilateral region limitation.

This method is similar to the previous one which used the belts. It needs a previous run of the algorithm (with a loose grid timespan) to save the vertex of the quadrilateral for any phasing, but it permits to delimit the detailed analysis in an even smaller region. The idea was to divide the belt in successive quadrilaterals which translate in the same way

of the contours. Even in this case the vertex of the quadrilateral can be tabulated as a function of A_m and the ΔV level so that the grid reduction can be applied time by time according to the necessities.

As reported at the end of Chapter 3, also the scenarios and results described in this chapter are reproducible considering transfers between different planets. Some regularities would be modified considering that the location of the ΔV islands and the position of features such as the bridge would be identified by different transit lines. Once the dynamics has been scaled considering the new semi-major axis of the two orbits, the analysis would be totally analogous to the one which has been presented.

5 | Transfer among eccentric and inclined orbits

This chapter aims to consider all the previously described parameters, trying to approximate as much as possible a real case scenario.

The RF is once again the one described at the beginning of Chapter 3. For this reason, the inclinations considered case by case are referred always to the Ecliptic plane. However, differently from Chapter 4, in this chapter the eccentricities of the two orbits are not zero. Many parameters play a role in adding a further complexity and generating a peculiar behavior in the morphology of the ΔV islands, so it is important to consider them gradually because adding multiple effects in the same plot would be very chaotic.

Firstly the combined effect of the two parameters, e and i, are addressed. Consequently, two Groups of situations are defined as follows.

- GROUP I: Effect of inclination variation on an eccentric orbit;

- GROUP II: Effect of eccentricity variation on an inclined orbit.

For both these two groups a further classification is introduced in order to address which of the eccentricities of the two orbits is considered. Indeed, the orbital configuration and the distance between the two planets is significantly different when the eccentricity considered is the former or the latter.

- Subgroup IA: Effect of inclination variation on Mars eccentric orbit;

- Subgroup IB: Effect of inclination variation on Earth eccentric orbit;

- Subgroup IIA: Effect of Mars eccentricity variation on an inclined orbit.

- Subgroup IIB: Effect of Earth eccentricity variation on an inclined orbit.

Differently from the previous classification, another subdivision based on the specific planet whose inclination is varied is not needed. Indeed, the first result is that, in both these groups of scenarios, the symmetry of the porkchop plots with respect to inclination is

still verified in the same way of Chapter 4. This induces no need of a further classification based on the specific planet whose inclination is modified because the parameter which matters is just the relative inclination Δi between the two orbital planes. GROUP I and GROUP II scenarios are represented in Figure 5.1 and 5.2 respectively. In Figure 5.1 the color scales together with inclination, and two different color scales are used to distinguish visually Subgroup IA and IB. Analogously, in Figure 5.2 the color varies with eccentricity.
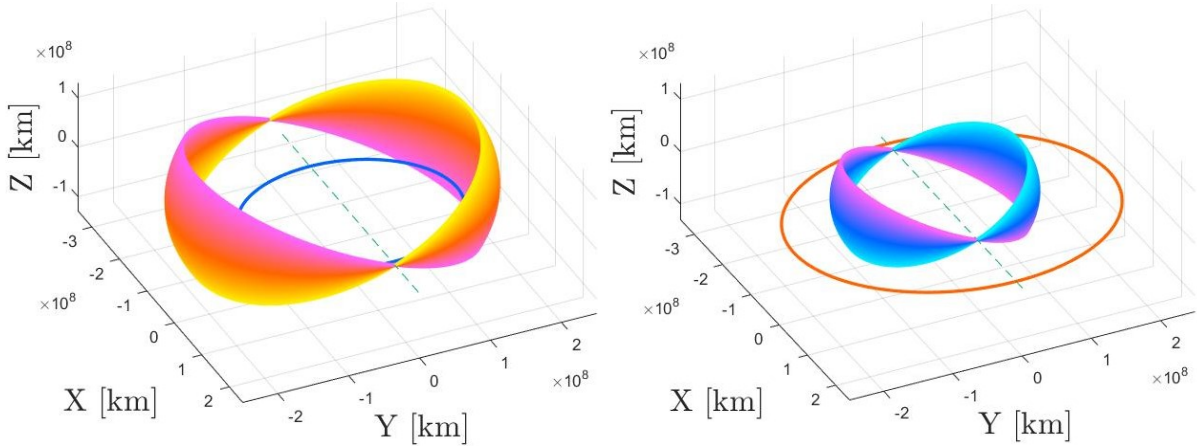

Figure 5.1: GROUP I scenarios. Subgroup IA (left) and Subgroup IB (right).
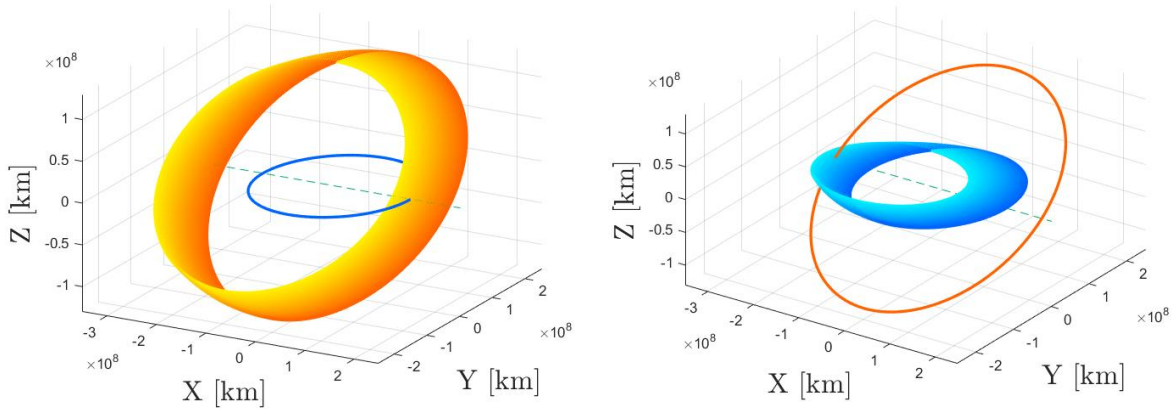
Figure 5.2: GROUP II scenarios. Subgroup IIA (left) and Subgroup IIB (right).

Concerning GROUP I scenarios, many similarities were found with respect to what happened when only one of the two parameters played a role. In the case of Subgroup IA, a fixed generic value $e_2 = \bar{e}$ was imposed, while e_1 is kept null. The porkchop plot produced now for increasing Δi show once again that the effects of the inclination on the ΔV islands are mainly the separation of the lobes with consequent generation of the ridge and the decrease of the area. The difference with the case described in Chapter 4 is that the fixed

eccentricity $\bar{e}$ spoils the shape of the island with respect to the circular-to-circular case. The case described by Subgroup IB scenario is totally analogous.

Concerning now the scenarios belonging to GROUP II, a certain $\Delta i = \overline{\Delta i}$ is introduced between the two orbital planes, and one eccentricity at a time is increased while the other is kept null. The ΔV islands in the Subgroups IIA and IIB are not the same since there is not a symmetric configuration but the effects are very similar: the fixed relative inclination produces a ridge whose width is independent from eccentricity. However, enhancing the eccentricity results in a strong modification in shape of the external border of the ΔV island (as in Chapter 3). In the end, at this stage the two single effects of Chapters 3 and 4 are concatenated.

The direct visualisation of such results is possible even adding the effect of phasing. As already discussed, the variation of phasing produces a shifting of the ΔV island on the graph and the sequence of these islands generates an envelope characterised by a certain frequency and amplitude.

In scenarios belonging to GROUP I, four different envelops can be produced, since for each Subgroup the effect of adding an offset to Earth or Mars modifies the resulting envelope. In the next plot it is reported the effect of introducing an offset to the initial angular position of Mars in a Subgroup IA situation. The phasing maintains the trend shown previously in Chapter 3: a notable modification in the shape and consequently in the value of interested area. This effect produces different peaks and the inclination does not influence the number of oscillations, it acts simply lowering the curve. This implies a smaller time window in which a specific transfer is feasible keeping the constraint of a maximum manoeuvre cost ($\Delta V = 10 \ km/s$). The results are reported in Figure 5.3.
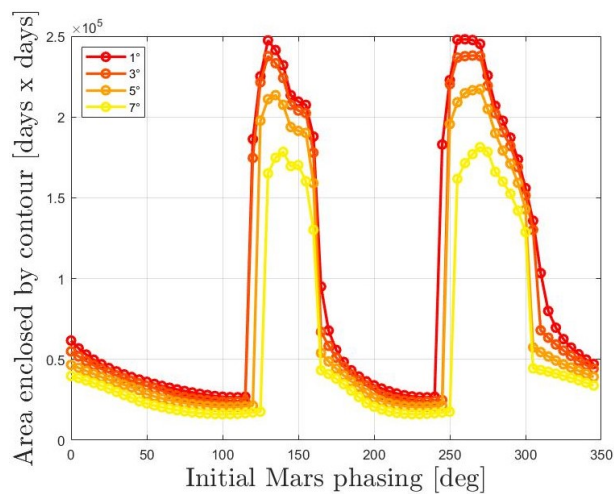

Figure 5.3: Combined effect of inclination and eccentricity on the area occupied by the contours in the porkchop plot.

The effect of eccentricity and inclination is qualitatively analogous when considering the other three scenarios belonging to GROUP I, therefore the trend has been reported just once to avoid redundancy. The envelop itself is shown in the left plot of Figure 5.4. From previous chapters it is already known that in case of circular orbits the envelop lies on the Hohmann transfer line, highlighted in violet. The enhanced eccentricity, instead, produces oscillations in the envelope modifying the size of the contours and concentrating the upper peaks in correspondence of the Earth transit lines. The superimposition of differently coloured contours shows the reduction in area of each contour caused by the higher relative inclination between orbits. The result is quite similar to the other three subgroups of situations. However, some differences are present with respect to what happens in the plot. First, considering the phasing of Mars, the upper peaks align with the dates in which the Earth transits from the ascending node in the case of Subgroup IA, while they align with the descending node transit in the cases of Subgroup IB. The reason is visible in Figure 5.1: the eccentricity of one orbit or the other causes a consistent reduction of the distance between the orbits in correspondence of the ascending node in the former case and in correspondence of descending node in the latter. Considering the Earth phasing, instead, the reasoning is the same but clearly reversed with respect to the transit of Mars from the nodes. In addition to this, another slight difference consists in the amplitudes of the envelops oscillations which are higher in the case of Subgroup IA with respect to Subgroup IB, independently from the planet whose initial offset is considered.

Scenarios classified in GROUP II, instead, are the ones reported in the right plot of Figure 5.4 where the different colours indicate the increased eccentricity influencing the location of the ΔV island. Even when a relative inclination between the two planets exist, the effect is to convey the islands in the region of the relevant transit lines.

In Chapter 3 the focus was on the transit of planets from the apse line, while in Chapter 4 the characteristic transit line was the line of nodes for obvious reasons: only one of them was defined at a time. In this chapter, having orbits both eccentric and inclined, these two lines are independent from each other being function of ω and RAAN respectively. At this stage both these two parameters are null and do not play a role: consequently the two lines are overlapping.
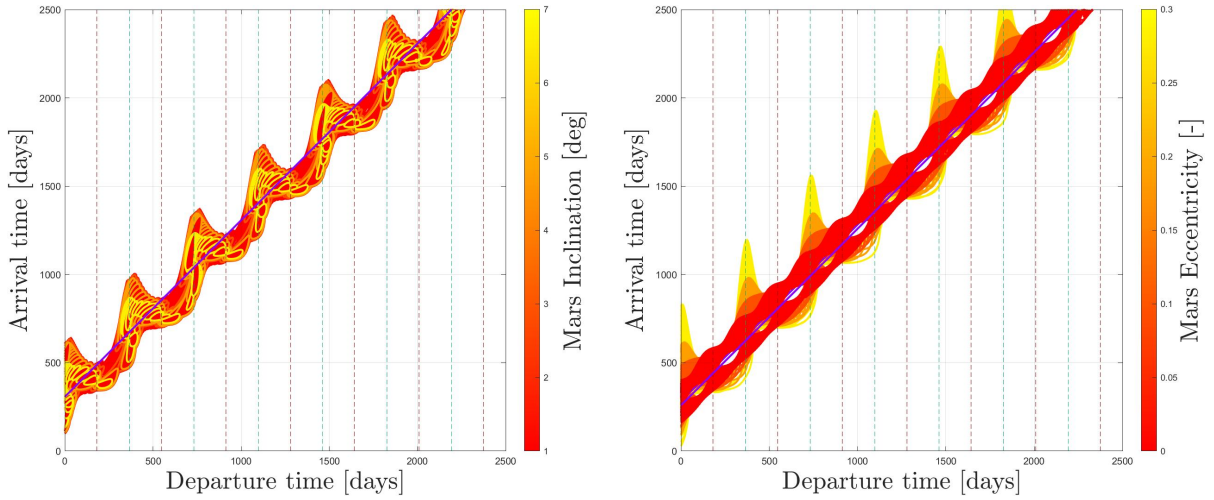
Figure 5.4: GROUP I (left) and GROUP II (right) envelops when considering the phasing of Mars.

5.1. 180 deg transfer line evolution

The combination of the different parameters produces effects which are not simply to track in a single graph.

However, it is possible to combine some results obtained in the previous chapters. The ridge, indeed, is still perfectly identified by the characteristic line highlighting the transfer having $\phi = 180 \, deg$.

In Chapter 4 the importance of the 180 deg transfer line has emerged. Indeed it passes through the island subdividing it in two lobes, permitting to locate the region in which the contour can be found in an easy way. Moreover, in Chapter 3 has been found out that the eccentricity spoils the shape of the contours due to the different time evolution of the θ in an eccentric orbit. For this reason, considering both eccentricity and inclination at the same time, it is possible to study the variation of the 180 deg transfer line under a huge variety of conditions in advance, especially when trying to generalise the effect of phasing, ω or RAAN. The 180 deg transfer line depends only on the orbital dynamics and approximates the island location variation since the bridge is always on this line. The analysis of the 180 deg transfer line is particularly suitable to explain great part of the results of this chapter.

First of all, the separate effect of e_1 and e_2 has been monitored and it is presented in Figure 5.5. The enhanced eccentricity strongly modifies the shape of the locus of solutions sharing $\phi = 180 \, deg$.
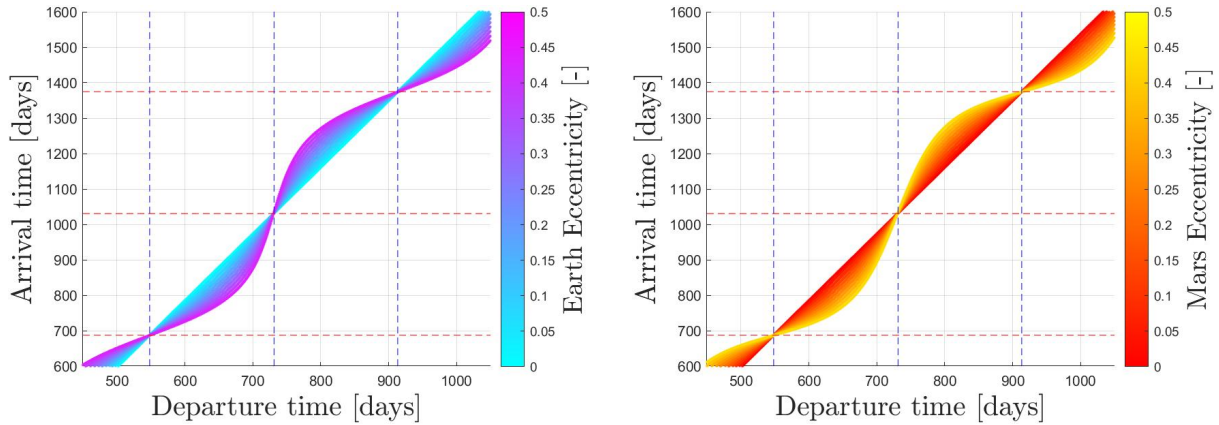
Figure 5.5: 180 *deg* transfer line variation due to Earth (left) and Mars (right) eccentricity.

The modification is proportional with the eccentricity and induces an oscillating trend with respect to the solution obtained in the circular case which is a straight line and will be indicated as $t_{180}\big|_{e=0}$. Considering this trend as a sort of wave, the "amplitude" increases with the eccentricity, while the "frequency" is constant being dictated by the synodic period and by the lines of transit from the apse line. Indeed, any curve generated for an eccentricity different from zero crosses $t_{180}\big|_{e=0}$ exactly at the intersection between the transit lines of inner and outer planet. Since these intersection points are fixed for any eccentricity different from zero, they are referred as *stationary points* in order to maintain the reference to the language of waves.

This same plot of curves is generated when the relative inclination is considered. In the same way as the 180 *deg* transfer line remained a straight line in Chapter 4, the inclination does not play a role in modifying such oscillations since the inclination does not appear in the equations of motion of a planet along the orbit (expressed by Equation (2.10) and (2.13)). The plots are not modified.

Considering both the eccentricities at the same time the family of curves is supposed to vary again. The distortion due to each single eccentric orbit must be considered and the result is that the amplitudes are summed.
In order to better understand this aspect, the reference frame is rotated to consider just the distortion with respect to the straight line belonging to the trivial circular case.

For any point of each curve is analysed the *Distortion distance*, defined as follows:

$$y_D\left(t_{dep}\right) = t_{180}\Bigg|_{e=\bar{e}}\left(t_{dep}\right) \quad - \quad t_{180}\Bigg|_{e=0}\left(t_{dep}\right) \tag{5.1}$$

where $\bar{e}$ is any eccentricity value imposed to one of the two orbits. This way it is possible to quantify how much a specific curve differs from the reference $t_{180}\Big|_{e=0}$.

Figure 5.6, shows the Distortion distance firstly for the case in which $e_1 = 0$ and e_2 is free to vary in the interval $[0, 0.5]$ (left plot). Then, the result is compared with the one obtained for e_2 spanning in the same interval, but imposing a certain $e_1 = \bar{e}$ not null (right plot).
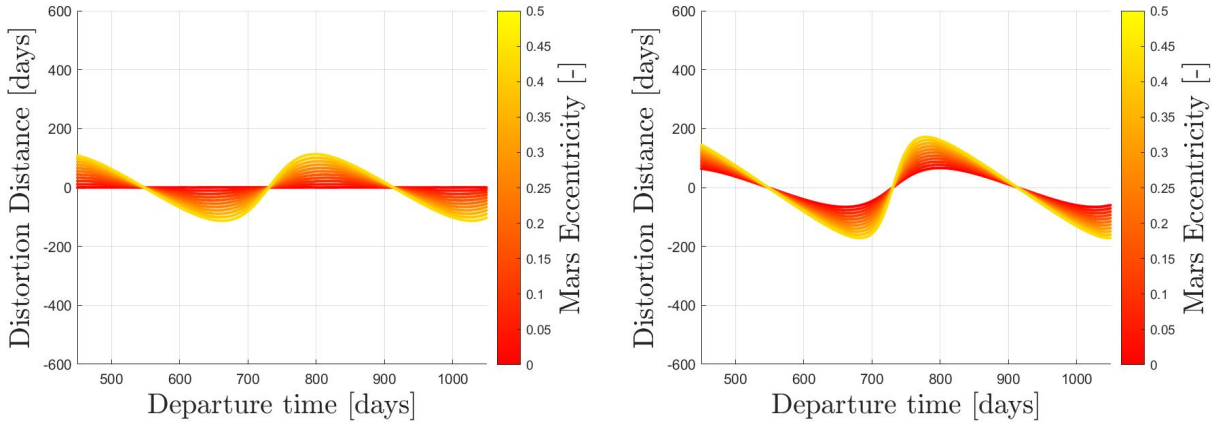

Figure 5.6: Distortion distance comparison. Difference in the family of curves for varying e_2 considering $e_1 = 0$ (left) and $e_1 = \bar{e}$ (right).

In both plots the colorbar is identical and is referred to e_2, and it is easy to observe the increment of the Distortion distance for each curve with the same colour. Moreover, also the curve having $e_2 = 0$ is no more a straight line. For this reason, when both eccentricities are varied, the definition of the Distortion distance must be updated considering that the reference case is the one in which both the eccentricities are null, because it is the only case in which the distortion is absent.

$$y_D\left(t_{dep}\right) = t_{180}\Bigg|_{e_1=\bar{e},\,e_2=\bar{e}}\left(t_{dep}\right) \quad - \quad t_{180}\Bigg|_{e_1=0,\,e_2=0}\left(t_{dep}\right) \tag{5.2}$$

The Distortion distance can quantify the variation with respect to the reference case. Particularly, monitoring its maximum or minimum value ($max(y_D)$ and $min(y_D)$ respectively)

the effect of any combination of e_1 and e_2 can be evaluated. Consequently, $max(y_D)$ is calculated and plotted as a 3D surface as a function of e_1 and e_2. The result is visible in Figure 5.7. Considering the minimum of this parameter is equivalent with the exception of the sign.
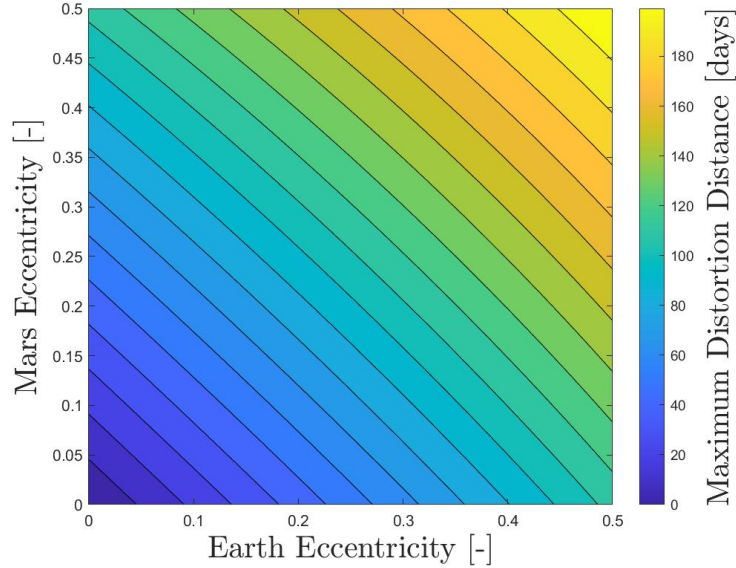

Figure 5.7: Maximum distortion distance as a function of any combination of e_1 and e_2.

In this case the effect is a total symmetry in the results. A sort of "commutative property" is verified: switching the values of e_1 and e_2 the maximum Distortion distance $max(y_D)$ is unchanged, thus resulting in a symmetry of the graph with respect to the line having $e_1 = e_2$.

At first glance, the locus of solutions having $\phi = 180\ deg$ and consequently the ridge location seems independent from the actual values of e_1 and e_2 but just function of their sum (e_1+e_2). Actually, this is not exactly verified, because the transverse regions in Figure 5.7 have borders not perfectly straight. However, in first approximation the distortion distance can be considered as function of the sum $(e_1 + e_2)$.

The symmetry just described does not imply a similarity in the final aspect of the ΔV island but just the identical position of the ridge. In other words, in this graph there is not a visible effect of the size of the orbit: the semi-major axis. The reason is that it just affects the period of each orbit, thus it affects the location of the stationary points but do not interfere with the amplitude of the oscillations.

5.1.1.   Effect of phasing

The effect of phasing has a strong influence in modifying the locus of the solutions. If the other parameters are fixed when a real transfer is considered, the phasing is the parameter which varies for different launch opportunities. In an infinite time, indeed, every condition of phasing can occur.

At this stage, the family of curves obtained varying e_2 (right image in Figure 5.5) is considered and an initial offset is imposed to the initial angular position of one planet at a time. The results are produced considering one planet eccentricity at a time; the choice of considering e_1 or e_2 is arbitrary. Considering both of them at the same time will produce the same superposition of amplitudes described earlier.

The following couple of graphs are produced just modifying the initial θ of the respective planet. The two family of curves share the same values of eccentricities (e_2 from 0 to 0.5, as before) but they have been plotted considering different phasing and can be distinguished by their different color. The standard one has been generated considering phasing zero and is represented with the colour scaling from red to yellow, while the other one is represented in a different colour scale to underline the different offset imposed to the initial θ, in this case equal to 90 deg.

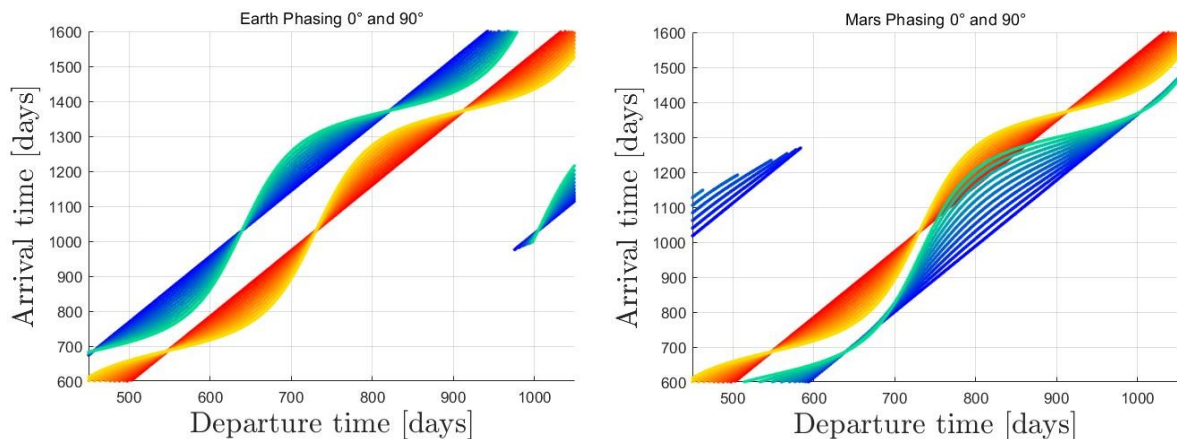Figure 5.8 shows that a substantial difference is present among the two cases.

Figure 5.8: Variation of the family of curves $\phi = 180\ deg$ caused by Earth (left) and Mars (right) phasing.

Phasing introduced to the planet laying on a circular orbit

When the phasing is introduced to the planet laying on a circular orbit (Earth) the effect is a simple translation of the family of curves towards the left side of the plot, so for

earlier departure times. This result is expected. Indeed, a positive phasing $\Delta\theta$ means that $\theta_0 = \Delta\theta > 0$ for the planet whose phasing is considered (Mars in this case). Consequently, the locus of solutions can be defined as follows:

$$t_{180}(t_{dep}) = t_{dep} + TOF \tag{5.3}$$

The TOF depends on the angular velocity of the planet (fixed) and on the angular distance to be covered (dependent on phasing) which is lower if the departure planet θ_0 is higher. In order to compare two different phasing conditions like the two present in the graph, 0 deg and 90 deg, the angular distance S_θ covered by the arrival planet is evaluated. Indeed, S_{θ_1} is 180 deg by definition, while S_{θ_2} can be computed as follows:

$$S_{\theta_2} = (\theta_E - \theta_M)\Big|_{t_{dep}} + 180 \ deg \tag{5.4}$$

$$TOF = \frac{S_{\theta_2}}{\sqrt{\frac{\mu}{a_2{}^3}}} \tag{5.5}$$

Being $\theta_E(t_{dep})\Big|_{\Delta\theta=90 \ deg}$ bigger than $\theta_E(t_{dep})\Big|_{\Delta\theta=0 \ deg}$ the result is that for any departure time the curve for 90 deg phasing is found at a higher arrival time than the one for 0 deg phasing.

For a similar reasoning, fixing the arrival time (and so Mars position at arrival), the constraint $\phi = 180 \ deg$ imposes the departure θ_E and the positive initial phasing permits to reach earlier that angular position, moving consequently the curve leftwards. Moreover, the curve is simply translated because the departure planet has a circular orbit, thus the TOF variation is proportional with phasing. The stationary points of the two envelops share the same arrival time since the time variation of Mars is still unchanged.

This is confirmed observing separately the modification due to phasing of Earth to the extreme curves of the envelop ($e_2 = 0$ and $e_2 = 5$) . Figure 5.9 shows in two adjacent graphs the effect of phasing of Earth when it is varied in the whole interval $[0 - 360] \ deg$.
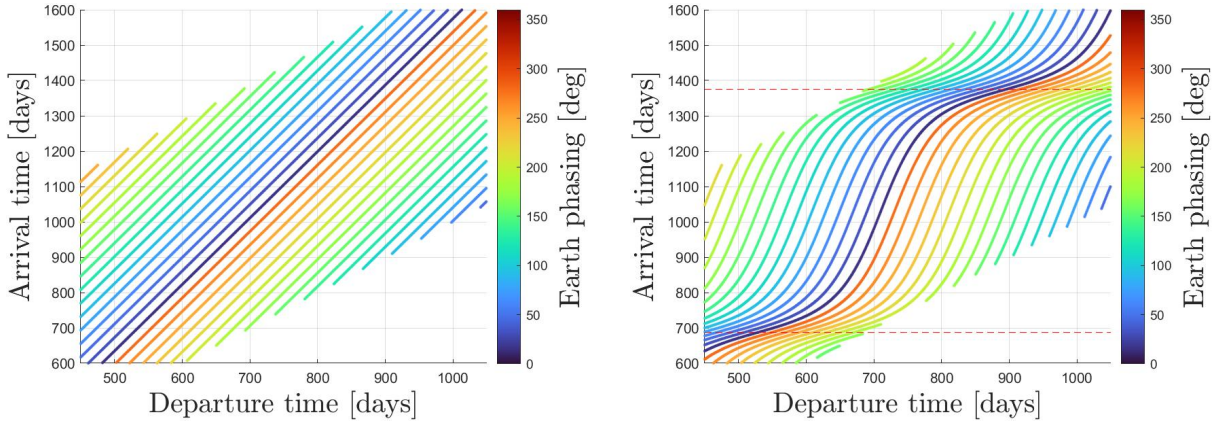
Figure 5.9: Variation of extreme curves $e = 0$ (left) and $e = 0.5$ (right) of the envelop due to different values of phasing of Earth.

Depending on the value of phasing in a specific launch opportunity, the translation gives an idea of the region of the epoch plane where the ridge is located and consequently of the appropriate evolution of the contour location. Moreover, if in the circular case there is nothing more than the straight line sliding leftwards, in the right plot it is possible to notice that the distortion due to eccentricity generates some denser regions in which all the lines are directed. These are related to the stationary points, found in correspondence of the horizontal lines highlighting the dates of transit of Mars from the apse line.

Phasing introduced to the planet laying on an eccentric orbit

The right plot of Figure 5.8, instead, shows the effect of the phasing of planet laying on the eccentric orbit. The translation of the family of curves is coupled with a modification in shape of the envelop itself. Comparing to the results of the previous paragraph (left plot in Figure 5.8), in this case the family of curves obtained for $\Delta\theta = 90 \; deg$ is located in the opposite side with respect to the family obtained for $\Delta\theta = 0 \; deg$. This time the envelop is modified since the TOF is found through Equation (2.13) and is no more directly proportional to the advance or delay caused by phasing. Actually, the shape of each curve is maintained, but a translation in the direction perpendicular to the curve $t180\Big|_{e=0}$ occurs modifying the overall shape of the envelop.

Therefore, the effect is a *double translation*. This consists in a main translation analogous to the aforementioned case (phasing Earth) in which the envelop is moved with respect to the envelop obtained for phasing zero. Added to this is a secondary one affecting separately each curve of the envelop and translating them perpendicularly with respect to

the standard curve $t180\Big|_{e=0}$.

The first effect has been already treated in the analogous case. The peculiar effect of Mars phasing is visualised in Figure 5.10 considering the Distortion distance.
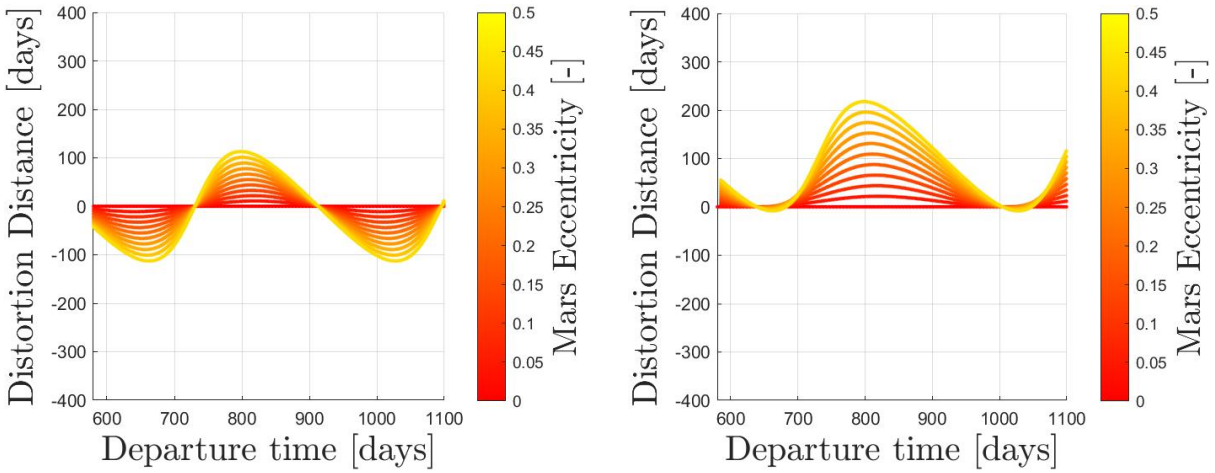

Figure 5.10: Modification of the Distortion distance envelop of curves for a Mars Phasing equal to 0 *deg* (left) and 90 *deg* (right).

In this reference frame the translation of the curves can be quantified considering the maximum and minimum values assumed by the Distortion distance. For any phasing, the Distortion distance is referred to the respective $t180\Big|_{e=0}$ line, which is affected by the main translation.

Figure 5.11 express how in this case the distortion is not just a function of eccentricity but also a function of phasing. The left plot shows the trend of maximum and minimum Distortion distance for a fixed eccentricity ($e_2 = 0.5$), while the right plot summarises in the same plot also the effect of eccentricity, giving the same colour to the maximum and minimum curves sharing the same eccentricity.
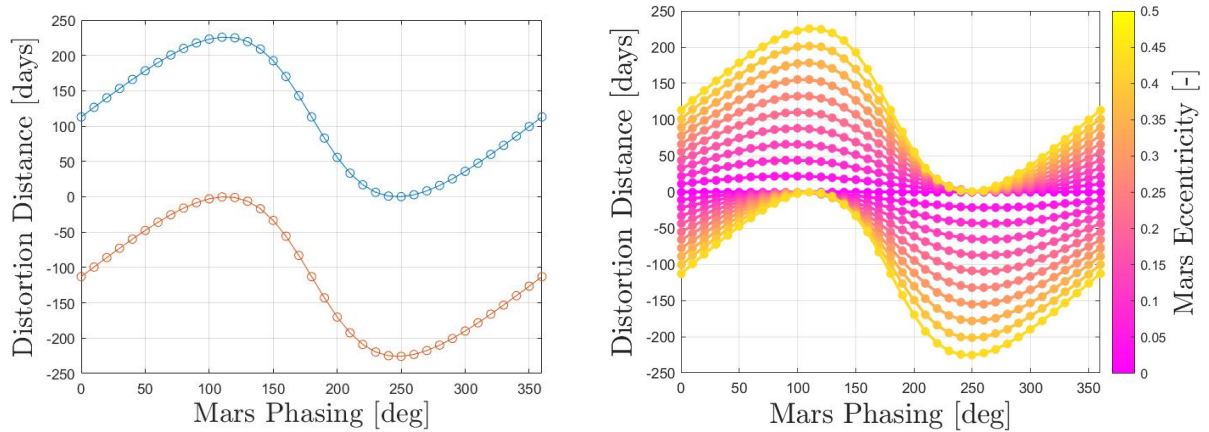
Figure 5.11: Maximum and minimum Distortion distance as function of phasing of the planet whose orbit is eccentric.

The distortion distance variation is proportional with the eccentricity but the effect of phasing is not trivial.

The distortion distance has 2 peaks which are common both for the trend of the maxima and for the trend of the minima. This shows that the effect is a translation (since affects equally the two limits) and not an asymmetric inflation of the curves. This translation moves the curves upwards for values of Mars phasing between 0 and 120 *deg*, then it changes direction in the interval between 120 and 240 *deg* and in the end it returns upwards between 240 and 360 *deg*. This is just a secondary effect since the main effect is the translation in the right-bottom part of the graph, which is the counterpart of what has been described for Earth phasing (observable in Figure 5.8). Figure 5.12 quantifies the importance of the secondary translation with respect to the main one: the two extreme curves of the envelop are plotted for varying values of phasing of Mars.
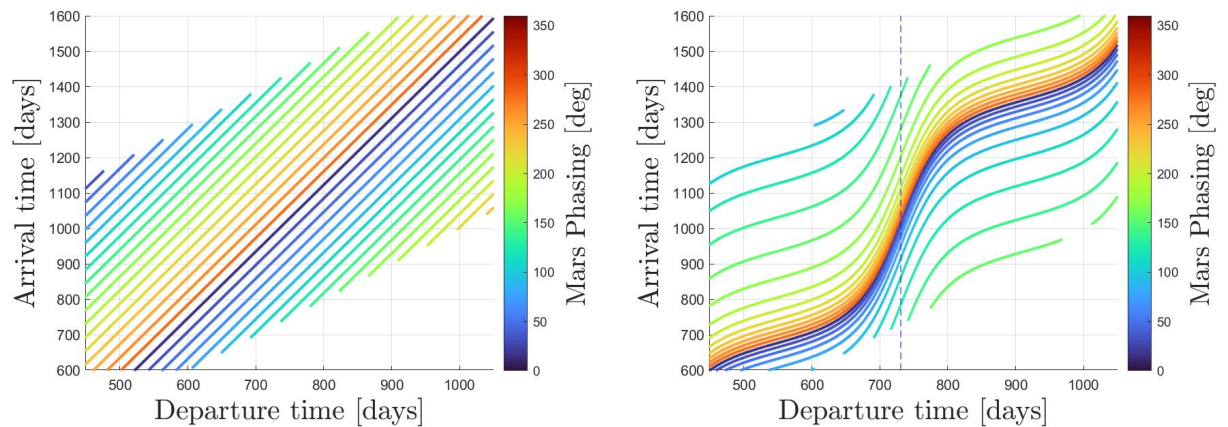

Figure 5.12: Variation of extreme curves $e = 0$ (left) and $e = 0.5$ (right) of the envelop due to different values of phasing of Mars.

This couple of plots shows similarities and differences with the previous case in which the phasing was imposed to the planet on the circular orbit.

First of all, the left figure is the matching case of the left plot in Figure 5.9 with the only difference that the planet which is considered in advance is Mars so the sliding is performed in the opposite direction. The right plot, instead, shows that the curve is subjected to the same main translation described in the adjacent plot, but also to the secondary translation which, up to a certain value of phasing, increases its magnitude. The overall effect causes, for a huge percentage of the interval of phasing variation, the overpopulation of the region of plane around the curve obtained for the reference case $\Delta\theta = 0 \ deg$. Therefore, the two different translations produce opposite effects that counterbalance each other for an important range of values.

This concludes the analysis of variation of the 180 deg transfer line due to phasing for a situation in which only Mars is moving on an eccentric orbit. The same identical dissertation would be produced when considering the phasing of Earth and Mars when the eccentric orbit is the terrestrial one. In that case it would be possible to observe a reversal of roles for Earth and Mars phasing. Indeed, the effect of Mars phasing (now on a circular orbit) would limit to a simple vertical translation of the family of curves. On the other hand, the effect of Earth phasing would consist in the double translation effects just described.

5.1.2. Effect of ω and Ω

As already discussed in the previous chapters, the effect of ω and Ω has two implications. In the first case $\theta_0 = 0$ for both planets, so the variation of the orbit orientation due to ω or Ω modifies the initial (X,Y) position of the planets and so their angular distance. In the second case the constraint is not on θ_0 but on the initial (X,Y) position, so that the planets at t_0 stay aligned even if one orbit is re-oriented. The hypothesis are presented in Table 5.1 in the case of ω_2, but the reasoning is totally reproducible for Ω_2.

	$\theta_1(0)$	$\theta_2(0)$	ω_1	ω_2	$X_1(0)$	$Y_1(0)$	$X_2(0)$	$Y_2(0)$
Situation 1	0	0	0	ω_2	x_{10}	y_{10}	$\overline{X_2}$	$\overline{Y_2}$
Situation 2	0	$-\omega_2$	0	ω_2	x_{10}	y_{10}	x_{20}	y_{20}

Table 5.1: Mars argument of periapsis variation comparison.

From previous chapters it is not surprising that the variation of ω_2 described by Situation

1 can be rewritten as a phasing variation related to the planet which is laying on a circular orbit. This is obtained rotating the reference frame together with ω_2 (or Ω_2).

	$\theta_1(0)$	$\theta_2(0)$	ω_1	ω_2	$X_1(0)$	$Y_1(0)$	$X_2(0)$	$Y_2(0)$
Situation 1	$-\omega_2$	0	0	ω_2	$\overline{X_1}$	$\overline{Y_1}$	x_{20}	y_{20}

Table 5.2: Equivalent Situation 1 formulation.

Therefore Situation 1 results in a simple translation, the one defined before as main translation, and is reported in left plot of Figure 5.13. The sliding occurs in the opposite semi-plane with respect to left plot of Figure 5.8 in correspondence of Earth phasing. This occurs since this time the phasing is constituted by a negative $\Delta\theta$, or in other words a delay.

Situation 2, instead, is a bit more complicated. The planets starts aligned at the beginning of the simulation, so the envelop does not experiences the main translation in one or the other direction with respect to the standard case, even if ω_2 is modified. However, the modified orientation of the orbit alters the shape of the envelops in the following way, visible in the right plot of Figure 5.13.
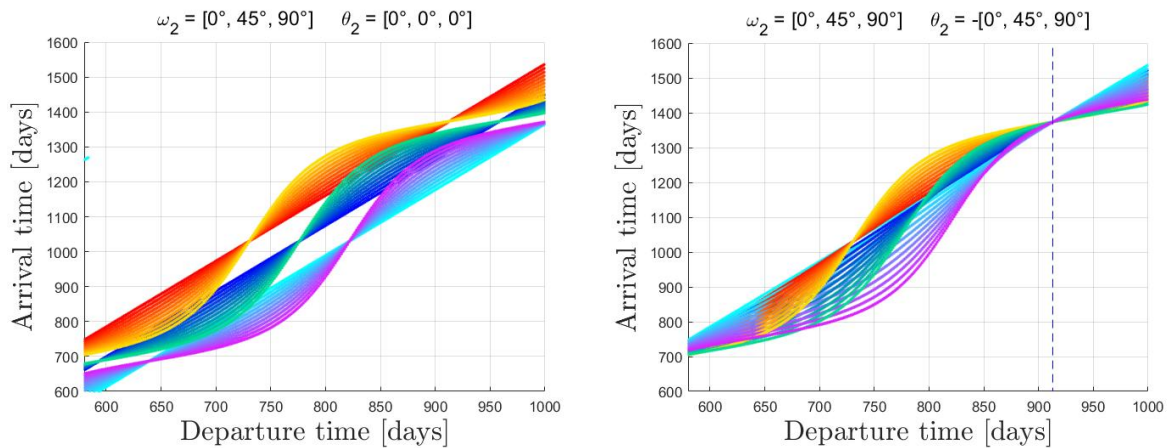

Figure 5.13: Situation 1 (left) and Situation 2 (right) envelop modifications.

The peculiarity of Situation 2 is that all the envelops are overlapping and share the straight line belonging to the circular case. So Figure 5.13 shows that the main translation described earlier is function only of the angular distance at t_0, which is null here. Moreover, the orientation of the orbit due to ω_2 reflects in the modification of the envelop. Once again this modification does not affect the shape of the curves but just their location,

thus modifying the aspect of the overall envelop. Even in this case the whole effect can be decomposed in two contributions. These are better visualised in the distortion distance plot where the limiting curve of the envelop ($e = 0.5$) is subjected to the variation of ω_2 in its complete interval of variation. It is possible to describe the two contributions as a parallel translation which increases continuously with ω_2 and a perpendicular translation which has cycles of 120 deg similarly to the previous case.
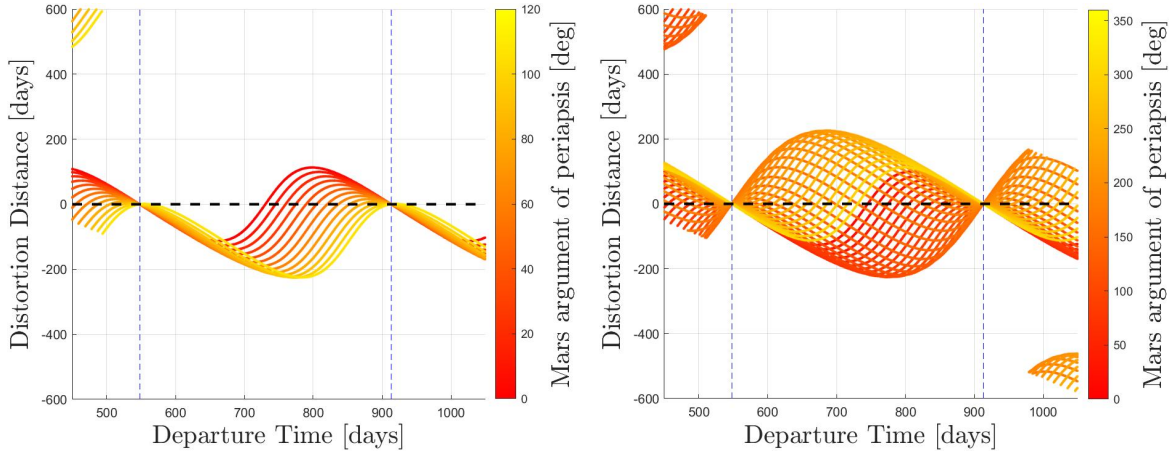
Figure 5.14: Effect of ω_2 on Situation 2 limiting curves.

In the left plot it is possible to observe the first cycle of variation. Contrarily to what occurred before, the perpendicular translation is downwards in this interval. In the following cycle, ω_2 spanning between 120 and 240 deg would move the curve to the top, still maintaining the parallel translation. Finally, in the last cycle ω_2 goes from 240 to 360 deg and the curve $e_2 = 0.5$ reproduces a configuration identical to the starting one. The complete evolution of the 180 deg transfer line is reported in the right plot, where the locus of solutions generates this candy-like envelop. Every curve merges with the other in the usual stationary points dictated by the vertical transit lines.

Summarising, the effect of ω_2 acts on the orientation of the orbit producing the variation in shape noticed. This effect should not be confused with the main translation which is caused only by the angular difference (both if due to ω_2 itself or due to phasing).

6 | Conclusion and future work

The aim of this thesis was to investigate the peculiar effect of eccentricity and inclination of the orbits in modifying the ΔV contour lines in the porkchop plot. This dissertation expands the results obtained by previous works (mainly Menzio [22] and Woolley and Whetsel [36]) focusing on the mechanism of formation of the ΔV contour lines in absence of the circular coplanar assumption. The main difference with the literature consists in the separate analysis of each parameter playing a role in the orbital dynamics. The target of the analysis was to shed a light on the variation of the resulting porkchop plots due to the evolution of the parameters. This way, it is possible to know in advance the shape of the contours and the location in the plane of the low ΔV transfer opportunities. The analysis has been performed considering an Earth-to-Mars transfer but can be extended to any couple of planets or moons scaling the results considering their specific data. This research allows a smart reconfiguration of the time windows, ignoring the pointless region of the graph far from the ΔV contours. This would optimise the mission design phase enabling a much lower computational effort.

Existing literature regarding the circular and coplanar scneario suggested the repetition of one ΔV island any synodic period. Moreover, each ΔV was located analytically by the intersection of two characteristic lines: the Hohmann transfer line and the 180 deg transfer line. Since for circular and coplanar orbits the position vector and the orbital velocity are constant in magnitude, any ΔV island had the same aspect.
The effect of eccentricity has been studied in Chapter 3. It alters consistently the shape of the ΔV islands, sometimes providing most convenient transfer opportunities. In correspondence of any different launch opportunity the planets would be aligned in a different position along the orbit, except when considering extremely huge time windows. This changes the position vectors and the planet velocities, thus modifying the inputs of the Lambert algorithm and the computed manoeuvre cost. The regularity in the location of the ΔV islands gets lost increasing the eccentricity. On the other hand, a new regularity has been exploited since the contours allocate on the epoch space mainly towards specific dates: the dates of transit at periapsis and apoapsis.

In Chapter 4 the effect of inclination has been considered. The change of plane is an expensive manoeuvre and the requested cost for a space transfer is influenced. Consequently, the ΔV islands decrease in size and are fragmented increasing the inclination. The ridge separating the islands in two lobes is always crossed by the 180 deg transfer line as described in literature. This time the island can be located analytically by the intersection of the 180 deg transfer line and two proper lines describing the dates of transit of the two planets from the line of nodes defined by their orbits. The intersection point occurs in correspondence of a feature named bridge which has been useful to analyse the variation of the island for different launch opportunities. Indeed, even if the orbits are circular, the shape of the ΔV island varies for any different launch opportunity.

The peculiar effect of ω and RAAN on the variation and evolution of porkchop plots has been analysed in Chapter 3 and 4 respectively. These parameters, alter the relative orientation of one orbit with respect to the other. Therefore, this introduces a further modification in the shape of each ΔV island. Their effect is linked to the modification due to the different phasing.

The analysis can be applied to real scenarios fixing the values of the orbital parameters, thus the phasing takes into account the time evolution. In an infinite amount of time any value of phasing will occur and analysing all the possible situations has been useful to define the region of plane where the ΔV island can be located. The resulting envelops showed the importance of the relevant transit lines which dictate the behaviour of solutions.

Chapter 5 considers both eccentricity and inclination at the same time. The concatenation of the singular effects has been shown. Moreover, the variation of the true anomaly evolution in eccentric orbits can be coupled with the peculiarity of inclined orbits to be always crossed by the 180 deg transfer line. This permitted to analyse, even over a variety of conditions together, the evolution of the region where the contour is likely to be found. The study of the solution sharing $\phi = 180\ deg$ permitted to quantify the distortion induced by the eccentricity, the translations of the islands due to phasing and the modification caused by different orbits orientation.

All these results are referred to direct planetary transfers from planet to planet. New insights on this topic could address multi revolution transfers. Particularly, the possibility to discover more convenient regions for higher TOF could be analysed in all the situations previously described.

An analysis on the semi-major axis variation has not been considered. Its main effects involve the periods of the orbits, which dictates the transit lines and the launch opportunities. So, varying the semi-major axis has the effect to enlarge or shrink the time window of the events but do not alters the discovered regularities. This is valid for small variation

of the semi-major axis difference. However, when moving away from the Earth-to-Mars transfer and considering missions to the outer planets, it is essential to consider flybys. This would complicate the treatise and could be examined in future works.

All the results obtained are valid in a different solar system or in a particular system of moons just by scaling the results with the own data. An interesting scenario involves three of the Galilean moons: Io, Europa and Ganymede. The analysis could be performed in this system considering the effects produced by the orbital resonance phenomenon which alters the gravitational interaction during the conjunctions. A specific analysis in this environment could be matter for future works.

Bibliography

[1] N. Arora and R. P. Russell. "A fast and robust multiple revolution Lambert algorithm using a cosine transformation". *Advances in the Astronautical Sciences*. Vol. 13, No. 150, pp. 411-430, 2014 . URL `https://citeseerx.ist.psu.edu/download?doi=10.1.1.711.9398&rep=rep1&type=pdf`.

[2] R. Bate, D. D. Mueller, and J. E. White. *Fundamentals of astrodynamics*. Dover Pubns, 1971.

[3] R. H. Battin. "An elegant Lambert algorithm". *Journal of Guidance, Control and Dynamics*. Vol. 7, No. 6, pp. 662–670, 1986, doi: 10.2514/3.19910.

[4] R. H. Battin. *An Introduction to the Mathematics and Methods of Astrodynamics, Revised Edition*. American Institute of Aeronautics and Astronautics, 1999.

[5] C. Blum, M. J. B. Aguilera, A. Roli, and M. Sampels. *Hybrid Metaheuristics*. Springer, 2008.

[6] M. Ceriotti. "Global optimisation of multiple gravity assist trajectories". PhD dissertation, University of Glasgow, 2010. Supervisor: Massimiliano Vasile . URL `https://theses.gla.ac.uk/2003/1/2010ceriottiphd.pdf`.

[7] A. Cianciolo, R. Powell, and M. Lockwood. "Mars Science Laboratory launch-arrival space study: a porkchop plot analysis". *2006 IEEE Aerospace Conference*, pp. 1-10, Big Sky, MT, USA, 4-11 Mar 2006,. doi: 10.1109/AERO.2006.1655797.

[8] H. D. Curtis. *Orbital Mechanics for Engineering Students*. Elsevier, 2014.

[9] D. de la Torre Sangrà and E. Fantino. "Review of Lambert's problem". *25th International Symposium on Space Flight Dynamics*. Munich, Germany, Oct. 19 - 23, 2015 . URL `https://issfd.org/2015/files/downloads/papers/028_Sangra.pdf`.

[10] P. Deuflhard. A short history of newton's method, 2012. URL `https://www.math.uni-bielefeld.de/documenta/vol-ismp/13_deuflhard-peter.pdf`.

[11] P. Deuflhard. *Newton Methods for Nonlinear Problems. Affine Invariance and Adap-*

tive Algorithms. Vol. 35 of *Computational Mathematics.*, Springer International, 2004. URL `https://doi.org/10.1007/978-3-642-23899-4`.

[12] F. Ferrari, M. Lavagna, M. Scheper, B. Burmann, and I. Carnelli. "The European asteroid impact mission: phase A design and mission analysis". *American Astronautical So- ciety/American Institute of Aeronautics and Astronautics, Astrodynamics Specialist Conference.* Vail (CO), USA, Aug. 2015. URL `https://www.researchgate.net/publication/281967574`.

[13] C. F. Gauss. *Theoria motus corporum coelestium in sectionibus conicis solem ambientum.* Hamburg: Friedrich Perthes and I.H. Besser, 1809.

[14] L. George and L. D. Kos. Interplanetary mission design handbook: Earth-to-mars mission opportunities and mars-to-earth return opportunities, 2009 - 2024. Technical report, JPL, 1998, doi: 10.13140/RG.2.2.14994.56008.

[15] R. H. Gooding. "A procedure for the solution of Lambert's orbital boundary-value problem". *Celestial Mechanics and Dynamical Astronomy.* Vol. 48, pp. 145–165, 1990, doi: 10.1007/BF00049511.

[16] D. Izzo. "Revisiting Lambert's problem". *Celestial Mechanics and Dynamical Astronomy.* Vol. 121, pp. 1-15, 2015, doi: 10.1007/s10569-014-9587-y.

[17] D. Izzo, V. M. Becerra, D. R. Myatt, S. J. Nasuto, and J. M. Bishop. "Search space pruning and global optimisation of multiple gravity assist spacecraft trajectories". *Journal of Global Optimization.* Vol. 2, No. 38, pp. 283-296, 2007, doi: 10.1007/s10898-006-9106-0.

[18] J. Jordan. The application of lambert's theorem to the solution of interplanetary transfer problems. Technical report, JPL, 1964.

[19] E. R. Lancaster and R. C. Blanchard. A unified form of lambert's theorem, 1969. URL `https://ntrs.nasa.gov/search.jsp?R=19690027552`.

[20] E. R. Lancaster, R. C. Blanchard, and R. A. Devaney. A note on lambert's theorem, 1966. URL `https://ntrs.nasa.gov/api/citations/19660010192/downloads/19660010192.pdf`.

[21] S. Matousek and A. Sergeyevsky. "To Mars and back - 2002-2020: Ballistic trajectory data for the Mission Architect". *AIAA/AAS Astrodynamics Specialist Conference and Exhibit.* Boston (MA), 10-12 August, 1998, doi: 10.2514/6.1998-4396.

[22] D. Menzio. "Grid search application for trajectory design in presence of fly-

bys". PhD dissertation, Politecnico di Milano, 2019. Supervisor: Camilla Colombo
. URL `https://www.politesi.polimi.it/bitstream/10589/152568/5/Menzio_`
`FinalPhDDissertation.pdf`.

[23] D. Menzio and C. Colombo. "An analysis of the pork-chop plot for direct and multi-revolution flyby missions". In *Advance in the Astronautical Sciences*, pp. 1739-1753, 2018. Paper presented at the *4th IAA Conference on Dynamics and Control of Space Systems* in Changsha (CN), 21-23 May, 2018. URL `http://hdl.handle.net/11311/`
`1056553`.

[24] D. Menzio and C. Colombo. "The combined Lambert-Tisserand method applied to the single flyby problem". Paper presented at the *68th International Astronautical Congress (IAC 2017)*, Adelaide (AU), 25-29 Sept. 2017, pp. 1-12. URL `http://hdl.`
`handle.net/11311/1034741`.

[25] P. J. Mohr, D. B. Newell, and B. N. Taylor. "CODATA recommended values of the fundamental physical constants: 2014". *Reviews of Modern Physics*. Vol. 88, No. 3, 26 Sept. 2016. doi: 10.1103/RevModPhys.88.035009. URL `https://link.aps.org/`
`doi/10.1103/RevModPhys.88.035009`.

[26] NASA/JPL. Planetary satellite mean elements. URL `https://ssd.jpl.nasa.gov/`
`sats/elem/`.

[27] J. E. Prussing and B. A. Conway. *Orbital Mechanics*. Oxford Univ Pr, 2012.

[28] J. Schoenmaekers, R. Jehn, M. Landgraf, and M. Khan. "Mission analysis - Towards a European harmonisation". *ESA bulletin. Bulletin ASE. European Space Agency*. Vol. 134, pp. 10-19, May 2008.

[29] W. Seefelder. *Lunar Transfer Orbits Utilizing Solar Perturbations and Ballistic Capture*. pp. 76, Herbert Utz Verlag, 2002. ISBN 9783831601554.

[30] J. J. Sellers, W. J. Astore, R. B. Giffen, and W. J. Larson. *Understanding Space: An Introduction to Astronautics, 2nd Edition*, McGraw Hill, pp. 228, 2004.

[31] A. B. Sergeyevsky, G. C. Snyder, and R. A. Cunniff. Interplanetary mission design handbook. volume 1, part 2: Earth to mars ballistic mission opportunities, 1990-2005. Technical report, JPL, 1983. URL `https://ntrs.nasa.gov/api/citations/`
`19840010158/downloads/19840010158.pdf`.

[32] H. Shen and P. Tsiotras. "Using Battin's method to obtain multiple-revolution Lambert's solutions", *Advances in the Astronautical Sciences*. Vol. 116, pp. 1067-1084, 2003.

[33] J. S. Townley, J. L. Sharma, and J. M. Lafleur. "Cost based launch opportunity selection applied to rendezvous with 99942 Apophis". *American Astronautical Society/American Institute of Aeronautics and Astronautics Space Flight Mechanics Meeting*. Galveston (TE), Jan. 27-31, 2008.

[34] O. Volk. "Johann Heinrich Lambert and the determination of orbits for planets and comets". *Celestial Mechanics*. Vol. 21, No. 2, pp. 237-250, 1980.

[35] P. J. Westwick. *Into the Black: JPL and the American Space Program, 1976-2004*. Yale University Press, 2011.

[36] R. C. Woolley and C. W. Whetsel. On the nature of earth-mars porkchop plots. Technical report, NASA/JPL, 2013. URL `http://hdl.handle.net/2014/44336`.

[37] R. Yuan, C. Pingyuan, and L. Enjie. "Exploration Opportunity Search for Near Earth Small Body". *25th Chinese Control Conference*. Harbin, Heilongjiang, China, 7-11 Aug. 2006, IEEE, doi: 10.1109/CHICC.2006.280690.

A | Appendix A

The effect of Earth eccentricity in the modification of the ΔV contours is similar to the effect of the Mars eccentricity. A difference concerns the trend of the minimum solution for varying eccentricities. Differently from Case 1, the best scenario is not the one belonging to CLASS II. The minimum $\Delta V0$ solution is found at very low eccentricity of Earth.
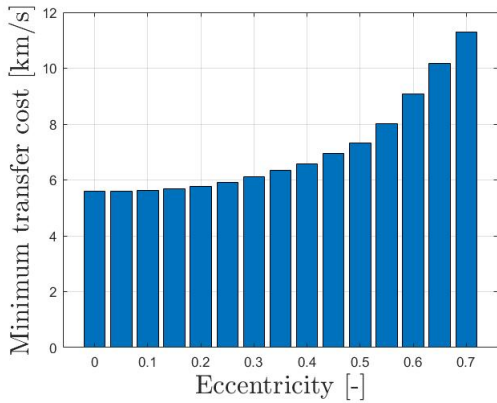
Figure A.1: Magnitude of minimum ΔV for varying eccentricities (Case 2)
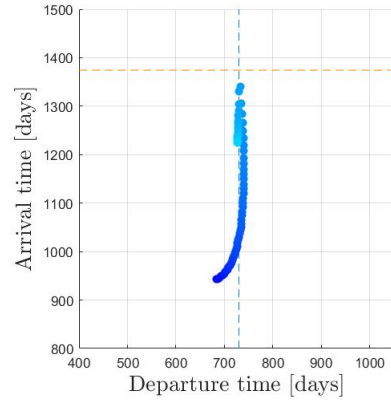
Figure A.2: Evolution of minima location on porkchop plot for varying eccentricity (Case 2)

This is due to the fact that, at this stage, the phasing was not considered and the initial θ was imposed as zero for both planets. Given this hypothesis, the two planets cannot arrive at the intersection point in the same moment, thus making impossible the one impulse transfer and giving no advantages for the eccentricity of CLASS II. Clearly, the reasoning would be different in case the initial θ is imposed as 180 deg for both planets.

The location of minimum for varying eccentricity was produced for Case 2 analogously to Case 1. In Figure A.2 the alignment of the minima with the transit line behaves as expected. In this case the characteristic transit date is the transit at the aphelium. This is can be observed by making reference to CLASS II. Indeed, for the eccentricity whose orbit produce two tangent orbits, the intersection point occurs at the aphelium. In this case the initial position is imposed to be the one allowing a rendez-vous of the two planets at $\theta = 180$ deg.

The effect of phasing can be highly reproduced. In order to produce an analogous situation, the offsets are introduced with respect to $\theta = 180\ deg$ instead of $\theta = 0\ deg$.

The analysis of the minima in Figure A.1 suggests that in Case 2 the ΔV levels are slightly higher than in Case 1, implying a worse situation regarding the transfer cost. As a result, the plots with phasing were produced showing the contours at $\Delta V = 8\ km/s$. The noticed trend were observed to be similar to Case 1 both for introduced phasing of Earth and Mars. Even in this case the contours tend to align to specific transit lines, however this time the relevant lines consider the transit at aphelium.

The results are displayed in the following two figures making reference again to the curves y_{mean} which is an optimum approximation of the envelop evolution :
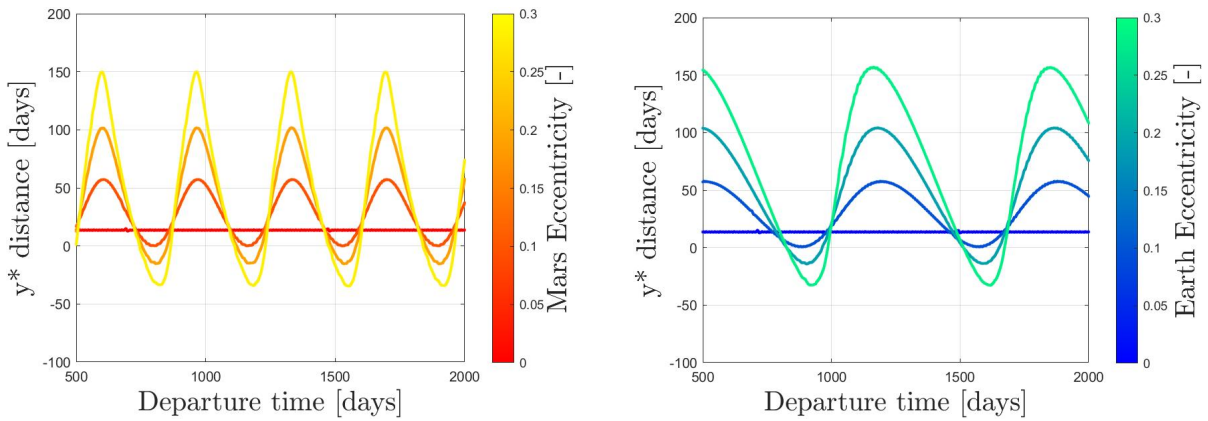
Figure A.3: Evolution of y_{mean} envelop due to introduced offset of Mars (left) and Earth (right) for Case 2.

Acknowledgements

Un grazie speciale va alla mia nonna Amalia. Quando passavo un esame, non riuscivi ad accettare che il voto fosse registrato online, perché avresti voluto leggerlo su un libretto cartaceo. Oggi, dovunque tu sia, spero che questa dedica possa raggiungerti. Stavolta il risultato è concreto, reale, tangibile. Spero che ne saresti stata orgogliosa almeno metà di quanto io sia orgoglioso del fatto che tu sia stata la mia nonna.